Title	Interfacial Ionic Conduction Mechanisms in Alkali-ion Conductive Electrolytes
Author(s)	齋藤, 唯理亜
Citation	大阪大学, 1992, 博士論文
Version Type	VoR
URL	https://doi.org/10.11501/3091083
rights	
Note	

INTERFACIAL IONIC CONDUCTION MECHANISMS

IN ALKALI-ION CONDUCTIVE

COMPOSITE ELECTROLYTES

YURIA   SAITO

December   1992

Interfacial Ionic Conduction Mechanisms in Alkali-ion Conductive Composite Electrolytes

Government Industrial Research Institute, Osaka

Yuria Saito

Contents

1. Introduction

An idea of material design in which we can create something on an artificial material is required for the development of functional materials. Studies of materials have generally been concentrated on single crystal originated features. However, interfaces in materials exhibit a wide variety of defects such as interstitial ions, vacancies, dislocations and its consequent electronic structures. These defects sometimes show the anomalous features which are not deduced from the single crystal oriented studies.

When a material was used as the form of sintered ceramics, the effects of grain boundaries and interfaces on the ceramics property have been neglected because they interfere with the bulk properties and are difficult to control. However, it is now accepted that the grain boundary and interface may have significant effects on properties of some electronic devices such as superconductors[1] and varistors[2]. This suggests that the grain boundaries and interfaces are possible regions which exhibit anomalous features inconceivable from the bulk region. The control of the interfacial properties enough to evaluate quantitatively would be necessary to taylor the interfacial function in material designing.

Ceramic solid electrolyte, which is an ionic conductor and an electronic insulator, is a typical example for the observation of interfacial anomalous feature. When some insulator particles were dispersed into ionic conductor particles to make a composite, the electrical conductivity was enhanced in some cases.

These phenomena have widely been reported since the first systematic study by Liang in which LiI dispersed by Al_2O_3 particles showed the ten times enhanced conductivity compared with that of pure LiI[3]. Since then, over 20 different crystalline materials of metal halides have been found to increase the conductivity with the addition of particles of an insoluble second phase. The most extensively studied composites were composed of silver, lithium or copper halide (e.g., LiBr[4], AgI[5], CuCl[6], HgI_2[7] and TlCl[8]) and the dispersed particles of insulator, such as alumina and silica. Typically composites containing 10 to 40 volume percent (vol%) of submicron particles showed the maximum enhanced conductivity by one to three orders of magnitude. The smaller the dispersed particle size was, the greater the enhancement was[9]. In the case of Al_2O_3 particle dispersion, dispersoid particles containing bound surface water were found to be more effective than predried particles[10]. The enhancement with respect to the pure phase was associated with the extrinsic conductivity occurred at lower temperature.

The mechanism responsible for this enhancement in the ionic conductor have been reported. These mechanisms would be classified into two categories, that is, the interfacial mechanisms and matrix mechanisms[11]. The interfacial mechanisms propose the enhanced conduction layer along the interface between ionic conductor and insulator particles. In matrix phenomena, the insulator modifies the conductivity in the matrix phase chemically and/or mechanically. Details of each mechanism will be explained in chapter 3-1. In these discussions, formation of a space charge layer at the interface, which is based on the inter-

facial mechanisms, is the most widely studied and accepted me-
chansim because the model could introduce the additional defects,
which were the origin of increased mobile ions, based on the
Schottky barrier model in semiconductor. Furthermore, the calcu-
lated results according to the space charge layer model were
consistent with the experimental results in which the conductivi-
ty was enhanced with the increase of dispersoid content in the
low dispersoid content, and smaller particle dispersion showed
higher enhancement[9]. However, the conductivity enhancement
process at the space charge layer is not systematically con-
structed yet. Furthermore, it is suggested that the width of
space charge layer, which is evaluated about few hundreds of
angstrom, is not enough to explain the conductivity enhancement
more than one order of magnitude because it comprises only a few
volume percent of a total particle.

These theoretical researches which have been reported were
only concentrated on the explanation of the observed results in
typical composites described above. They do not offer the pre-
diction of the conductivity enhancement in the different kinds of
composites.

In order to establish the enhanced conduction mechanism due
to the spacial ion conductive layer at the interface, contribut-
ing factors to the formation of the layer should be demonstrated.
The author proposes two models experimentally to suggest the
essential factors for the interfacial high conductivity between
ionic conductor and insulator particles. Firstly, it is probable
that acid-base interaction between ionic conductors and insulator
particles is significant in the enhancement from the analogy with

the Al_2O_3 particle dispersion where acidic -OH or H_2O species adsorbed on the surface of the particles were expected to be the principal factors for the formation of interfacial layer[5]. The effect of acidic species is supported from the fact that Al_2O_3 particles containing bound water were found to be more effective on the enhancement rather than the dried particles[10]. Furthermore, dispersion of Al_2O_3 particles whose surface were modified with MeLi or MeSiCl (Me: Methyl) into AgBr to know the influence of surface active centers has also shown the conductivity enhancement compared with pure AgBr[10]. In order to make sure of this idea, the particles possessing strong acidic sites will be applied as a dispersoid.

Secondly, dielectric interaciton at the interface would be important for the enhancement at the interface because it is defined in the theoretical researches that the width of space charge layer depends on the dielectric constant. When two different materials contact, each chemical potential changes to coinside at the interface, which is well known in the field of electronics of semiconductors[2]. Consequently, induced potential change at the interface would form the space charge layer in which the layers of vacancies and interstitial ions aligned alternately. It is suggested in the space charge layer model that those defects are responsible for the enhanced conductivity. In order to investigate the dielectric effect on the enhancement, the author plans to use the ferroelectric materials with high dielectric constants as dispersoids.

The enhanced conductivity depends on the increase of carrier concentration and/or mobility. Therefore, it may be offered that

the concentrated defects, such as interstitial ions and vacancies, at the interface cause the increase of carrier concentration and/or mobiltiy. Mobile ion would hop along the layer in which defects are aligned to be utilized for ion migration.

This enhancement model at the interface between heterogeneous particles would be supported if the defects are introduced in a conductor intentionally and the consequent enhancement of the conductivity is evaluated correlated with the properties of the defects. In order to create this situation, the author will take the means of substitution with aliovalent ion in the crystal structure. When one host ion are substituted by another ion with different valence, some defects such as interstitial ions and vacancies would be introduced in the structure. Conductivity enhancement due to the additionally introduced defects depends on the content and property of the dopants. Comprehensive studies of dopant effects on the mobile ion content and/or mobility will be conducted in $LiTi_2(PO_4)_3$, Li_4SiO_4 and $NaZr_2(PO_4)_3$ conductors.

Substitution of an ion with an aliovalent ion not only introduces the defects for charge compensation but displaces and polarizes the neighbouring ions. The total effect of these changes contribute to the conductivity enhancement which reflects the increase of mobile ion content and/or the mobility. Therefore, it would be natural to accept the concept of the 'defect core structure' composed of the doped ion, defects, and displaced and polarized ions, as a source of conductivity enhancement. If the conductivity enhancement by the insulator particle dispersion could be explained using the defect core structure, the enhancement mechanism would be realized with the concept of mobile ion

content and its mobility generalized in substituted ionic conductor.

The final goal of this research is to demonstrate the factors contributing to the enhanced conductivity by the insulator dispersion. Furthermore, it is expected that the effective concept to design the composite electrolytes with high conductivity and stability for practical use will be proposed finally.

References

[1]   J. Nowotny, M. Rekas, D. D. Sarma and W. Weppner in "Surface and near-surface chemistry of oxide materials" J. Nowotny and L-C. Dufour, eds., Ch. 16 (Elsevier, 1988).

[2]   D. Hennings in "Surface and near surface chemistry of oxide materials" J. Nowotny and L-C. Dufour eds., Ch. 11 (Elsevier, 1988).

[3]   C. Liang, J. Electrochem. Soc., 120, 1289 (1973).

[4]   C. D. Slade and I. M. Tompson, Solid adtate Ionics, 26, 287 (1988).

[5]   P. Chowdhary, V. B. Tare and J. B. Wagner, Jr., J. Electrochem. Soc., 132, 123 (1985).

[6]   T. Jow and J. B. Wagner, Jr., J. Electrochem. Soc., 126, 1963 (1979).

[7]   J. B. Wagner, Jr., Mat. Res. Bull., 15, 1691 (1980).

[8]   J. Maier and B. Reichert, Ber. Bunsenges. Phys. Chem., 90, 666 (1986).

[9]   O. Nakamura and J. B. Goodenough, Solid State Ionics, 7, 119 (1982).

[10]   J. Maier, Mat. Res. Bull., 20, 282 (1985).

[11]   N. J. Dudney, Solid State Ionics, 28-30, 1065 (1988).

2. Complex impedance analysis

Electrical measurements of ionic conductors for the electrical characterization determine the parameters which are most relevant to the application of the electrolytes in, for example, advanced batteries and sensors. The measurement techniques would be divided into two major groups, direct current (d.c.) measurements and alternating current (a.c.) measurements.

The d.c. technique of measuring a direct current between two metallic electrodes on the application of a stable d.c. voltage, is the more straightforward method although it yields less information than the a.c. technique. On the application of a stable d.c. voltage, V, a constant current, I, flows through the cell depending on the resistance of the electrolyte, R, which is calculated from R=V/I.

In an a.c. experiment, an alternating voltage is applied to a cell and the alternating current passing through the cell as a result of this perturbation is determined. The data gives information not only about the long-range migration of ions but also about polarization phenomena occurring within the cell, e.g., the relaxation of trapped ions related to the frequency of the applied voltage.

The data of a.c. conductivity have been analized in popular with the representation of complex planes. Furthermore, frequency dispersion analyses of a.c. conductivity have been applied to the ionic conductors to obtain the detailed information of ionic conduction. A combination of conventional complex plane analysis and frequency dispersion analysis of a.c. conductivity has

been developed to derive potential mobile ion concentration and its hopping rate corresponding to the ionic mobility. This procedure would be effective in the point that the two types of enhanced conduction phenomena, that is, the enhancements in composite conductors and in doped (non-stoichiometric) ionic conductors, could be discussed comparatively using the parameters of mobile ion content and hopping rate.

2.1 Complex impedance measurement and an equivalent circuit for ceramic material

Ionic conductors of ceramics are composed of bulk and grain boundary regions (fig. 2-1). Both regions are usually represented by a parallel combination of resistance and capacitance as a electric response[1]. Figure 2-2 represents the situation of an ionic conductor material with the electric responses of the each component, grain (bulk), grain boundary and electrode. Each combination of R-C circuit may be different, however, these were simplified to three characteristic components as shown in fig. 2-3. In general, the electrode is assumed to have infinite resistance, so that works only as polarized capacitance.

Figure 2-4 shows two typical a.c. data in the form of complex impedance plane plots of $LiTi_2(PO_4)_3$ ceramics. The data separates into a high frequency region composed of a semicircle and a low frequency region containing a spike that is sometimes linear and sometimes curved depending on the condition of electrodes. These results show that parallel combination of resistance and capacitance is a reasonable circuit to represent the
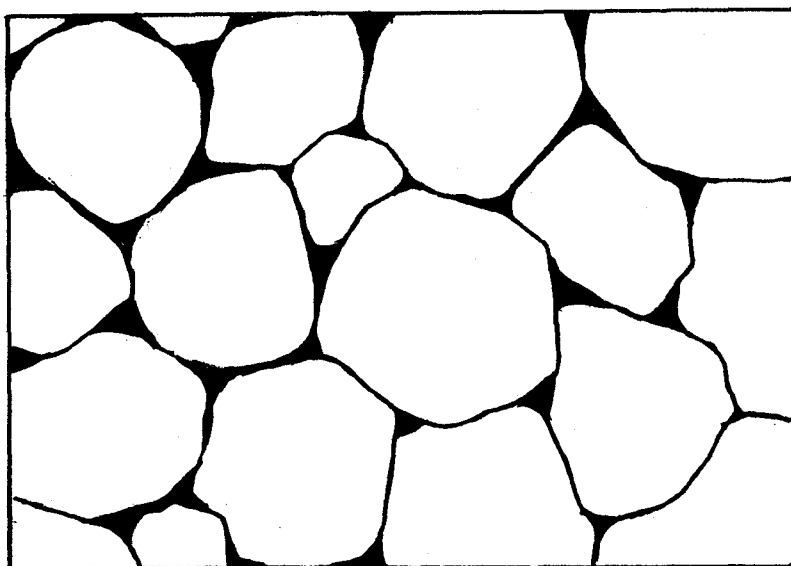
Fig. 2-1 Model of ceramic structure. ☐ : bulk, ■■ : grain boundary.

electrode
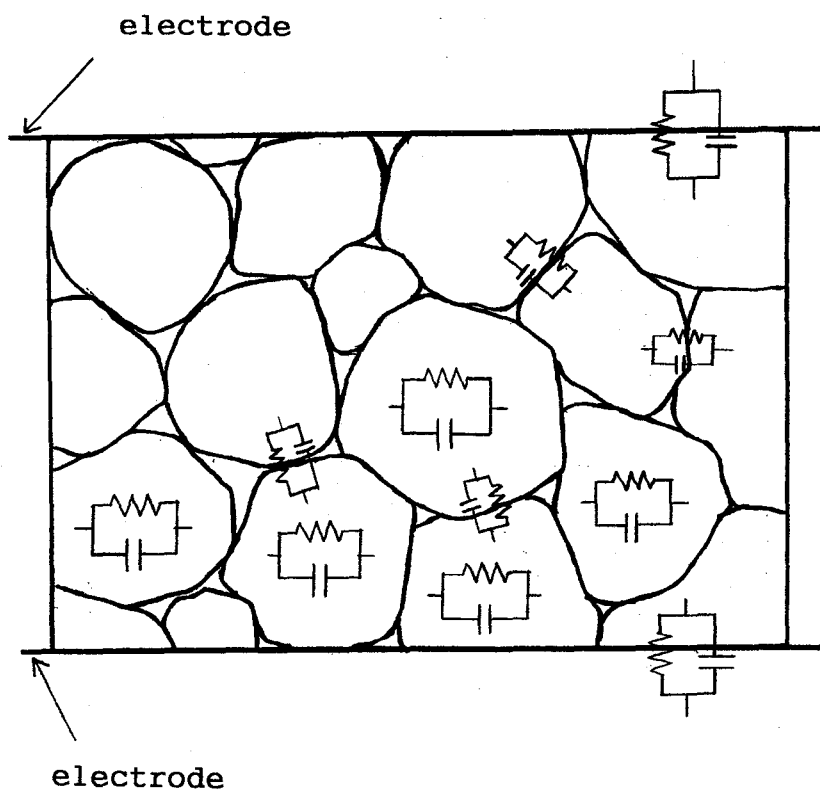
electrode

Fig. 2-2 Model of electric property of ceramics.

electrode | bulk | grain boundary | electrode

(a)

electrode | bulk | grain boundary
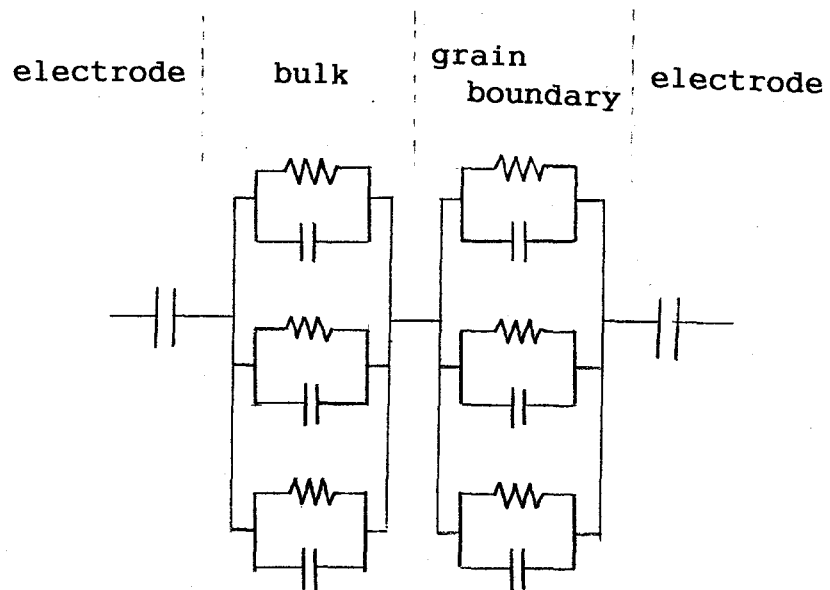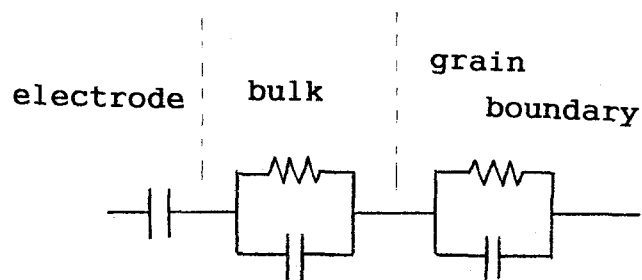
(b)

Fig. 2-3   Possible representation (a) and its simplified feature (b) of equivalent circuit of ceramic ionic conductors.

Fig. 2-4 Complex impedance plots for $LiTi_2(PO_4)_3$ with Au elec-
trodes at 100^oC. (a) sintered at 800^oC for 10 hours, (b) sin-
tered at 800^oC for 48 hours.

electric property in ceramic ionic conductor because a simple combination of parallel RC circuit indicates the complex impedance response of
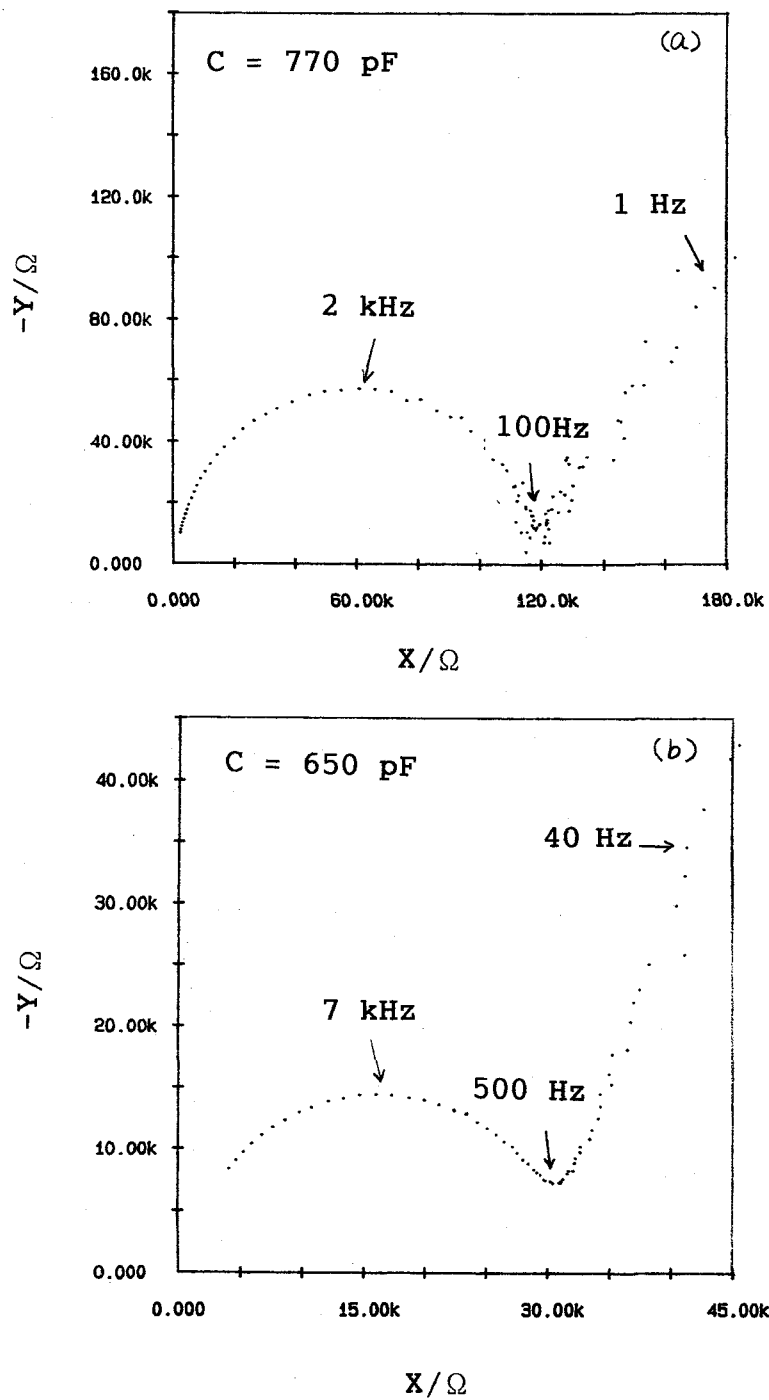
$$Z^* = (\frac{1}{Z_R} + \frac{1}{Z_C})^{-1}$$

$$= (1/R + j\omega C)^{-1}$$

$$= \frac{R}{1 + (\omega RC)^2} - \frac{j\omega R^2 C}{1 + (\omega RC)^2} \qquad (2\text{-}1)$$

which is represented by a semicircle in a complex plane. Combining the capacitance to this circuit explains the observed spike connecting with the circle. The magnitude of the semicircle depends on the firing temperature and sintering temperature for pelletization of ceramics. Using the relation $\omega RC=1$, which holds at the maximum of a semicircle, the capacitace of the ceramics was evaluated as 150 ~ 250 pFcm^{-1} in fig. 2-4. This magnitude represents charge polarization at the grain boundary[2].

High density ceramic pellets of ionic conductors sometimes show ac response with two semicircles[2]. The high frequency semicircle, which passes through the origin, is associated with intragranular or bulk responses of the conductor. The capacitance of the bulk is typically a few pFcm^{-1}[2]. This corresponds with what was expected regarding the dielectric polarization of the crystal represented by the relationship:

$$C_b = \varepsilon' C_0 \qquad (2-2)$$

where C_0 is the vaccum capacitance of the cell, and a typical ε' value of dielectric materials is 5~20. The low frequency semicircle is attributed to a grain boundary impedance in series with the bulk impedance. The typical value of its capacitance, C_{gb}, is in the range of 10~400 $pFcm^{-1}$[2]. The impedance plot in fig. 2-4 shows that the bulk resistance is so small that it is concealed by the semicircle of grain boundary components.

There are four basic formalisms that may be used to represent and analyze a.c. data. These are as follows:

$$\text{Complex admittance : } A^* = (Z^*)^{-1} = A' + jA'' \qquad (2-3)$$

$$\text{Complex permittivity : } \varepsilon^* = A^*/(j\omega C_0) = \varepsilon' - j\varepsilon'' \qquad (2-4)$$

$$\text{Complex electric modulus : } M^* = (\varepsilon^*)^{-1} = j\omega C_0 Z^* = M' + jM'' \qquad (2-5)$$

Different formalisms emphasize different features of a circuit. The complex impedance formalism gives prominence to the most resistive elements in an equivalent circuit. Thus in ceramics with relatively large grain boundary resistances and small bulk resistances, grain boundary resistances dominate the a.c. response in a complex impedance plane concealing the bulk effect behind them.

In the complex electric modulus formalism, however, the element that has the smallest capacitance is predominant. Therefore, the component of the grain boundary may effectively disap-

pear.   It is therefore possible to separate the effects of bulk

and grain boundary effectively by a comparison of the results

analyzed with these two different formalisms when the capaci-

tances of two components are orderly different.

As a typical model, the author could assume the equivalent

circuit represented in fig. 2-5(a). The complex impedance of the

circuit would be represented as fig. 2-5 (b), in which intracrys-

talline (bulk) semicircle appears in the higher frequency region

and usually difficult to extract the intracrystalline parameters.

When the impedance is replaced by modulus which is defined in equa-

tion (2-5), the size of each semicircle is proportional to C_0/C

appeared in fig. 2-5 (c).   Therefore, combination of the two

pictures, impedance and modulus plots, is available for the

estimation of the parameters of the material composed of some

fractions with different features.

$10^6 \; \Omega$ $10^8 \; \Omega$

$10^{-6} \; F$

$10^{-12} \; F$ $10^{-10} \; F$

bulk   grain   electrode
       boundary

(a)

Z"

$\omega R_{gb} C_{gb} = 1$

R_b $R_b + R_{gb}$ Z'

(b)

M"

$\omega R_b C_b = 1$

C_0 / C_{gb} M'
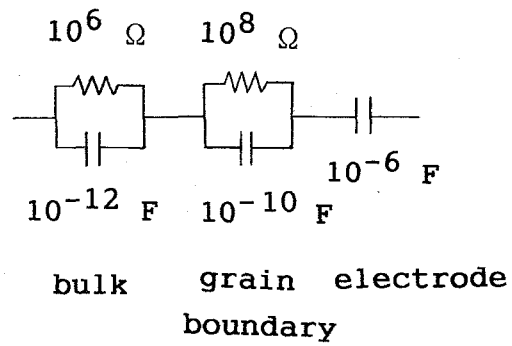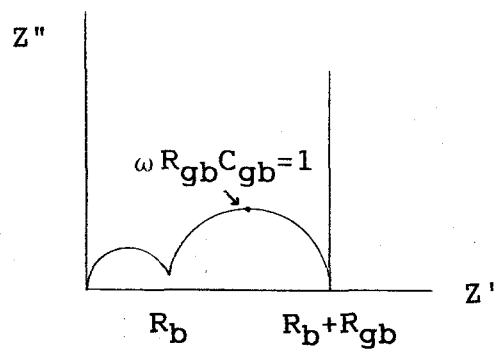
$C_0 (1/C_{gb} + 1/C_b)$
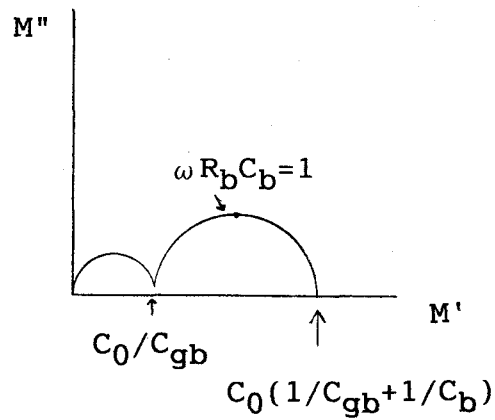
(c)

Fig. 2-5   Electrical response of typical ionic conductor.   (a) equivalent circuit, (b) complex impedance plot, (c) complex modulus plot.

2.2 Hopping rates and mobile ion concentrations by an analysis of a.c. conductivity

Ionic conductivity derived from the impedance measurements gives information of the movement of total ionic response to the certain frequency. The conductivity is generally represented by

$$\sigma = en\mu \tag{2-6}$$

where e is the electronic charge, n is the number of the charge carrier and μ is the mobility[1]. The author adopts the frequency dispersion analyses of a.c. conductivity proposed by Almond and West[3,4] for the detailed analysis of conductivity σ. The advantage of this method is that both n and hopping rate (ω_p) which is a main factor of μ would be estimated at the same time. This analysis would also be appropriate to know which is the major contribution to the conductivity change when the ionic conductors are modified by the dispersion of some particles or by substitution with some ions. Practical applications will be appear in chapters 3 and 4.

The systematic analysis of Almond and West is based on the model proposed by Jonscher, called 'Law of Universal Dielectric Response'[5]. Inherent notion of his approach is that individual polarization events do not take place independently each other but, rather, interact cooperatively. This means that if a dipole in a crystal reorients itself, this must influence neighbouring dipoles in the crystal. This is accepted as the extended concept of Debye type dielectric response which generally explains the

one-particle process[6].

Since all materials are composed of positive and negative charges, the application of an external electric field gives rise to a slight relative displacement of the centers of gravity in the positive and negative charge distributions. This is the cause of polarization, which indicates the reorientation of dipoles in dielectrics or the hopping of ions in conductors. In general, dielectric response is expected to obey the Debye response in which the decay of polarization from an initial value after sudden removal of the exciting field follows the simple first-order rate equation with a time constant τ;

$$\frac{dP}{dt} = - \frac{P}{\tau} \tag{2-7}$$

Equation (2-7) has a solution for polarization P represented by

$$P(t) = P_0 \exp(-t/\tau) \tag{2-8}$$

The Fourier transformation of this function gives the frequency dominant complex susceptibility,

$$\chi(\omega) = \frac{\chi(0)}{1+j\omega\tau} = \chi(0) \left(\frac{1}{1+\omega^2\tau^2} - j\frac{\omega\tau}{1+\omega^2\tau^2}\right) \tag{2-9}$$

The complex susceptibility diagram (Cole-Cole expression) of an ideal Debye system represents the semicircle, which is shown in fig. 2-6 with the frequency dependence of the real and imaginary
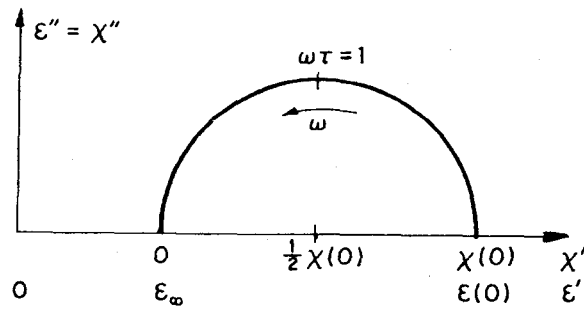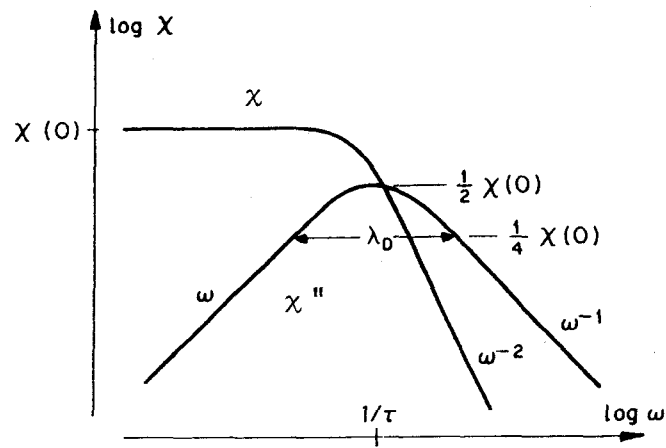
Fig. 2-6   The complex susceptibility diagram of ideal Debye system.   (a) Cole-Cole plots, (b) frequency dependence of the real and imaginary parts.

components of them.

In practice, the Cole-Cole plots are often not exactly semi-circular but are distorted to varying degrees. Similarly, the peaks in the dielectric loss, ε", are not symmetric Debye peaks but are often broadened asymmetrically. Conventional approach to describing such distorted peaks is to regard them as the superposition of an appropriate number of peaks, each, occuring at different frequency.

Contrary to these explanation, Jonscher proposed the universal power law relation generalized by

$$\chi"(\omega) \propto \omega^{n-1} \tag{2-10}$$

The magnitude of n depends on the strength of the cooperative interaction of dielectric response between the species.

When charge carriers are present in the dielectrics, e.g., ionic conductors, eq. (2-10) would be extended to

$$\chi"(\omega) \propto \frac{\sigma(\omega)}{\varepsilon_0 \omega}$$

$$\propto (\omega/\omega_p)^{n_1-1} + (\omega/\omega_p)^{n_2-1}. \tag{2-11}$$

Additional second term means the polarization event of the hopping of carriers in the material. Of course, since the effect of hopping of carriers and reorientation of dipoles or other polarization events could not be divided distinctly, n_1 and n_2 would contain the influence of several factors of responses.

Observed frequency dependence of ionic conductivity of $LiTi_2(PO_4)_3$ is shown in fig. 2-7. Dispersion of each plot in lower frequency region could be excepted because they are due to the polarization effects between the conductor and electrode. In intermediate frequency region, conductivity is independent of frequency, and further increase of frequency shows the gradual increase of conductivity. This figure is represented empirically by

$$\sigma(\omega) = \sigma(0) + A\omega^n \tag{2-12}$$

where A is a constant corresponding to each temperature, and exponent n is calculated to 0.7. n is observed typically in the range of $0<n<1$ in many ionic conductors. Equation (2-12) shows a typical case of the exponent of lower frequency, $n_2 \sim 0$ in equation (2-11).

Comparison of equation (2-11) and (2-12) represents

$$\sigma(0) = K\omega_p \tag{2-13}$$

$$A = K\omega_p^{1-n} \tag{2-14}$$

where K is the constant proportional to ε_0.

Hopping rate, ω_p, is associated with relaxation time, τ, and thermally activated as follows,

$$\omega_p = 1/\tau = \omega_0 \exp(-\Delta G_a/kT)$$
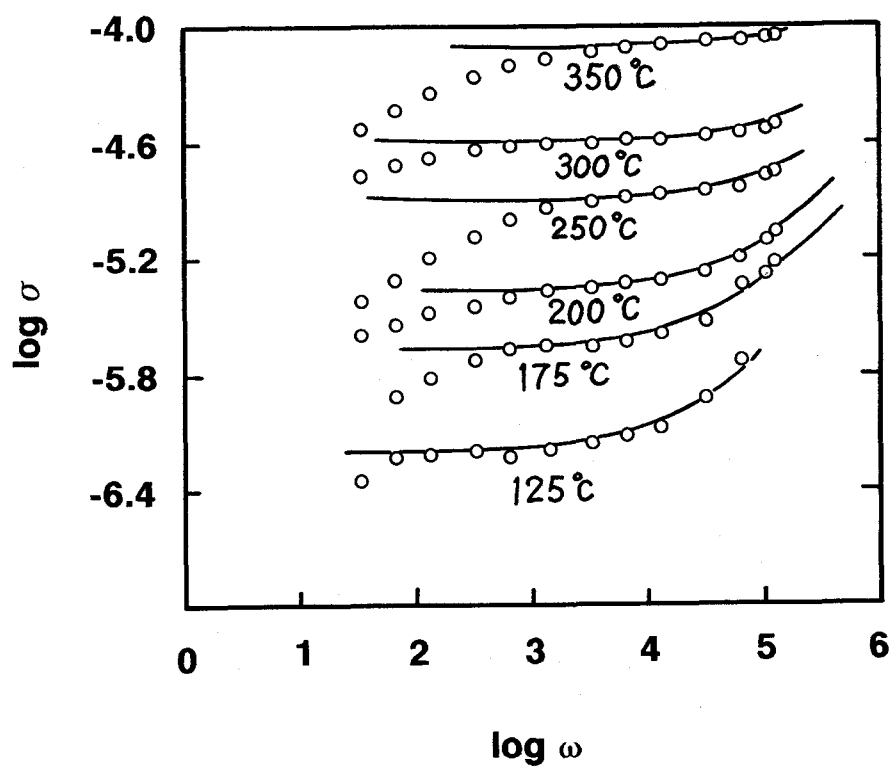$$= \omega_0 \exp(\Delta S_a/k) \exp(-E_a/kT)$$

Fig. 2-7 Frequency dependence of ionic conductivity of $LiTi_2(PO_4)_3$.

$$= \omega_e \exp(-E_a/kT) \qquad (2\text{-}15)$$

where ΔG_a, E_a and ΔS_a are the free energy, enthalpy and entropy for activation, respectively, for the migration of mobile carriers and ω_e is effective attempt frequency.

d.c. conductivity $\sigma(0)$ comes from the fundamental ionic hopping, and is related with the self diffusion factor, D, by the Nernst-Einstein equation[1] as

$$\sigma(0) = \frac{aN(Ze)^2}{kT} D \qquad (2\text{-}16)$$

where a is a correlation factor depending on the mechanism of ion migration, Ze is the charge on the mobile ions, N is the number of the equivalent lattice site per unit volume, k is the Boltzmann constant and T is the absolute temperature. D is represented by the atomic migration model in solid by the random walk,

$$D = (1/6)fr^2 \qquad (2\text{-}17)$$

where f is the frequency factor and r is the interatomic distance. f is proportional to the hopping rate, ω_p. And it is proportional to the carrier concentration, c, and the vacancy concentration, 1-c into which carriers may jump. Therefore,

$$f = \alpha \omega_p c(1\text{-}c) \qquad (2\text{-}18)$$

where α is the constant. Combining (2-16) to (2-18), $\sigma(0)$ is

summarized in

$$\sigma(0) = (kT)^{-1}aN(Ze)^2(1/6)\alpha\,\omega_p c(1-c)r^2$$

$$= (kT)^{-1}N(Ze)^2 r^2 \gamma c(1-c)\omega_p \qquad (2\text{-}19)$$

$$(\gamma = (1/6)\alpha a)$$

This shows that the d.c. conductivity depends on the hopping rate of ions ω_p and on the carrier concentration c if c<<1. Compared this representation with equation (2-13), we obtaion

$$K = (kT)^{-1}N(Ze)^2 r^2 \gamma c(1-c). \qquad (2\text{-}20)$$

Thus, we recognize that K is the c dependent constant. a.c. conductivity component of $\sigma(\omega)$ is derived from the relationship between (2-12) and (2-14) as

$$A\omega^n = (1/kT)N(Ze)^2 r^2 \gamma c(1-c)\omega_p^{1-n}\omega^n \qquad (2\text{-}21)$$

The $\sigma(0)$ and A in each temperature, and n which is assumed to be independent of temperature are determined by fitting of the experimental data to equation (2-12). c and ω_p are determined from the equations of both (2-19) and (2-21), with the substitution of appropriate values for some factors corresponding to the crystal structure. c corresponds to the n in equation (2-6) and ω_p mainly affect μ in equation (2-6). It must be noted that the mobility μ depends on N or γ which represent the structural

feature of each compound in equation (2-20). Temperature dependence of $\sigma(0)$ and A shows the characteristic conduction feature of the material. When the activaiton energies of $\sigma(0)$ and A are in the ratio 1:(1-n), ω_p is only the temperature dependent factor from the relationship between the equations (2-13) and (2-14). If the activation energies of $\sigma(0)$ and A are out of the ratio 1;(1-n), some cases should be considered to extract the practical conduction mechanism. One possibility is the temperature dependence of K of eq. (2-20). Almond and West have assumed that the carrier concentration c in K had the temperature dependence and represented as

$$c = c_0 \exp(-\Delta G_c / kT)$$

$$= c_0 \exp(\Delta S_c / k) \exp(-E_c / kT)$$

$$= c_e \exp(-E_c / kT) \tag{2-22}$$

where ΔG_c, E_c and ΔS_c are the free energy, enthalpy and entropy of activation, respectively, for the creation of mobile carriers, and c_e is the effective carrier concentration.

Another reason of the deviation of the E_a ratio from 1:(1-n) is that some different mechanisms of conduction would exist comparably. In this case, it must be needed to add another term to equation (2-11) characterized by different exponents.

The values of $\sigma(0)$ and A obtained from the least squares fit of experimental data to equation (2-12) are plotted in Arrhenius format in fig. 2-8. In the case of $LiTi_2(PO_4)_3$, the activa-
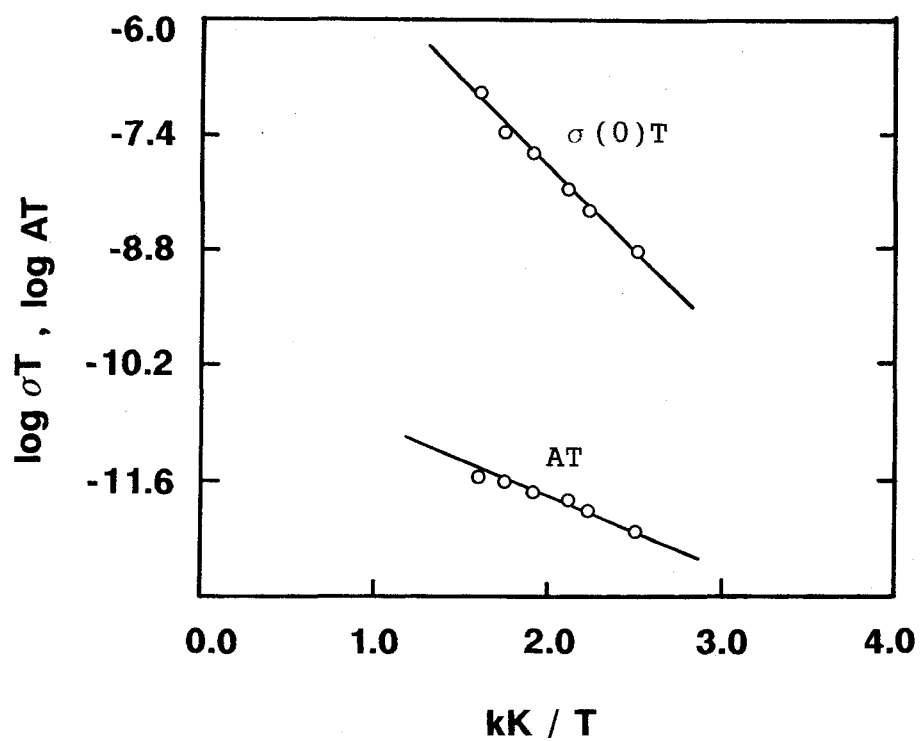
Fig. 2-8 Arrhenius plots $\sigma(0)$ and A derived from the fitting
results to equation (2-12).

tion energies of $\sigma(0)$ and A are in the ratio $1:(1-n)$, indicating the temperature independence of mobile ion concentration. By the comparison of equations (2-13) and (2-14), the hopping rate ω_p is given by

$$\omega_p = (\sigma(0)/A)^{1/n} \tag{2-23}$$

The hopping rate ω_p calculated from equation (2-23) is shown in Arrhenius format in fig. 2-9. The activaiton energy was within experimental error the same as that found for $\sigma(0)$ in fig. 2-8. The effective attempt frequency ω_e obtained from fig. 2-9 is close to the typical value for ω_0 ($10^{12} \sim 10^{13}$ Hz) which is obtained from infrared absorption or Raman scattering.

In order to evaluate c in equation (2-20), the jump distance, r, was assumed as 3Å, from the average value of the distance between Li^+ sites, and γ was assumed to 0.3 from the empirical data. N is the equivalent lattice sites per unit volume. In the case of Li_4SiO_4, it is therefore 18/unit cell. The carrier concentration c is then calculated to be the order of a few percents. The carrier concentrations of other ionic conductors are also reported to be the order of a few percents[2]. This is reasonable from the fact that they are the members of the rigid structure of solid.
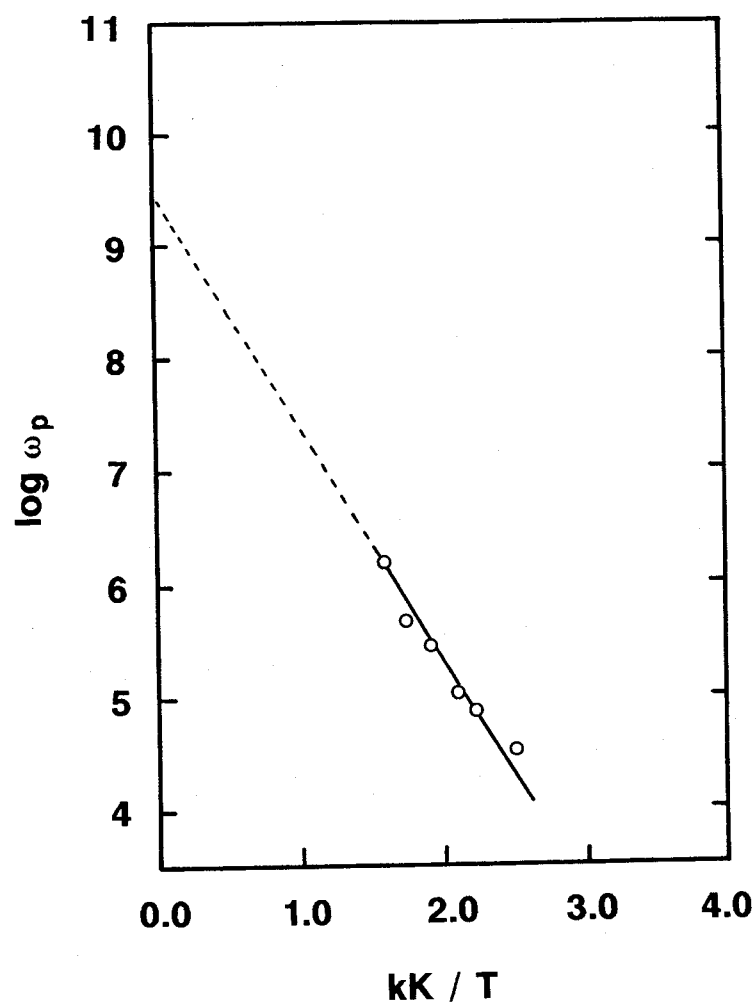
Fig. 2-9 Arrhenius plots of ω_p derived from equation (2-23).

References

[1]   A. R. West, Solid State Chemistry and its Applications, Wiley, New York, 1984.

[2]   P. G. Bruce and A. R. West, J. Electrochem. Soc., <u>130</u>, 662.

[3]   D. P. Almond. G. K. Duncan and A. R. West, Solid State Ionics, <u>8</u>, 159 (1983).

[4]   D. P. Almond and A. R. West, Solid State Ionics, <u>9,10</u>, 277 (1983).

[5]   A. K. Jonscher, Nature, 267, 673 (1977).

[6]   A. K. Jonscher, Phys. Thin Film, <u>11</u>, 236 (1980).

3. Interfacial layer conductivity between different particles

It has been widely reported that the conductivities of some ionic conductors were enhanced by the dispersion of insulator particles. The most extensively studied composites are composed of ionic conductors as silver, lithium or copper halides, and insulators such as alumina, silica and zirconia. Typically, composites containing 10 to 40 volume percent (vol%) of insulator particles show the maximum enhancement by about one or two orders of magnitude. Dispersion of smaller size particles showed the larger enhanced conductivity. The enhancement with respect to the pure phase is associated with the extrinsic conductivity mainly observed at lower temperature. Many of these composites would become promising solid electrolyte materials for battery, fuel cell and sensor since they are easy in fabrication and stable for practical use.

The mechanisms responsible for this enhancement in the ionic conductivity are still a matter of some debate. A composite containing an appropriate volume fraction of insulator particles would have the ionic conductor-insulator particle interface. It is now widely accepted that the overall effect of forming the composite is to create a highly conductive path along the interfaces. The relevant reactions occurring at the interface of an oxide particle dispersed in a halide are compared in Table 3-1 with the corresponding surface reactions in the particle hydrates. In metal halide - oxide composites, the conductivity enhancement is explained by the formation of vacancies or interstitial ions.

Table 3-1　Surface reaction in particle hydrate and interfacial reaction between halide (MX, M=Li or Ag and X=Br or I) and oxide particles

| Oxide particle (x=Br or I) [a)]	Host	Surface reaction	Net charge particle	Net charge sc [b)]	Mobile ion
Particle hydrates					
acidic	H_2O	$(H_2O)_s + H_2O \rightleftharpoons (OH^-)_s + H_3O^+$	−	+	H_i^+
		$(OH^-)_s + H_2O \rightarrow (O^{2-})_s + H_3O^+$			
basic	H_2O	$(OH^-) + H_2O \rightleftharpoons (H_2O)_s + OH^-$	+	−	V_H^-
		$(O^{2-})_s + H_2O \rightleftharpoons (OH^-)_s + OH^-$			
Halides with dispersed oxides					
W	MX	$(H_2O)_s + 2MX \rightarrow (OM_2)_s + 2HX\uparrow$	0	0	
		$(O^{2-})_s + MX \rightleftharpoons (OM^-)_s + V_M^-$	+	−	V_M^-
		$(OH^-)_s + MX \leftarrow (O^{2-})_s + HX\uparrow + M_i^+$	−	+	M_i^+
D	MX	$(O^{2-})_s + MX \rightleftharpoons (OM^-)_s + V_M^-$	+	−	V_M^-
		$(V_O)_s + MX \rightarrow (X^-)_s + M_i^+$	−	+	M_i^+

a) W=wet, D=dry.　b) sc=charge layer.

$(H_2O)_s$: H_2O molecule located at the particle surface

M_i^+: interstitial metal ion, V_M^-: metal ion vacancy

In the LiX-oxide composite, V_M^- contributes to the enhanced conductivity, and in the AgX-oxide composite, M_i^+ created by wet particle dispersion contributes to the enhanced conductivity.

The reaction at the interface between metal halide matrix and oxide particles would depend on the surface condition of the oxide particles[1]. The surface of a wet oxide particle, which is exposed to the air at room temperature before dispersion, contains bound water that completes the oxygen coordination of the surface cations and the associated protons are distributed over the surface. A dry particle has no bound water, that is, a surface cation with deficient anion coordination may induce a reversible restructuring of the surface that, on contact with the salt, returns to normal with the capture of an anion from the salt. These are shown schematically in fig. 3-1.

The proposed enhancement mechanism of the lithium salts, LiI and LiBr, must be distinguished from that of the silver salts AgI and AgBr. By the dispersion of wet oxide particles into the lithium halide matrix, Li^+ ions displace surface protons from the wet particles,

$$(H_2O)_s \;+\; 2\ LiX \;\rightarrow\; (OLi_2)_s \;+\; 2\ HX\uparrow \qquad (3\text{-}1)$$
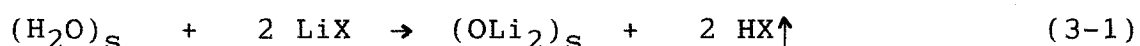
which does not introduce any defects as interstitial or vacancy of cations. However, the oxide ions on both the wet and the dry particles attract Li^+ ions from the salt via the reaction

$$(O^{2-})_s \;+\; LiX \;\rightleftharpoons\; (OLi)_s^- \;+\; V_{Li}^- \qquad (3\text{-}2)$$
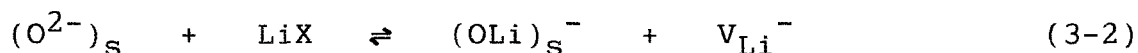
until the electrochemical potential for Li^+ in the oxide becomes equal to that in the salt via the space charge layer capacitance created by the Li^+ ion transfer. Therefore the enhanced conduc-
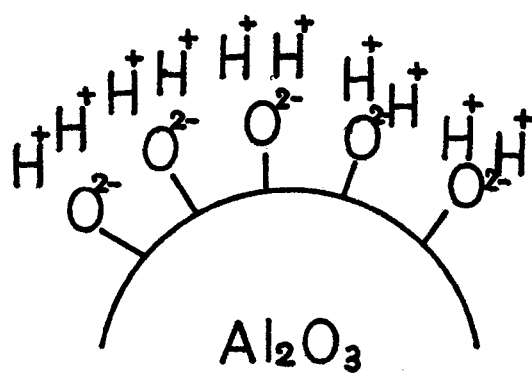
(a)
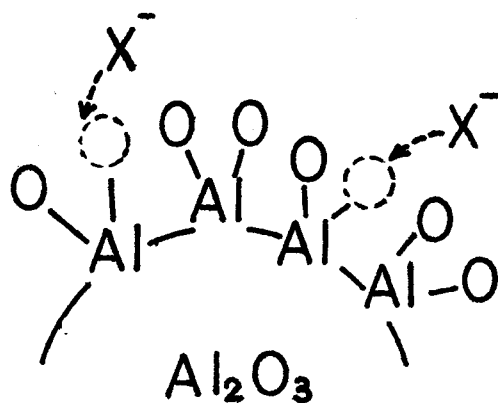
(b)

Fig. 3-1   Schematic features of the surface of Al_2O_3 in   (a) wet
and (b) dry atmosphere.

tivity of LiX halide by both the wet and dry particle dispersion of oxide is attributable to the Li^+ ion vacancies, V_{Li}^-, at the interface. The Li^+ ion conduction in the space charge layer induced by the reaction should be via V_{Li}^-.

The Ag^+ ion, on the other hand, does not displace a surface proton. In the silver salts with a wet particle, reaction (3-1) is replaced by

$$(OH^-)_s \quad + \quad AgX \quad \rightarrow \quad (O^{2-})_s \quad + \quad HX\uparrow \quad + \quad Ag_i^+ \qquad (3-3)$$
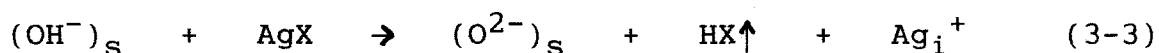
where Ag_i^+ is an interstitial Ag^+ ion. Reaction with oxide ions on both the wet and dry particles would induce the reaction

$$(O^{2-})_s \quad + \quad AgX \quad \rightleftharpoons \quad (OAg^-)_s \quad + \quad V_{Ag}^- \qquad (3-4)$$
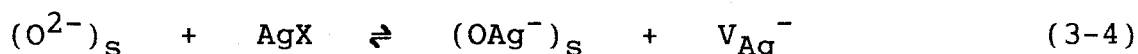
This is shifted strongly to the left. Therefore, conductivity enhancement of the silver halide would mainly depend on interstitial Ag^+ ions in equation (3-3). For a dry particle, the reaction

$$(V_O)_s \quad + \quad AgX \quad \rightleftharpoons \quad (X^-)_s \quad + \quad Ag_i^+ \qquad (3-5)$$
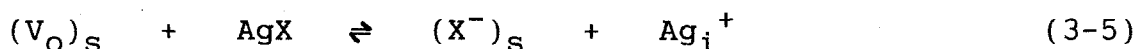
would be expected. For the AgBr , the enhancement of Ag^+ ion conductivity is observed only by the wet Al_2O_3 particle dispersion. This suggests that the equation (3-3) is the dominant reaction for AgBr conductor. It is predicted from this argument that the increased Ag^+ ions near the surface would form the space charge layer.

These models of defect formation are established only in simple metal-halide ionic conductors. And the application of them to other kinds of conductor such as oxide compounds is not achieved yet.

Contrary to the space charge model at the interface caused by the reaction with adsorbed H_2O species, the change of micro-structure in the ionic conductor particles would, in some cases, contribute to the conductivity enhancement. Ionic conductors of polycrystalline ceramics have extremely many micro-structural factors such as grain boundary, clack, vacancy and dislocation. Furthermore, when insulator particles are dispersed into the ionic conductor, some chemical reactions may occur at the interface to give an additional phase and alter the grain size, density, and crystal structure of the ionic conductor. It is difficult to control and estimate these possible contributions to the interfacial interaction for the enhancement because they depend on the preparation processes, correlate each other complicatedly and, in particular, there is no established technique for the estimation of the effects of micro-structures and/or interfacial reactions.

In this chapter, the author purposed to elucidate the factors which contribute to the enhanced conductivity of composites. Firstly, interfacial enhancement mechanisms which have been proposed in the simple system, metal halide/alumina or silica, will be summarized. They are compared with the following experimental researches of NZS composites to investigate the effective factors for the enhancement and to identify the interfacial situation when the enhanced conductivity is observed.

3.1 Concepts for interfacial phenomena

In this section, a number of distinct mechanisms of conductivity enhancement of composites are summarized. The processes that may be contributing to the conductivity increase by the dispersion, have been classified into two categories: (a) interfacial mechanisms which lead to enhanced conduction along the matrix-particle interface, and (b) matrix phenomena where the second phase (insulator) modifies the conductivity in the matrix phase such that the enhanced conductivity path need not be restricted to follow the interface.

3.1.1 Interfacial mechanisms

There are three possible processes that may lead to enhanced conduction along the interface between the conduction matrix phase and the dispersed second phase. Of these the formation of a space charge layer is the most widely studied and accepted mechanism.

(a) Space charge layer conduction

At thermodynamic equilibrium, most internal interfaces and free surfaces of an ionic crystalline material would be expected to have some net charge. This charge interface is compensated with a diffuse layer which contains an excess of oppositely charged point defects of ions. An enhanced conductivity would attributed to the excess concentration of the defects in the

diffuse layer named as the space charge layer or double layer. The spatial extent of the diffuse layer is characterized by the Debye length at the interface between two particles. Figure 3-2 shows the schematic feature of the space charge layer at the surface of an insulator particle in the conductor matrix. The Debye length, λ, is expressed as follows[2],

$$\lambda = [(8\pi Ne^2/\varepsilon kT)\exp(-E/kT)]^{-1/2}$$

$$= [(8\pi e^2/\varepsilon kT)n(\infty)]^{-1/2} \qquad (3-6)$$

where N is the total number of cation in the conductor per unit volume, ε is the dielectric constant, E is the formation energy of defects and $n(\infty)$ is the concentration of defect in the bulk. The typical value of λ is estimated about hundreds of angstrom. The excess of the conductivity due to the space charge layer would be proportional to the excess charge content in the layer. Jow and Wagner represented the excess conductivity as follows[3,4].

$$\Delta\sigma = \sum_i e\mu_i \Delta n_i(x)dx$$

$$= \sum_i e\mu_i <\Delta n_i> \frac{4\pi r_1^2 \lambda}{(4/3)\pi(r_2^3-r_1^3)} \qquad (3-7)$$

where μ_i is the mobility of i defects, r_1 is the alumina particle radius, r_2 is the half of the average distance between two alumina particles. Average excess density $<\Delta n_i>$ with the thick-
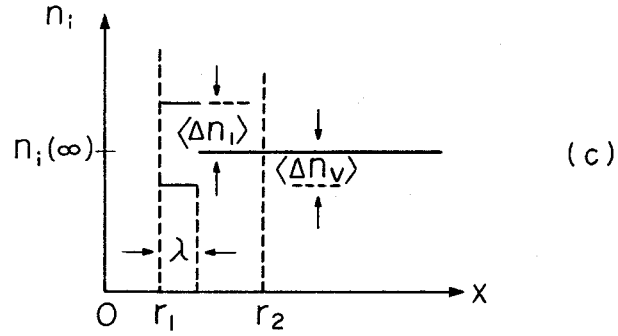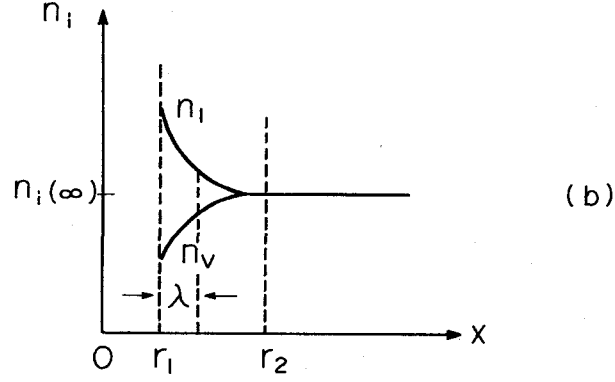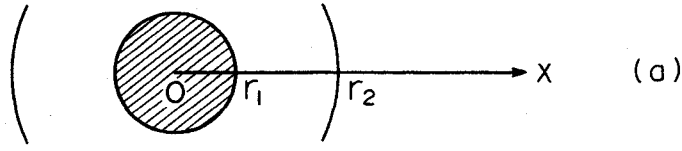
Fig. 3-2 Space charge layer models at the surface of Al_2O_3 particle in the ionic conductor matrix CuCl[3,4]. (a) Schematic cross-sectional view of a single alumina particle of radius r_1 in a CuCl matrix. $2r_2$ is the average distance between two alumina particles. (b) Sketch of the defect concentrations along the x-axis, where F_I (free energy of formation if an interstitial) < F_V (free energy of formation of a vacancy) is assumed. n_i: concentration of interstitials, n_v: concentration of vacancies, λ: Debye length corresponding to the distance where the n_i and n_v fall to $1/e$ from the surface. (c) Sketch of the average excess charge density (Δn_i) in the space charge layer along the x-axis.

ness λ is introduced as the model in fig. 3-2 (c). When $r_2 >> r_1$ is assumed, then $(r_1/r_2)^3 \sim V_v$ and the equation (3-7) can be rewritten as

$$\Delta \sigma = 3 \sum_i e \mu_i < \Delta n_i > \lambda (1/r_1)(V_v/(1-V_v)) \qquad (3-8)$$

At a definite temperature, the excess conductivity $\Delta \sigma$ is proportional to λ and $(1/r_1)(V_v/(1-V_v))$ when it is assumed that $r_2 >> r_1$. This result was compared with the experimental results of CuCl-Al$_2$O$_3$ and LiI-Al$_2$O$_3$ composites in fig. 3-3.
Equation (3-8) fits to the experimental results fairly well in the low concentration of the dispersant. However, the model assumes that the increase of dispersant content leads to a linear increase of space charge layer without consideration of the insulator's blocking effect. This effect is observed in the experimental data as a deviation from the line of equation (3-8) in the high concentration of Al$_2$O$_3$.

Maier has also reported the possible formation of the space charge layers along the interfaces in composite electrolytes[5]. His model is essentially the same as that proposed by Jow and Wagner, and in good agreement with the observed conductivity for composites of AgCl, AgBr and TlCl (fig. 3-4).

Polarization phenomena for the formation of space charge layer is not only induced by the dielectric constant in equation (3-6). Al$_2$O$_3$ particles have the adsorbed species as H$_2$O molecules or OH$^-$ groups on the surface, which affect the ionic conductor contributing the ionic polarization. The effect of the
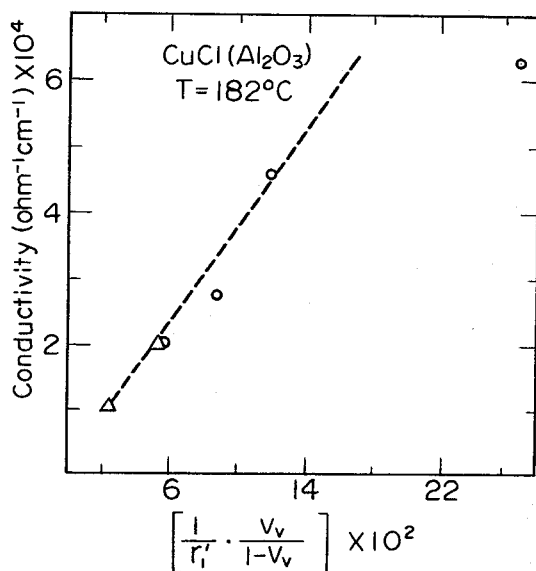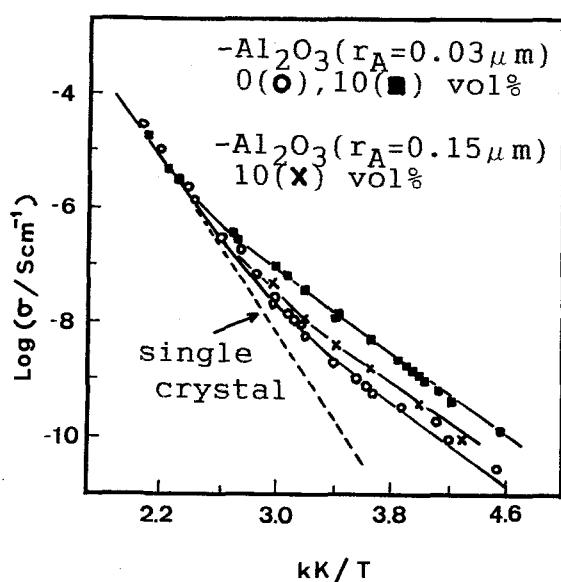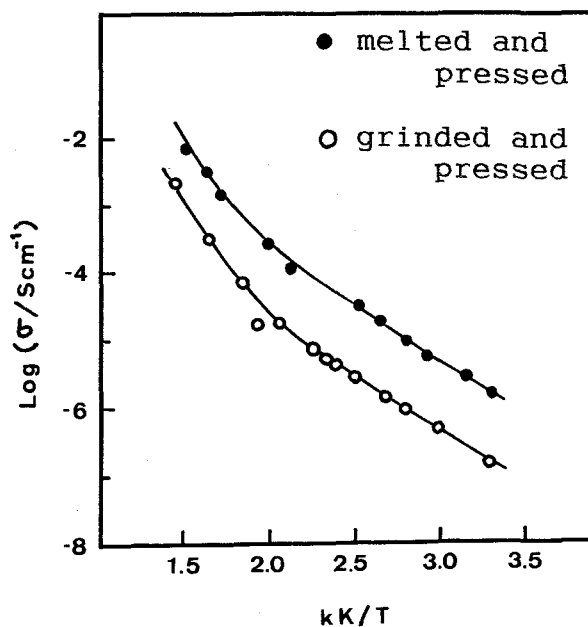
(a)
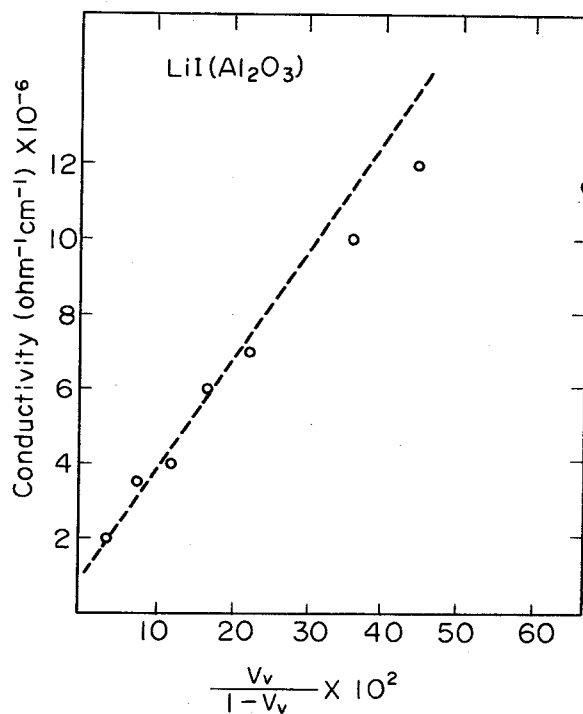
(b)

Fig. 3-3 Comparison of conductivity of experimental and calcu-
lated results.   (a) Plots of conductivity of $CuCl-Al_2O_3$ vs.
$(1/r_1)[(V_v)/(1-V_v)]$ at   a temperature for $182^{\circ}C$. Δ ; $r_1=0.3\mu m$
(exp.), O ; $r_2=0.06\mu m$ (exp.) (b) Plots of conductivity of LiI-
Al_2O_3 vs. $V_v/(1-V_v)$. O ; experimental data of Liang.

Fig. 3-4 Comparison of calculated data with experimental results of (a) TlCl-Al$_2$O$_3$ composite for different volume fractions (0(O), 10(■) vol% ; r$_A$=0.03μm, 10(X) vol% ; r$_A$=0.15μm) of Al$_2$O$_3$, and (b) AgCl-Al$_2$O$_3$ composites with different preparations: ● ; melted and pressed, O ; grinded and pressed. All solid lines are calculated results.

adsorbed species is also described in another mechanism in the later.

Despite their successful models, there are problems applying the space charge layer mechanism to other composite electrolytes. Dudney has estimated the space charge polarization that can be formed at the interface between the ionic conductors, LiI, β-AgI and AgCl, and dispersant[6]. Assuming the defect mobilities near the interface are the same as those in the bulk, integration of the excess defect concentrations gives the excess conductance, C_i along the interface. The relative excess conductance, C_i/σ_b, where σ_b is the bulk conductivity, means the effective width of bulk conduction layer along the interface. In this form, the effect of a space charge layer can be quickly determined by comparing C_i/σ_b with the sample or grain dimension. Table 3-2 summarizes the results of the space charge polarization calculations estimated by Dudney with the selected parameters used in the calculations. Composites of LiI and β-AgI have the largely enhanced ionic conductivities, but the estimations of their C_i/σ_b are extremely small. This result proposes that the alumina and matrix layers can be only 60 A thick in the LiI composite and only 0.5 A thick in the layered β-AgI composite to give a 100 fold enhanced conductivity from the equation in table 3-2. It is clearly unrealistic to attribute the enhanced conductivity observed in the real composites with much larger grain and particle dimensions to such a space charge polarization layer. These calculations suggest that other alternative effects must be considered. In most of space charge layer model, the conductivity enhancement can be due only to enhanced carrier concentration

Table 3-2 Selected parameters and results of interfacial space-charge polarization calculations at 300K.

Mat.	Defect conc.[a]	Mobility Ratio[a]	λ(A)	$C_i/\sigma_b(\mu m)$[b]
AgCl	$[V_{Ag}^-]=[M_{Ag}^+]=7\times10^{-7}$	$\mu_i/\mu_v=470$	245	59
β-AgI	$[V_{Ag}^-]=[Ag_i^+]=2\times10^{-4}$	$\mu_i/\mu_v=23$	13.3	0.0054
LiI	$[V_{Li}^-]=[M_{Li}^+]=7\times10^{-5}$	$\mu_{Li}/\mu_I>>1$	25.5	0.60

[a] Literature references given in 12.

[b] Calculated for accumulation in space-charge layer.

M_{Ag}^+: impurity ion on Ag lattice site

V_{Ag}^-: Ag$^+$ ion vacancy

    AgCl is an extrinsic Frenkel material, β-AgI is documented to be an intrinsic Frenkel material, LiI is an extrinsic Schottky material.
    Conductivity enhancement, x, of the 1 thick film of a conductor by the space charge layer formation is estimated by

$$x = \frac{1 + C_i/\sigma_b}{1} .$$

in the layer. However, it is possible that other mechanisms such as enhanced mobility and/or the presence of an additional phase may contribute to the conductivity enhancement.

(b) Enhanced conduction at the core of the interface

The lattice distortion within the first one to three atomic layers near an interface is likely to make significant changes in the defect mobilities and the defect concentrations. This is the mechanism proposed by Phipps for LiI composite as a result of measurement with LiI film, 0.2 mm thick, sandwiched between silica plates[7,8]. The contribution of interface to the total conductivity of LiI film was separated by subtracting the conductivity through the LiI films from the conductivity measured along the films. The result showed that both the activation energy and pre-exponential terms differed from that of bulk LiI samples, suggesting a new conduction mechanism with rapid ion transport along the core of the interfacial region. The space charge layer model, on the other hand, in which the carrier has almost the same mobility as that of the bulk could explain the experimental results that the activation energy of the enhanced composite does not change compared with the pure material.

This enhancement mechanism within the core of the interface has not been widely accepted because the enhanced conduction layer is restricted to several atomic layers. This is much narrower compared with the space charge layer which is expected to be approximarely hundreds of angstrom wide. If a very thin layer shows the high conductivity, the conduction layer is re-

quired to have a charged, continuous network composed of ionic matrix dispersed with alumina particles with a high surface area. It is probable that microstructural imperfections such as grain boundary and a dislocation layer are the origin of this mechanism.

(c) Interfacial phase formation

In this mechanism, a highly conductive third phase has formed along the interface due to the reaction of the matrix with the dispersed oxide particles or with surface adsorbed species. This possibility has been discussed most widely for composites of LiI and LiBr since these materials are known to form a number of hydration compounds with higher conductivity[9]. Dispersion of wetted Al_2O_3 particles into LiI showed the conductivity increase although the ultra-dry composite did not show the enhanced conductivity[9]. However, the third phase has never been detected by X-ray diffraction. The enhanced conduction mechanism would be more complex than simply the formation of an interfacial layer because all hydrated composites were not always enhanced by the dispersion.

3.1.2 Matrix mechanism

It is possible that the bulk properties at the matrix is affected by the dispersed ion in the second phase. There are several mechanisms by which conductivity through the matrix can be enhanced in the presence of the dispersed phase.

(a) Conduction along grain boundaries and dislocations

The presence of rigid inert particles is known to effect the microstructure that develops during sintering or recrystallization of a material. Therefore, the microstructure of the matrix of the composite may be considerably different from that of the pure material. Dudney also suggests the importance of the lattice defects in the conductor matrix[10]. When the Al_2O_3 fibers were dispersed into AgCl matrix, conductivity was enhanced after deforming or annealing the composite. The fibers would affect the nucleation and grain growth processes as the AgCl recrystallizes, stabilizing a finer AgCl grain structure than can be achieved in annealed pure AgCl. Stabilized fine AgCl grains would form the grain boundary with high conductivity, likewise as in the case of alumina particle dispersion. Model calculations of the conductivity for a composite, where the grain boundaries contribute to the high conduction path, reproduced the experimental observation quite well[10]. In these calculations the grain size is assumed to decrease as the volume fraction of particles increase according to the theoretical relationships between the conductor grain size and the dispersant particle size and the volume fraction[22]. In this model, it is likely that the composite containing 1 vol% of thoroughly dispersed fine particles shows a significant increase in conductivity, which could not be explained by the interfacial models discussed in space charge layer conduction. The enhanced conduction along the grain boundaries may be due to either the enhanced carrier con-

centration or mobility. For the AgCl composites, it is conceivable that the enhanced conduction is mainly due to the formation of a space charge layer along the grain boundaries. However, the composites of either LiI or β-AgI, in addition to the formation of space charge layer, would need to consider this mechanism along the grain boundary.

(b) Formation of metastable phase with a high conductivity

The presence of second-phase particles in a composite may in some materials act as factor of stabilization for a metastable phase or a higher-temperature matrix phase formed during the processing[11,12]. There are some experimental results which suggest that the metastable (gamma) phase of AgI might be present in the alumina composites although the AgI matrix has generally been assumed to be the stable low temperature beta structure. Gamma phase of AgI which is a more conductive compound compared to beta phase may be responsible for the enhanced conductivity of the composites. The existence of metastable gamma phase was also confirmed by X-ray diffraction when the beta phase of AgI was cold pressed.

3.2 Dispersion of ferroelectric materials

In the previous section, it was clarified that the interfacial mechanism in which the space charge layer was formed at the interface between the conductor matrix and insulator particles was widely accepted for the support of enhanced conductivity. Equation (3-6) showed that the space charge layer depends on the dielectric constant. According to this model, ferroelectric materials, PZT and $BaTiO_3$, with the dielectric constant (ε) of $\sim 10^4$ and $\sim 10^3$, respectively, are probable as the dispersants for ionic conductor. When the ferroelectric particles contact with ionic conductors by dispersion, they would induce the dielectricity in the conductor by the interaction at the interface indicating the lager ε in equation (3-6). In particular, we applied the $BaTiO_3$ particles with different particle size and dielectric constant to investigate the effect of the amount of dielectric constant on the enhanced conductivity.

The ionic conductor used for enhancing the conductivity is a sodium ion conductor, $Na_4Zr_2Si_3O_{12}$ (NZS), which is one of the end members of sodium super ion conductor NASICON ($Na_{1+x}Zr_2Si_xP_{3-x}O_{12}$). The ionic conductivity of NZS is lower than that of intermediate NASICON because the sodium ion sites are completely occupied and it is difficult for Na^+ ions to migrate easily. Therefore,it would be needed to increase the vacant sites in the lattice structure in order to increase the ionic conductivity. By the dispersion of insulator particles into the NZS, it is expected that space charge layer formed at the interface could prepare the vacant sites for Na^+ ion migration. Ionic

conductor NZS, whose sites are completely occupied by Na^+ ions, would be the most promising conductor to observe the great enhancement of conductivity on the NASICON type conductors.

3.2.1 Dispersion of ferroelectric PZT

*** experimental ***

NZS was prepared either by a conventional solid state reaction named mechanical mixing NZS or a coprecipitation method named sol-gel NZS.   Starting materials, Na_2SiO_3, $ZrO(NO_3)_2 \cdot 2H_2O$, SiO_2 were mixed in a stoichiometric proportion (Na:Zr:Si=4:2:3) in both methods.   The mechanical mixing NZS was obtained by a repeated sintering of dry powder mixed with mortar or ball mill at $1200^O C$ for 6 hours.   In the coprecipitation method, the aqueous solutions of Na_2SiO_3 and $ZrO(NO_3)_2 \cdot 2H_2O$ were mixed together to precipitate, subsequently slurried by elimination of some water after mixing with insoluble SiO_2 fine powder.   A sample precursor was obtained by drying this slurry slowly in a rotary evaporator at $80^O C$.   The NZS was obtained by repeated sintering of the precursor at $1100^O C$ for 6 hours.   These sintering conditions were determined experimentally by optimization of sintering temperature and sintering time.   Repetition of sintering was effective to reduce the second-phase such as ZrO_2, Na_2ZrSiO_5, $Na_2ZrSi_2O_7$ and others, and to enhance the crystallinity.

Dispersed ferroelectric PZT ($Pb_{0.95}Sr_{0.05}Ti_{0.46}Zr_{0.54}O_3$) was produced by Japan Storage Battery Co.   This PZT has a temperature dependent dielectric constant (ε) with a maximum at $370^O C$, however, ε was in the order of 10^4 over the temperature range

between 0 and 500°C. The dispersant was mixed with NZS mechanically in a mortar at room temperature. All composites were identified by XRD; no other peaks than those of NZS and the dispersed PZT were observed even in a pellet after sintering.

The sample powder was pressed into a pellet with a pressure of 255 MPa in a 10 mm diameter steel die and was sintered at 1000°C for 2 hours. Gold electrodes were formed from an Engelhard A-3360, which was decomposed and hardened by raising the temperature to 600°C over period of 20 minutes.

The ac conductance was measured by inspection of the complex admittance plot obtained with a Hewlett-Packard 4192A impedance analyzer in the frequency range of 5Hz to 500kHz. The contact resistance of 600 mΩ was measured with a Hewlett-Packard 4328A milliohmmeter, which is negligible small compared with the measured resistance of the sample pellet.

*** Result ***

Ionic conductivity of Na$_4$Zr$_2$Si$_3$O$_{12}$

Figure 3-5 shows the Arrhenius plot of ionic conductivities of NZS by solid state reaction and coprecipitation methods. The mechanical mixing NZS showed the activation energies of 64 kJ/mol and ~40 kJ/mol prepared by mortar and ball mill, respectively. This difference would come from the difference of particle size of powder before firing. For the sol-gel NZS, the activation energy is ~37 kJ/mol. Transmittance electron microscopy (TEM) has shown that the coprecipitated NZS particles are smaller than the mechanical mixing NZS particles (fig. 3-6), suggesting that the nucleation rate of the precursor is faster than that of
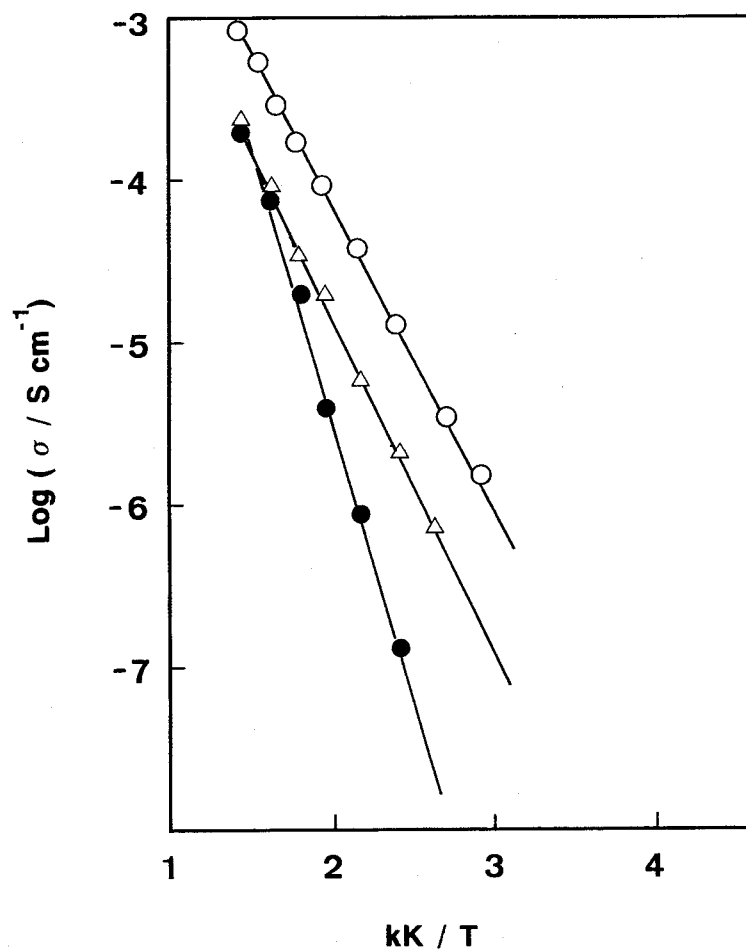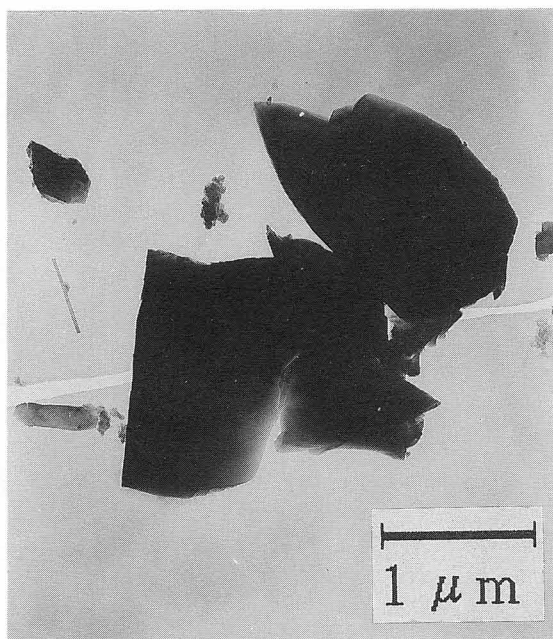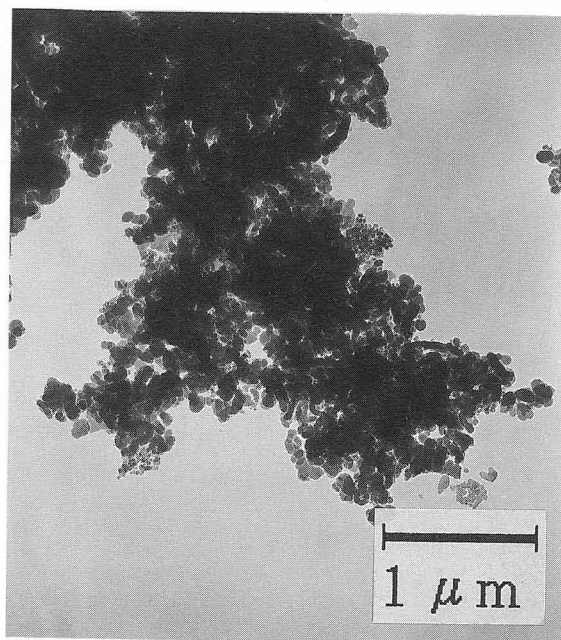
Fig. 3-5   Temperature dependence of ionic conductivity of mechan-
ical mixing NZS by mortar (●), by ball mill (△) and sol-gel
NZS (○).

(a)

(b)

Fig. 3-6 Transmittance electron microscophy (TEM) photographs of
(a) mechanical mixing NZS and (b) sol-gel NZS.

crystal growth in the solution. This observation is consistent with the fact that lower sintering temperatures are adequate to prepare the sol-gel NZS. If a sintered pellet consists of bulk region and grain boundary region, the sol-gel NZS pellet would contain a larger portion of grain boundary region in comparison with the mechanical mixing NZS pellet. This suggests that the overall conductivity, σ_t, of a sintered pellet should also be divided into two parts, i.e., the bulk conductivity, σ_b, and the grain boundary conductivity, σ_{gb},

$$\sigma_t \rightarrow \sigma_b + \sigma_{gb} \qquad\qquad (3-9)$$

The higher conductivity in sol-gel NZS should be attributed mainly to the grain boundary conduction, as a capacity of 100 pF/cm in a parallel RC element equivalent circuit, which is a typical value for grain boundary conduction[13], was observed in the complex impedance semicircle. In the mechanical mixing NZS, fraction of grain boundary would be small compared with the sol-gel NZS in a pellet. Furthermore, surface condition of the particle, which depends on the preparation condition, would effect on the grain boundary conduction. This is the cause of the conductivity difference between mechanical mixing NZS by ball mill and sol-gel NZS although they are almost the same in particle size and in activation energy.

Conductivity of NZS dispersed with PZT

Enhanced conductivities of mechanical mixing NZS by the

dispersion of PZT are shown in fig. 3-7 as a function of PZT content. They show activation energy changes with PZT content. By the addition of PZT, the conductivity is enhanced by nearly two orders of magnitude at the maximum point, and the activation energy decreases from 64 kJ/mol to 37 kJ/mol.

The conductivity increase and the decrease of activation energy with the increase of PZT (0-40 mol%) indicates the increase of the fraction of interfacial conductivity which is added into the basic bulk and grain boundary conductivity (fig. 3-8). This is represented by the modification of equation (3-9) as

$$\sigma_t \longrightarrow \sigma_b + \sigma_{gb} + \sigma_{int} \qquad\qquad (3\text{-}10)$$

When the electrical insulator was dispersed into NZS in a pellet, σ_b and σ_{gb} will be reduced. Since the experimental results show electrical conductivity (σ_t) enhancement, the third component, σ_{int}, has to increase greatly compared with σ_b and σ_{gb} reductions. In the region of 40 to 70 mol%, the conductivity has been further enhanced, but the apparent activation energy has converted to a slight increase with increase of PZT content. It is considered that this increase of apparent activation energy is the result of a compensation at lower temperatures of the conductivity enhancement by a reduction in the effective cross-sectional area for conduction. A sharp decrease of conductivity occurred in increasing the PZT content further to 70-80 mol%, while the activation energy almost unchanged. This means that the decrease of σ_b and σ_{gb} are larger than the increase of σ_{int}.

In comparison, fig. 3-9 shows the conductivity increase of
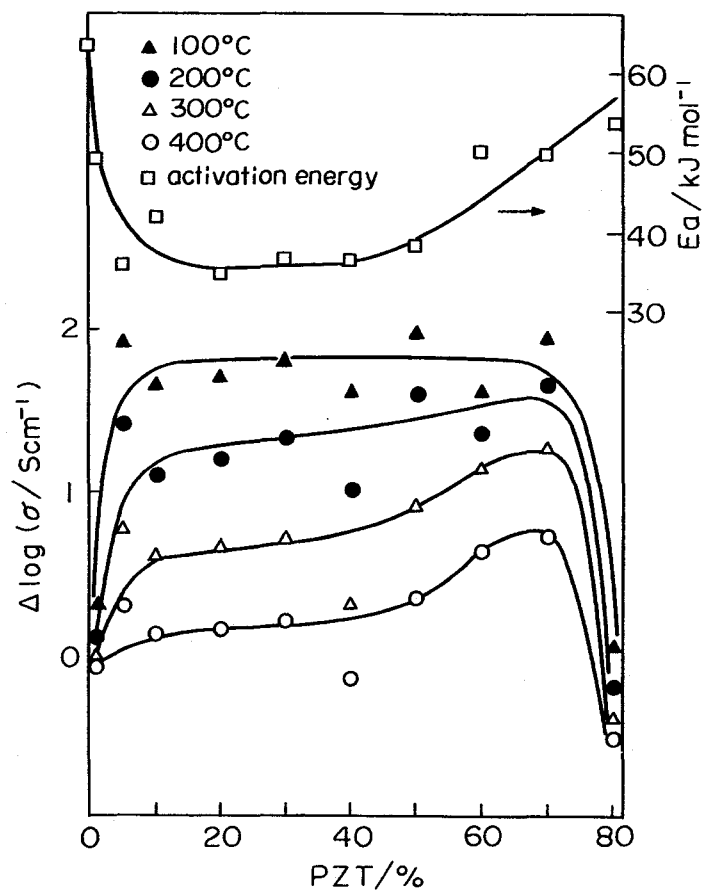
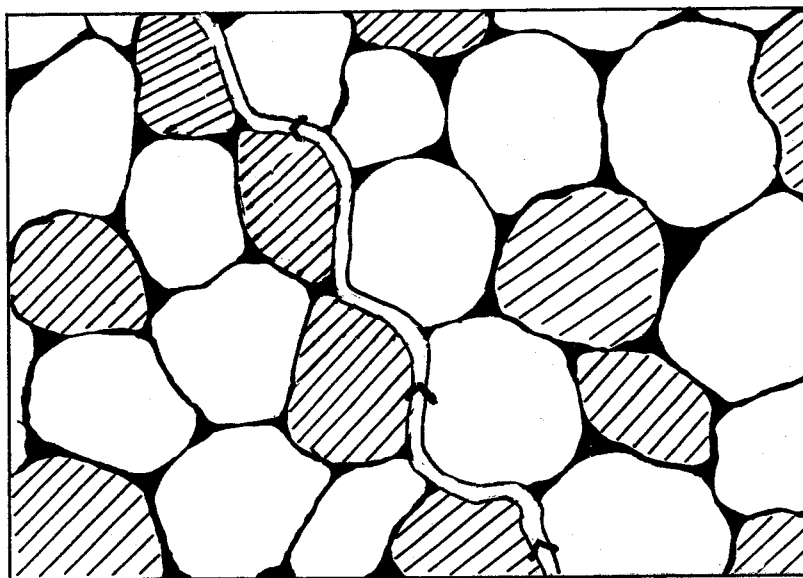Fig. 3-7 Conductivity increase of mechanical mixing NZT as a function of dispersed PZT content.

Fig. 3-8 A model of composite pellet, (☐) NZS particle; (▨) PZT particle; (➤) interfacial conduction path between NZS and PZT particles.
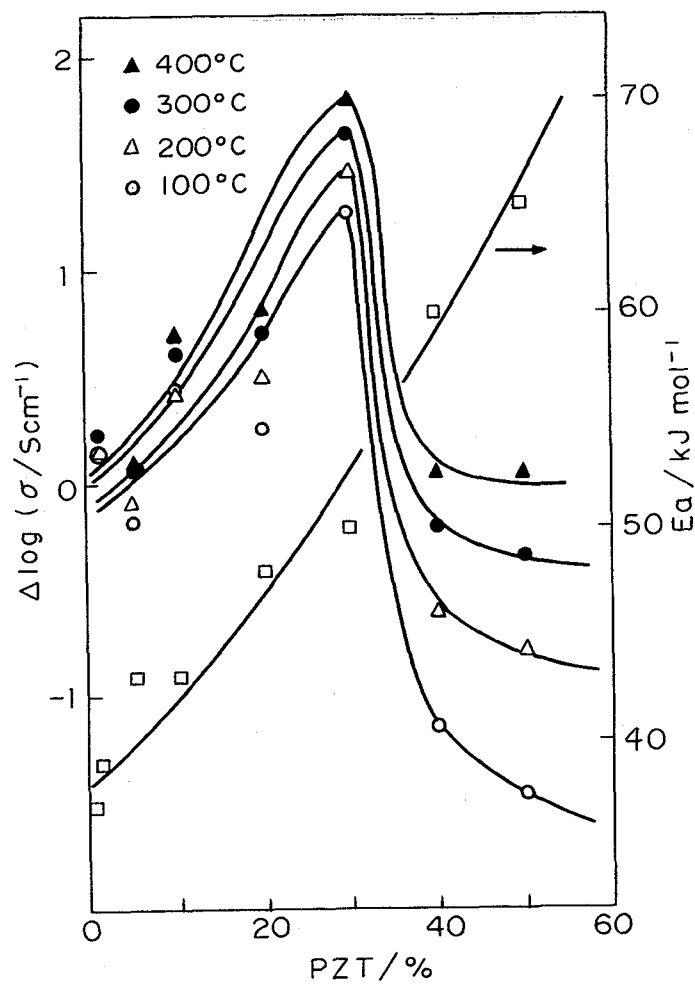
Fig. 3-9 Conductivity increase and activation energy (E_a) of sol-gel NZS as a function of dispersed PZT content.

sol-gel NZS as a function of dispersed PZT content. The conductivity passes through a maximum at 30 mol% PZT in the observed temperature ranges between 50 and 450^OC. The magnitude of enhancement is almost temperature independent while the enhancement in the conductivity of mechanical mixing NZS at low temperature (100^OC) is greater than that at high temperature (400^OC). This shows that the conduction mechanism of interfacial conductivity is similar to that of grain boundary conductivity. However, a sharp decrease of conductivity has also been observed when more than 30 mol% PZT was added with the increase of E_a.

3.2.2 Dispersion of ferroelectric $BaTiO_3$

*** experimental ***

The ferroelectric $BaTiO_3$ as a dispersant was prepared by a conventional solid state reaction. $BaCO_3$ and TiO_2 were mixed 1:1 molar ratio and fired at temperatures of 800, 1000, 1200 and 1400^OC, for 6 hours. The prepared $BaTiO_3$ with each temperature was pressed into a pellet of 10 mm diameter and was sintered to measure the dielectric constant.

*** results ***

Dielectric constant of $BaTiO_3$

It is known that dielectric constant of $BaTiO_3$ ceramics closely depends on the particle size which is easily controllable by firing temperature. Also, the temperature dependence of dielectric constant is large and unique.
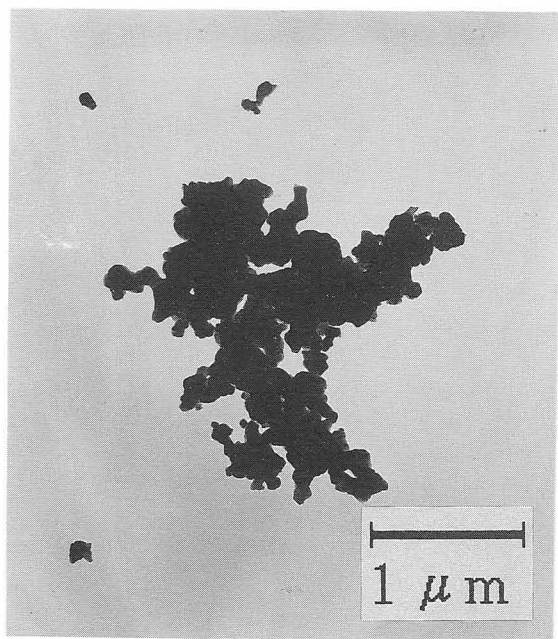
The transmittance electronic microscopy (TEM) photographs of

BaTiO$_3$ with several particle sizes are shown in fig. 3-10. BaTiO$_3$ shows the particle growth with increasing firing temperature. The average particle size is 0.3, 0.5, 0.9 and 5 μm for the firing temperature of 800, 1000, 1200 and 1400°C, respectively.

Figure 3-11 represents the comparison of dielectric constant (ε) of these obtained BaTiO$_3$ as a function of particle size. Among the four BaTiO$_3$ with different firing temperature, BaTiO$_3$ ceramic with the particle size of 0.9 μm showed the maximum dielectric constant. The dielectric constant of each BaTiO$_3$ depends on the temperature, which is shown in fig. 3-12 for BaTiO$_3$ fired at 1200°C. All four BaTiO$_3$ showed the phase transition at 135°C where maximum dielectric constant was obtained.

Figure 3-13 shows the conductivity enhancement as a function of BaTiO$_3$ content in the composite. It is clear that the maximum enhancement is obtainable at 5 mol% BaTiO$_3$. This dependence is completely different from that of PZT dispersion. Also, this is not similar to the case of halide-alumina in which maximum enhancement is observed at 20-40 vol% alumina. Yamamoto et al.[14] have reported in the system LiI-PLZT the maximum enhancement at 1.8 mol% dispersant.

When 0.9 μm BaTiO$_3$ particles were dispersed into NZS matrix, maximum enhancement was observed in the vicinity of phase transition temperature. Figure 3-14 represents the enhancement against dielectric constant ε for both sol-gel NZS and mechanical mixing NZS. On the other hand, fig. 3-15 shows the plots of conductivity enhancement against particle size of BaTiO$_3$ showing similar dependence as in fig. 3-11 in the case of sol-gel NZS.
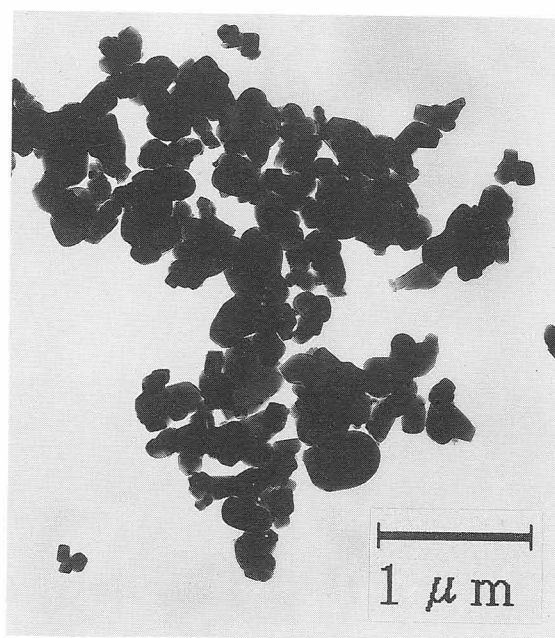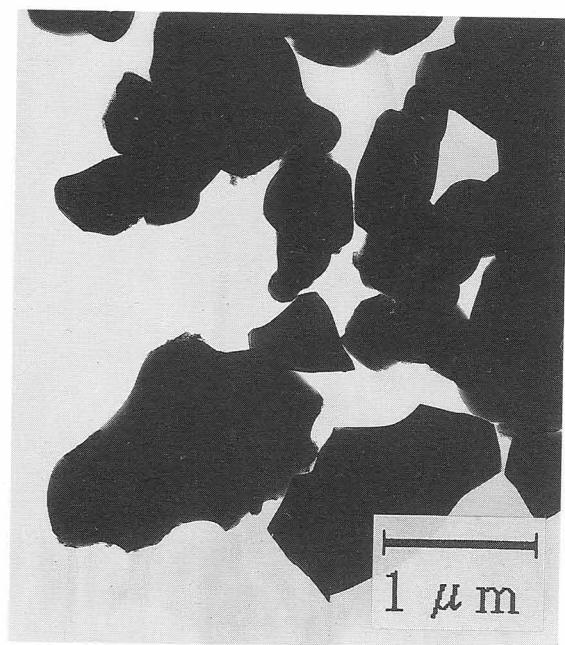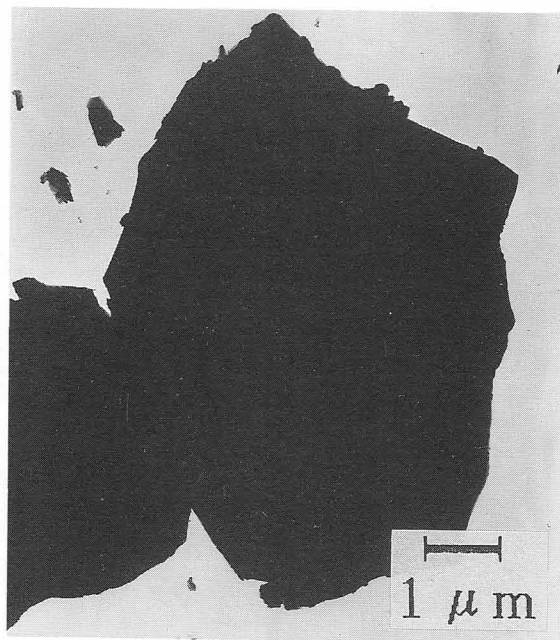
Fig. 3-10 Transmittance electronic microscopy of $BaTiO_3$ fired at
(a) 800°C, (b) 1000°C, (c) 1200°C and (d) 1400°C.
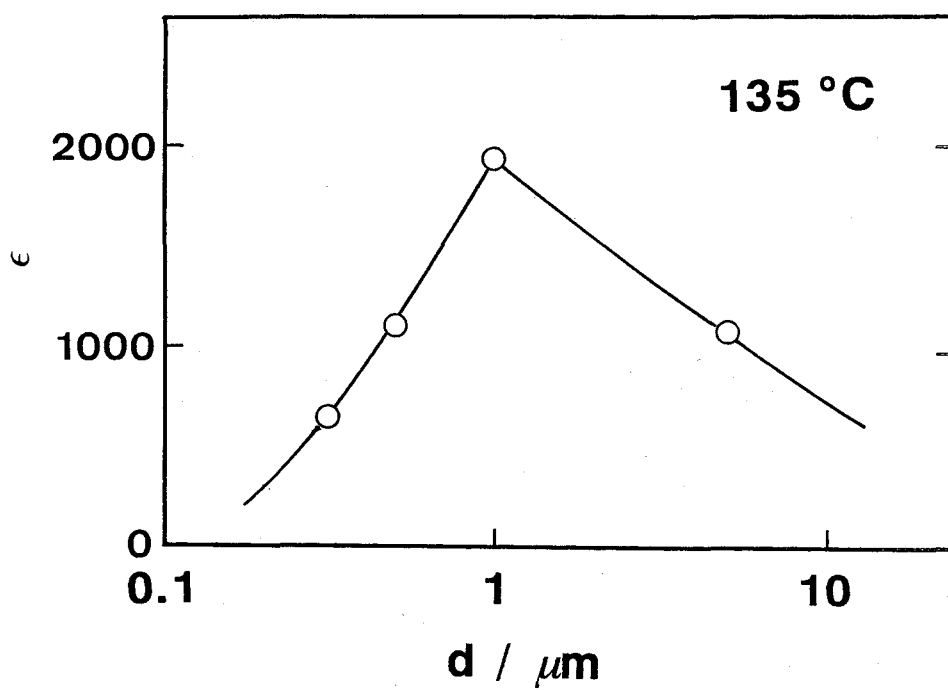
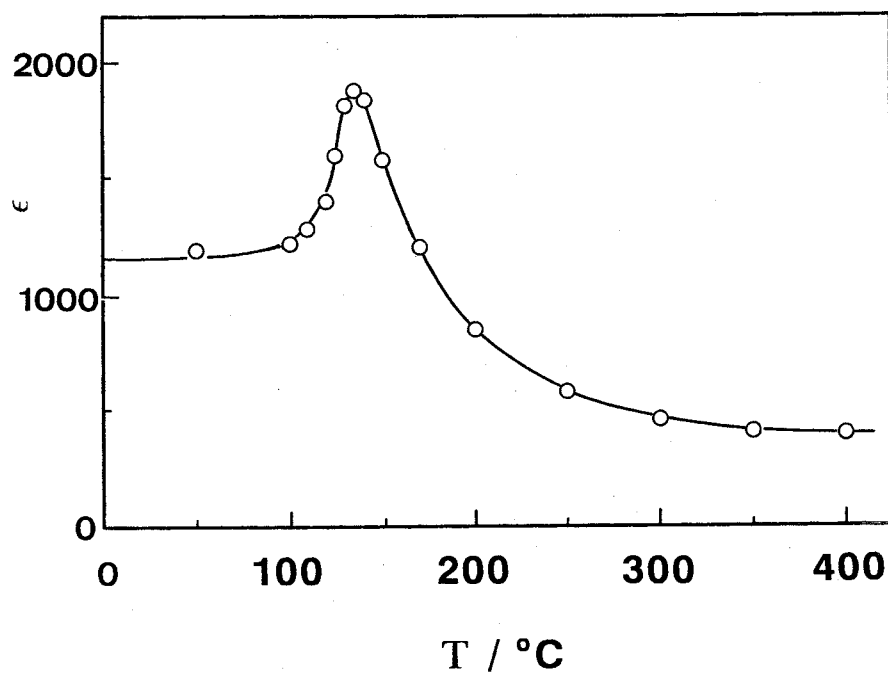Fig. 3-11 Dielectric constant of BaTiO₃ at 135°C as a function of particle size of BaTiO₃.

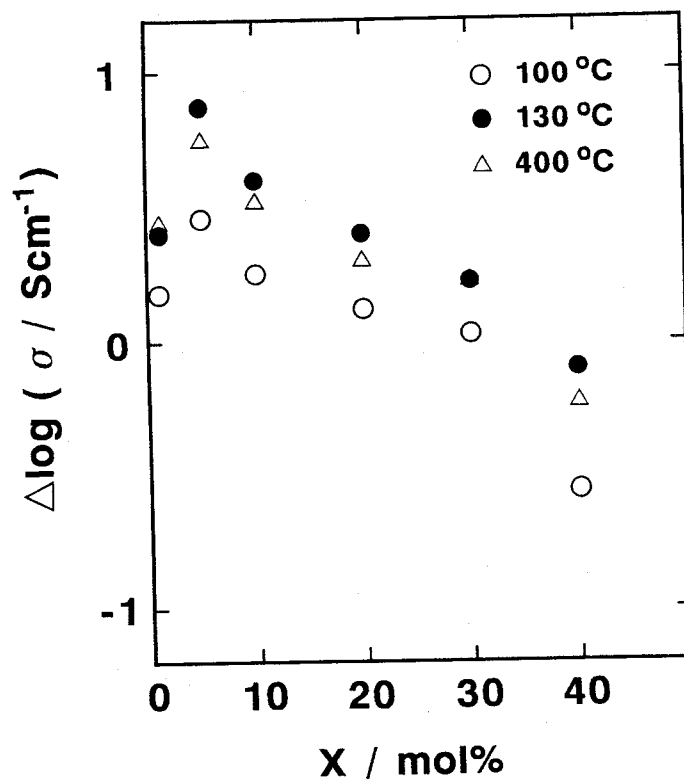Fig. 3-12 Temperature dependence of dielectric constant of BaTiO$_3$ with the particle size of 0.9 μm.

Fig. 3-13 Electrical conductivity enhancement of sol-gel NZS as a function of molar concentration of dispersed BaTiO$_3$ at 100°C (O), 130°C (●) and 400°C (△).
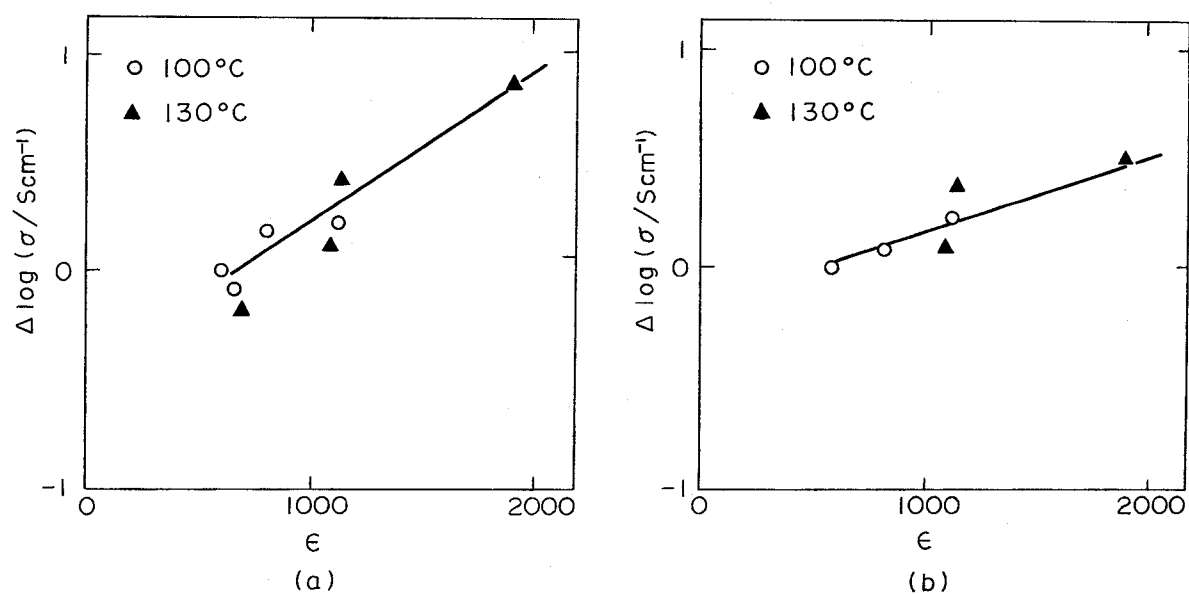
Fig. 3-14 Electrical conductivity enhancement of (a) sol-gel NZS and (b) mechanical mixing NZS as a function of dielectric constant of $BaTiO_3$ of four different particle sizes at $100^{\circ}C$ (O) and at $130^{\circ}C$ (▲).
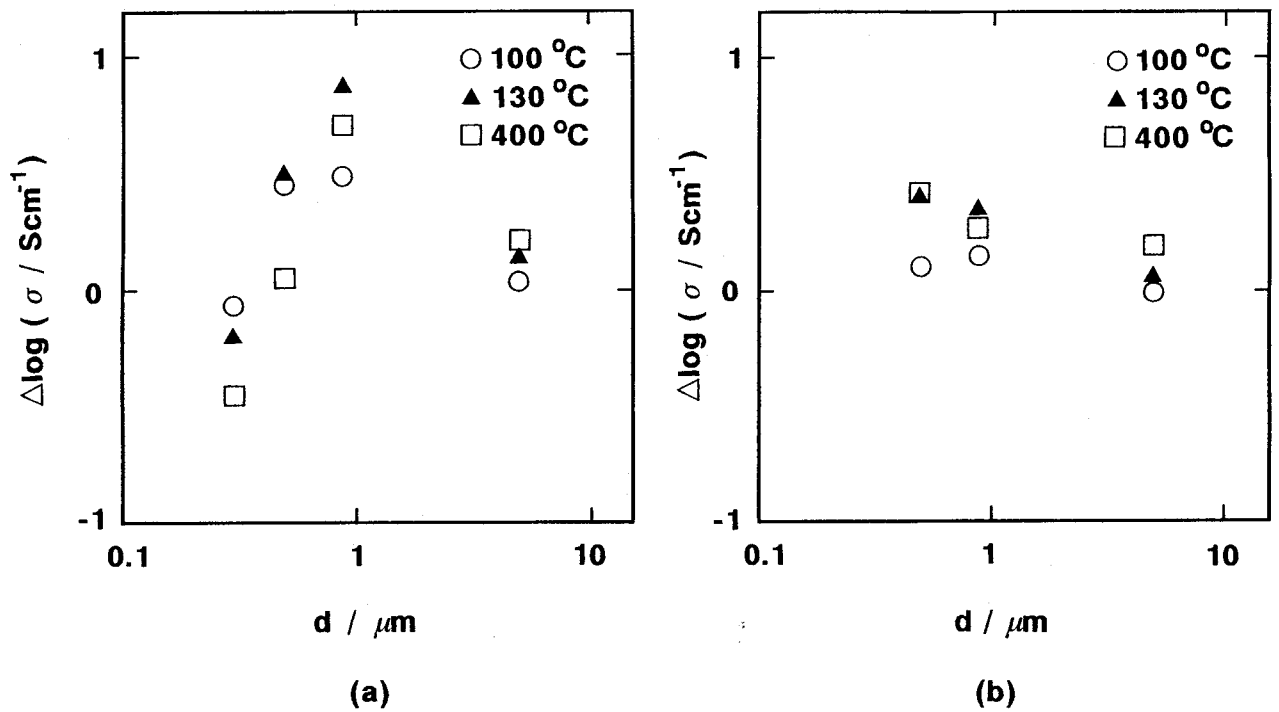
Fig. 3-15 Electrical conductivity enhancement of (a) sol-gel NZS and (b) mechanical-mixing NZS as a function of particle size of dispersed $BaTiO_3$ of four different particle sizes at $100^{\circ}C$ (O), at $130^{\circ}C$ (▲) and at $400^{\circ}C$ (□).

From these data, the enhancement has a dependence on ε, rather than on particle size. In many cases of halide composite, however, smaller particles in the submicron region of the dispersant can enhance largely.

The author has found the existence of the effect of ε of dispersant on the ionic conductivity enhancement of NZS. In addition, it is needed to consider the surface condition of dispersed particles to compare the difference of the enhancement between the cases of PZT and $BaTiO_3$ dispersion. The effect of adsorbed species would be described in the next section.

3.3 Dispersion of solid superacid materials

As is mentioned in the first of this section, it is probable that the adsorbed OH^- groups and/or H_2O molecules of the dispersant particles contribute to the defect formation resulting in the enhanced conductivity. Maier has suggested that the attractive interaction in $AgCl/Al_2O_3$ composite may occur between Ag^+ ions and acidic sites of OH^- and H_2O on Al_2O_3 particles. It is reasonable to consider that the acid-base interaction at the interface would create the expanded space charge layer leading to the high conductivity. Following this concept, it may be expected that solid superacid particles, which have the acidic sites stronger than 100% sulfuric acid on the surface, would be more effective for the formation of Na^+-ion vacancies since the acidic sites attract electrons on oxygens consequently inducing the Na^+ ions on the particle surface.

3.3.1 Dispersion of solid superacid SO_4^{2-}/ZrO_2

*** experimental ***

Solid superacid SO_4^{2-}/ZrO_2 was prepared after Hino et al.[15].About 30 ml of 1 $mol\,dm^{-3}$ H_2SO_4 was poured over the 2g of $Zr(OH)_4$ powder. Strong acidity was developed on the surface of ZrO_2 particles (SO_4^{2-}/ZrO_2) by heat treatment. Acid strength was examined by yellow colour change of a sample immersed into a sulfuryl chloride solution containing indicators, m-nitrotoluene ($pK_a=-11.99$), nitrobenzene (-12.14), p-nitrofluorobenzene (-12.44), p-nitrochlorobenzene (-12.70), m-nitrochlorobenzene (-13.16), 2,4-dinitrotoluene (-13.75), 2,4-dinitrofluorobenzene (-14.52), 2,4,6-trinitrotoluene (-15.60) or 1,3,5-trinitrobenzene (-16.04).

*** Results ***

An acidity of $H_0<-16$ was developed in SO_4^{2-}/ZrO_2 heat treatment at 650°C. The acidity was dependent on the treatment temperature. Although the NZS with SO_4^{2-}/ZrO_2 should be sintered at 650°C for pelletization to maintain the lowest H_0 (highest acidity), a higher temperature of 1000°C was applied in order to obtain a pellet with sufficient mechanical strength for conductivity measurement. When the H_0 of crushed powder of this pellet was measured, $H_0<-16$ was maintained, though the amount of acidic sites was reduced.

The conductivities of NZS with SO_4^{2-}/ZrO_2 are also shown in fig. 3-16 and 3-17. Both composites of the mechanical mixing NZS and the sol-gel NZS show obvious enhancement of the conductivity.
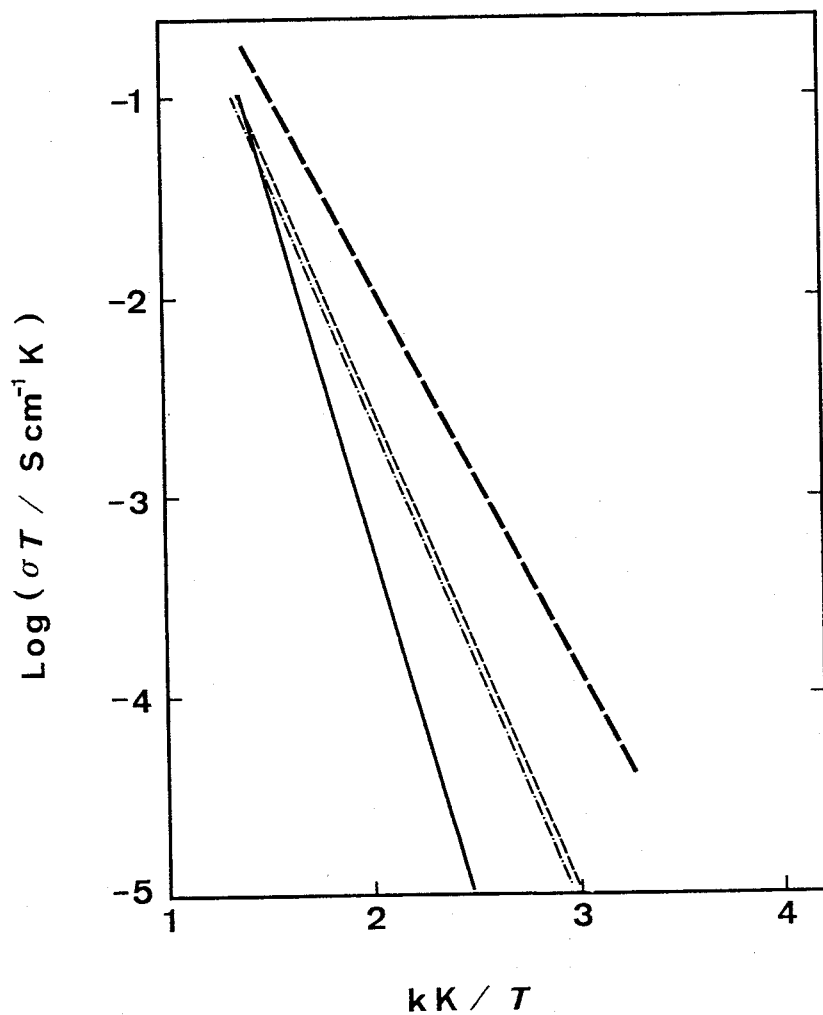
Fig. 3-16   Temperature dependence of ionic conductivity of me-
chanical-mixing NZS: (——) NZS without SO_4^{2-}/ZrO_2;   (——)
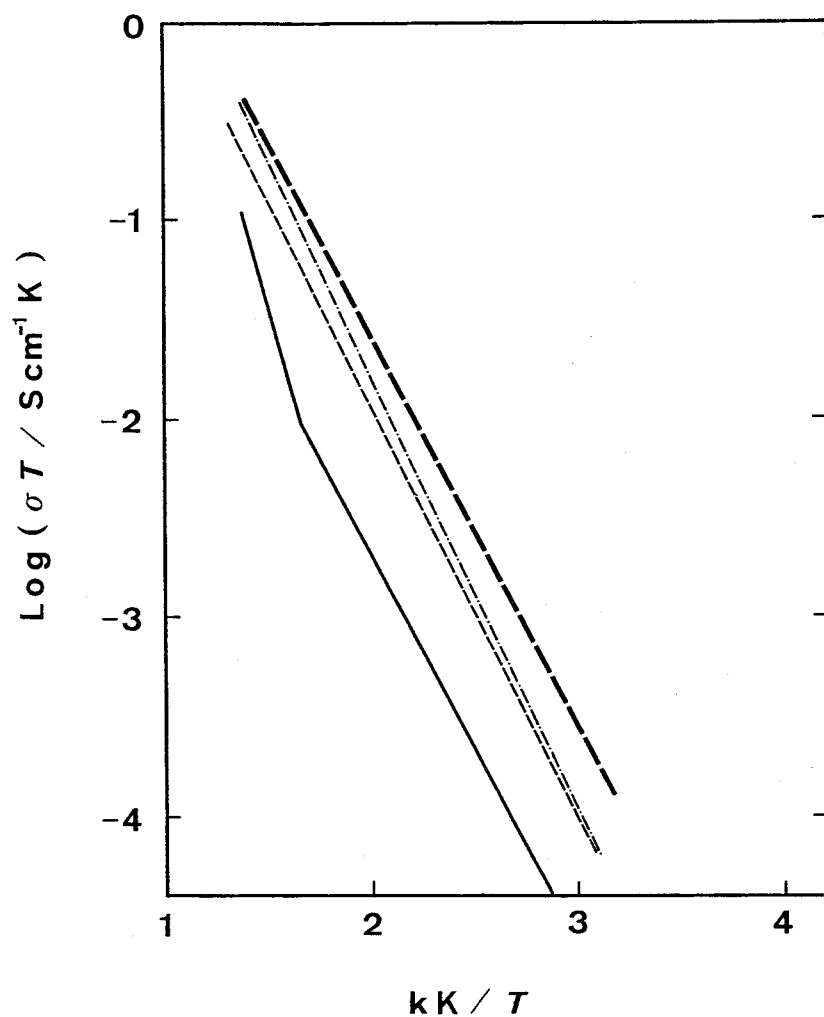NZS+40mol%SO_4^{2-}/ZrO_2;   (——) NZS+70mol%SO_4^{2-}/ZrO_2;   (—·—·—)
NZS+80mol%SO_4^{2-}/ZrO_2.

Fig. 3-17 Temperature dependence of ionic conductivity of sol-
gel NZS. (———) NZS without SO_4^{2-}/ZrO_2; (———) NZS+20mol%SO_4^{2-}
/ZrO_2; (———) NZS+40mol%SO_4^{2-}/ZrO_2; (———) NZS+50mol%SO_4^{2-}/ZrO_2.

In the mechanical mixing NZS with the dispersion of SO_4^{2-}/ZrO_2, the apparent activation energy, E_a, was decreased depending on the SO_4^{2-}/ZrO_2 content, up to 70 mol%. In contrast, in the case of sol-gel NZS with SO_4^{2-}/ZrO_2, the activation energy was almost independent of the SO_4^{2-}/ZrO_2 content. These defferences in the magnitude of conductivity enhancement and the change of E_a between the mechanical mixing NZS and the sol-gel NZS with SO_4^{2-}/ZrO_2 might be explained as follows.

The author has already described in section 3-2 that the relative contribution of σ_b to σ_t would be greater than that of σ_{gb} in the pellet of mechanical mixing NZS. The addition of SO_4^{2-}/ZrO_2 forms many interfacial contacts between NZS and SO_4^{2-}/ZrO_2 particles.

Figure 3-18 and 3-19 show the dependence of the conductivity enhancement on the molar concentration (x) of dispersant SO_4^{2-}/ZrO_2. In the mechanical mixing NZS with SO_4^{2-}/ZrO_2 (fig. 3-18), the conductivity enhancement at every temperatures passes through a maximum at x=70%. The enhancement of two orders of magnitude at 100°C was observed at the maximum. Figure 3-19 shows that the maximum enhancement (one order of magnitude) was observed at x=40% in all temperatures in the sol-gel NZS dispersed with SO_4^{2-}/ZrO_2.

The dependence of conductivity enhancement on SO_4^{2-}/ZrO_2 content might be explained when equation (3-10) and the model of Fujitsu et al.[16] as shown in fig. 3-8 are assumed. The compositional dependence of σ_{int} is roughly divided into three regions (fig. 3-20). (1) When x is small, i.e., 0-10% SO_4^{2-}/ZrO_2 (region I), the increasing rate of σ_{int} is expected to be sharp,
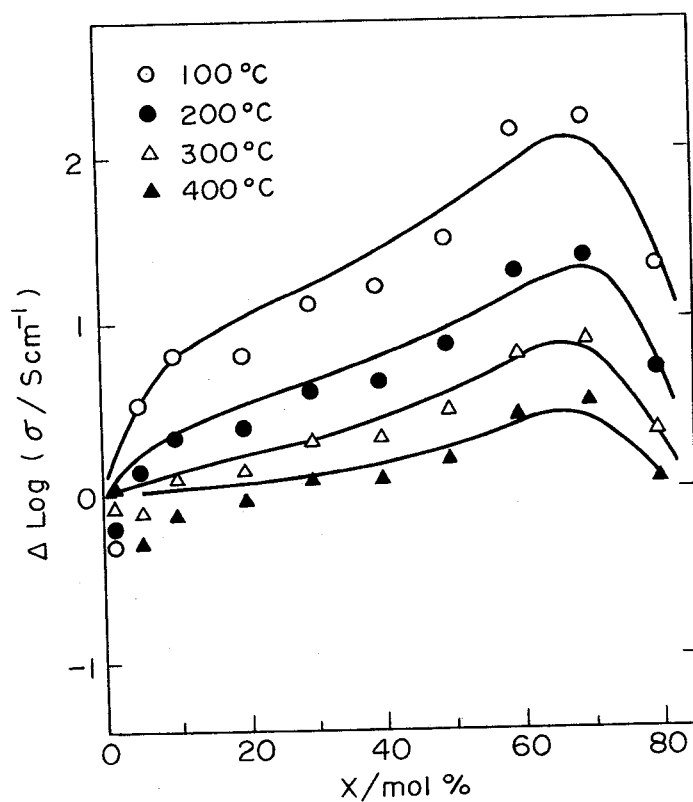
Fig. 3-18   Conductivity enhancement of mechanical-mixing NZS as
a function of the molar concentration (x) of dispersant SO_4^{2-}
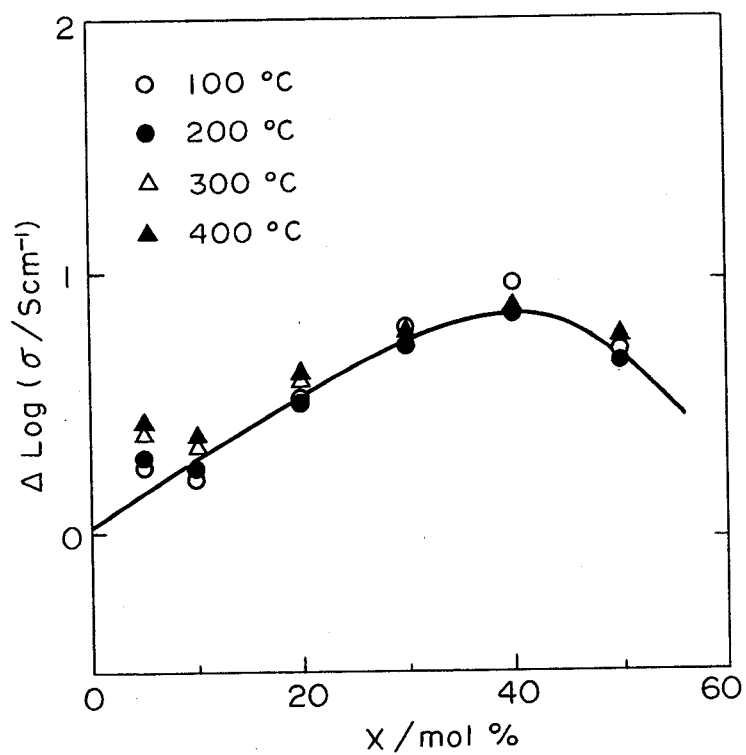/ZrO_2:   (O) 100°C;   (●) 200°C;   (△) 300°C;   (▲) 400°C.

Fig. 3-19 Conductivity enhancement of sol-gel NZS as a function of the molar concentration (x) of dispersant SO_4^{2-}/ZrO_2: (O) $100^{\circ}C$; ($\bullet$) $200^{\circ}C$; ($\triangle$) $300^{\circ}C$; ($\blacktriangle$) $400^{\circ}C$.
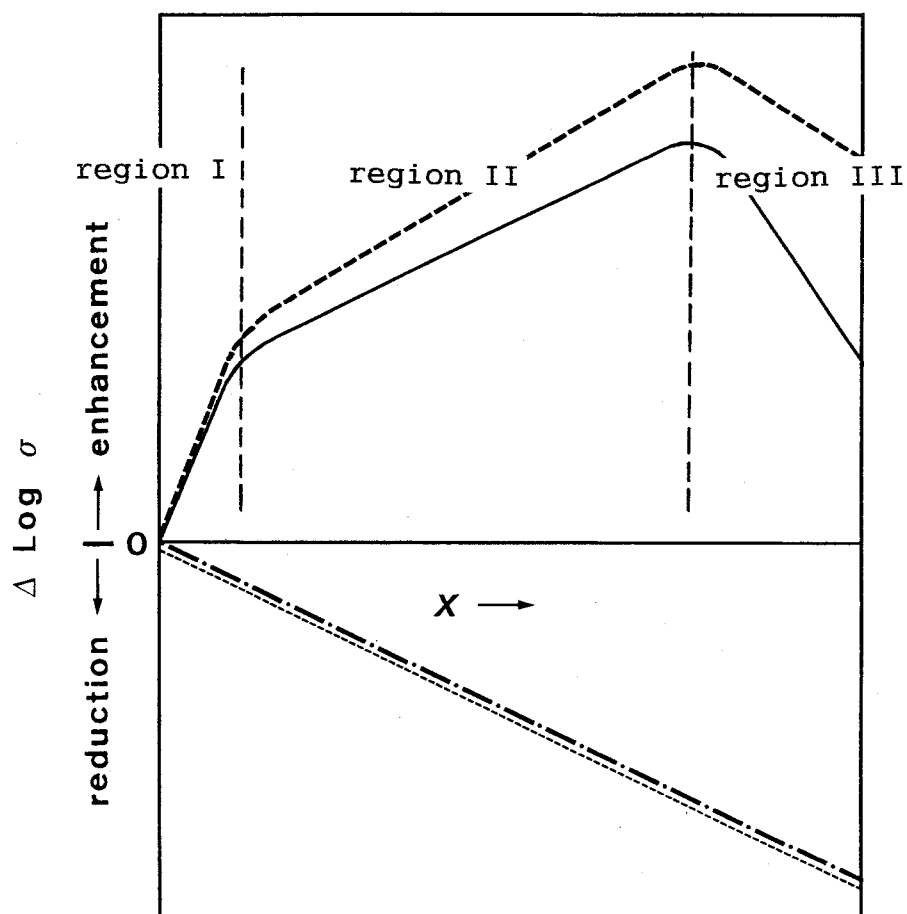
Fig. 3-20 Deviations of overall (σ_t: ——); bulk (σ_b: —·——·—·);
grain boundary (σ_{gb}: -------); and interfacial (σ_{int}: —————·); con-
ductivities from those of NZS without dispersant as a function of
added molar concentration (x) of SO_4^{2-}/ZrO_2. Both vertical and
horizontal axes are denoted by arbitrary scale.

since every contact area between NZS and SO_4^{2-}/ZrO_2 particles is effective to enhance σ_{int}. (2) When x is large, i.e., 70-100% SO_4^{2-}/ZrO_2 (region III), σ_{int} would be reduced sharply with increasing x, because almost all particles in the pellet should consist of insulator SO_4^{2-}/ZrO_2. (3) In the intermediate region, x=10-70% (region II), the interface area between NZS and SO_4^{2-}/ZrO_2 particles would increase with increasing x. However, the increasing rate of interfacial area will not be so sharp as that in the small x region (region I), because the effective number of SO_4^{2-}/ZrO_2 particles surrounding NZS particles would be reduced. That is, the SO_4^{2-}/ZrO_2 particles which could not contact NZS particles would increase with incresing x. A maximum value in σ_{int}, therefore, would be observed in this region.

The fact that the experimental result of compositional dependence of the enhancement shown in fig. 3-18 qualitatively agreed with the dependence of σ_t in fig. 3-20, suggests that the existence of interfacial layer with high Na^+-ion conductivity is plausible.

Enhancement mechanism by SO_4^{2-}/ZrO_2 addition

The observed specific dielectric constant of solid superacid SO_4^{2-}/ZrO_2 was 13, comparable with 12 of Al_2O_3 and 14 of non-H_2SO_4-treated ZrO_2 prepared from $Zr(OH)_4$. This suggests that surface adsorbed SO_4^{2-} groups or Lewis acid oxygens do not affect the dielectric constant. The conductivity of NZS with a dispersion of Al_2O_3 or ZrO_2 is shown in fig. 3-21 and 3-22. Only a slight conductivity enhancement was observable in the ZrO_2 addition to the mechanical mixing NZS, in contrast to the significant

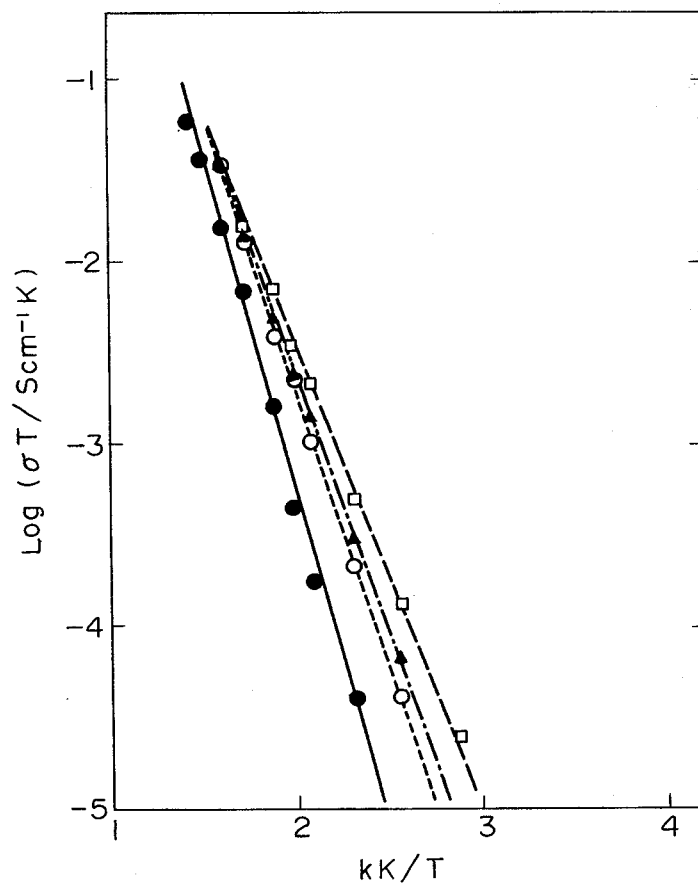Fig. 3-21 Temperature dependence of ionic conductivity of mechanical-mixing NZS: (—●—) NZS without dispersant; (—▲—) NZS+40mol%Al_2O_3; (—○—) NZS+40mol%ZrO_2; (—□—) NZS+40mol%SO_4^{2-}/ZrO_2.
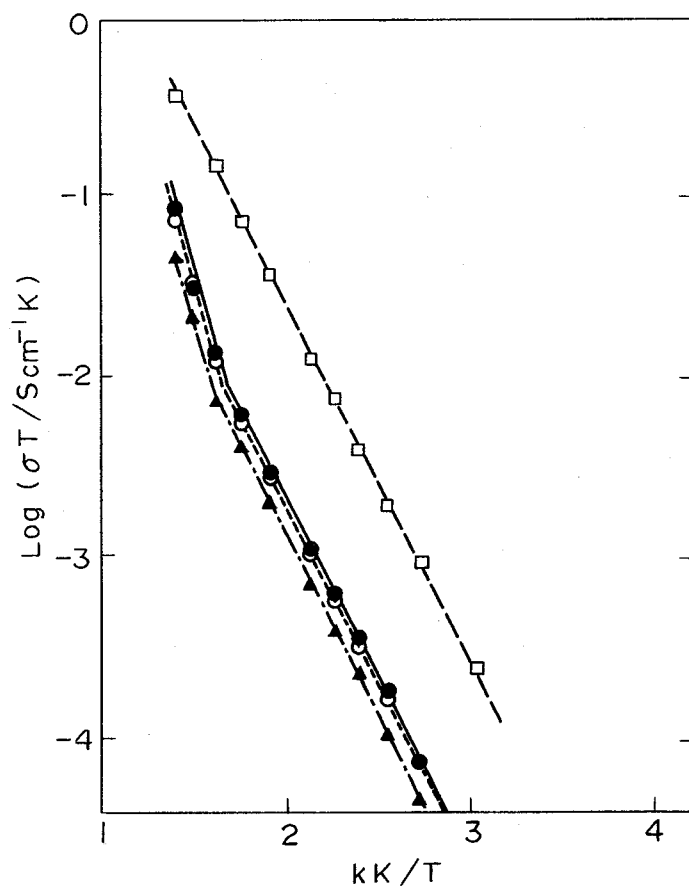
Fig. 3-22 Temperature dependence of ionic conductivity of sol-gel NZS: (—●—) NZS without dispersant; (—▲—) NZS+40mol%Al$_2$O$_3$; (--O--) NZS+40mol%ZrO$_2$; (—□--) NZS+40mol%SO$_4{}^{2-}$/ZrO$_2$.

enhancement in the SO_4^{2-}/ZrO_2 addition. These experimental results suggest that the dielectric constant of SO_4^{2-}/ZrO_2 is ineffective for conductivity enhancement.

The solid superacid SO_4^{2-}/ZrO_2 addition into NZS was effective for conductivity enhancement. This fact suggests that the enhancement may be due to an acid-base interaction at the interface between dispersant and NZS particles. This may be supported by the finding of Hino et al.[17]. They have found from the X-ray photo-electronic spectroscopy (XPS) and infrared spectroscopy (IR) observations that SO_4^{2-} groups would be coordinated at the surface of ZrO_2 particles. Further, this effect retains the concept of the space charge layer model for the ionic conductivity enhancement[5].

3.3.2 Dispersion of SbF_5 adsorbed solid superacids

*** Experimental ***

Four kinds of adsorbed solid superacid $SbF_5/(SiO_2-Al_2O_3)$, (hereinafter S/(S-A)), $SbF_5/(SiO_2-TiO_2)$, (S/(S-T)), $SbF_5/(SiO_2-ZrO_2$, (S/(S-Z)), and $SbF_5/(TiO_2-ZrO_2)$, (S/(T-Z)), were prepared after Shibata et al., as follows[18]. Binary oxides with specific mixing ratio of $SiO_2-Al_2O_3$, (S-A), SiO_2-TiO_2, (S-T) and SiO_2-ZrO_2 (S-Z) were synthesized by coprecipitation from a H_2SiO_3 solution and one of the $AlCl_3$, $TiCl_4$, $ZrOCl \cdot 8H_2O$ solutions with each ratio. TiO_2-ZrO_2 (T-Z) was coprecipitated from mixing solutions of $TiCl_4$ and $ZrOCl_2 \cdot 8H_2O$. Each mixture was allowed to stand overnight and calcined at 500°C for 3 hours after drying at 80°C. Non-acidified silica-alumina (S-A) sample was also pre-

pared by sol-gel method to compare the effect of preparation. $Al(NO_3)_3 \cdot 9H_2O$, $Si(OC_2H_5)_4$, C_2H_5OH and HCl were refluxed at 80°C for 3 hours. The mixture was left for about 2 weeks to become gel, dried at 150°C, and calcined at 500°C for 3 hours. These four kinds of binary oxides were confirmed to be amorphous by X-ray diffraction (XRD). SbF_5 was adsorbed on these binary oxides at 0°C by ten minutes repeating adsorption/desorption for four times.

Specific surface area and the amount of acidic site were measured for the binary oxides, S-A, S-T, S-Z and T-Z by BET method using N_2 gas and NH_3 chemical adsorption, respectively. Particle size and its distribution were measured by transmittance electron microscopy (TEM) photograph and a sedimentation method, respectively. Acid strength of each compound was examined by the method represented in 3.3.1.

*** Result ***

Estimation of acid strength and the amount of acidic site at the surface of superacid particle

In the previous section 3.3.1, it was found that the acidic property of dispersant particles may contribute to the enhancement of the interfacial conductivity. Before going into the quantitative details, the dependences of the enhancement on acid strength (pK_a) and on the contacting interfacial area should be studied. Unfortunately, pK_a is not an adjustable variable when SO_4^{2-}/ZrO_2 was used as the superacid dispersant. On the other

hand, Shibata et al. have reported that the pK_a of SbF_5 adsorbed oxide particles (solid superacid) depends on the oxide matrix[18]. This is the reason why this series was taken up.

Table 3-3 lists the pK_a at room temperature determined by a colour change method using Hammett indicators. These values agree with those of Shibata et al.[18] except S/(S-A). The pK_a of this superacid tends to be greatly affected by the sample preparation procedures. Contrary to the expectation, S/(S-A) prepared by the sol-gel method showed the same pK_a value of <-16.04 as that of S/(S-A) prepared by coprecipitation. It is not clear why such a high value can be obtained. The degree of pK_a reduction by a heat treatment was measured because the solid superacid particles dispersed into the ionic conductor would be heated up during conductivity measurements and the sintering of the composite pellet. After the heat treatment of 1000^OC, pK_a of S/(S-A) remained the same as the initial value, whereas the pK_a of S/(S-T), S/(S-Z) and S/(T-Z) changed down to -12.44, -13.16 and -12.44, respectively.

The contact area between the particles of ionic conductor and solid superacid should also affect the conductivity enhancement since a large number of vacant sites for mobile ions would be created at the interfacial regions. Supposing that the acidic sites at the surface of superacid particles induced vacancies at the ionic conductor surface, the amount of chemisorbed NH_3 (ml/g) was measured. The results are listed in Table 3-4. These were converted to the NH_3 molecules per specific surface area under the condition that the contact interfacial area depends on the surface area of superacid particles. Because the particle size

Table 3-3 Acidic properties of SbF$_5$ adsorbed solid superacids

	S/(S-A)	S/(S-T)	S/(S-Z)	S/(T-Z)
acid strength (pK$_a$)	<-16.04	-13.16	-14.52	-13.16
acid strength after 1000°C heat treatment	<-16.04	-12.44	-13.16	-12.44

Table 3-4 BET surface area and adsorbed NH$_3$ on binary oxides

	S/(S-A)	S/(S-T)	S/(S-Z)	S/(T-Z)
BET surface area (m^2/g)	376	359	308	215
adsorbed NH$_3$ (ml/g)	27	23	17	19
adsorbed NH$_3$(/nm^2)	1.9	1.7	1.5	2.4

of these binary oxides prepared by coprecipitation are almost the same, ~1μm, effective concentration of acidic sites should be proportional to NH_3 molecules adsorbed per specific surface area.

Figure 3-23 shows a schematic mechanism for how the acid strength should be enhanced[19,20]. Accordingly, an acidic site would still remain after SbF_5 saturated adsorption, because SbF_5 molecules should create a chemical bond with the basic site of the oxide surface. Moreover, the number of affected site should be proportional to the number of adsorbed SbF_5 molecules. Therefore, the total amount of Na^+ ion vacancies at the interface region in the ionic conductor can be estimated by the amount of adsorbed NH_3 molecules per unit surface area of solid superacid particles.

Effect of acidity of the dispersants

Figure 3-24 shows Arrhenius type plots of the ionic conductivity of NZS with a 40 mol% dispersion of S/(S-A), S/(S-Z) and S/(T-Z), where maximum enhancement of about two orders of magnitude at 100^OC was observed in the NZS - S/(S-A) composite. This enhancement is compared to that of SO_4^{2-}/ZrO_2. The activation energy decreased with the increase of the conductivity.

Figure 3-25 shows plots of conductivity versus acid strength and the concentration of acidic sites to determine the dominant effect in the enhancement. A linear correlation between log σ and pK_a was obtained, suggesting that acid strength may induce a high vacancy concentration at the interfacial region of the ionic conductor particles. On the other hand, the concentration of
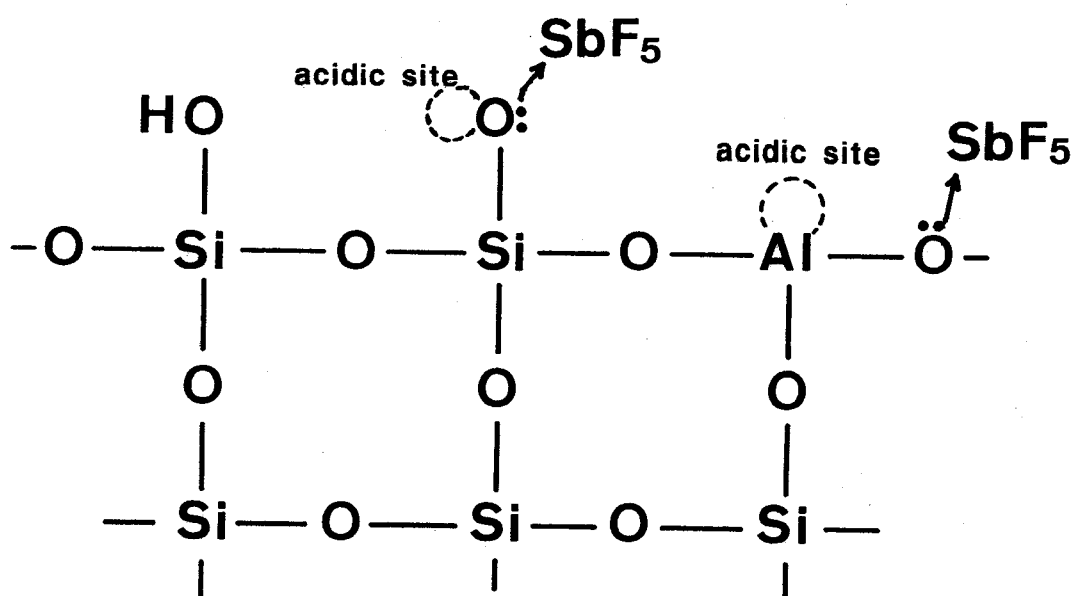
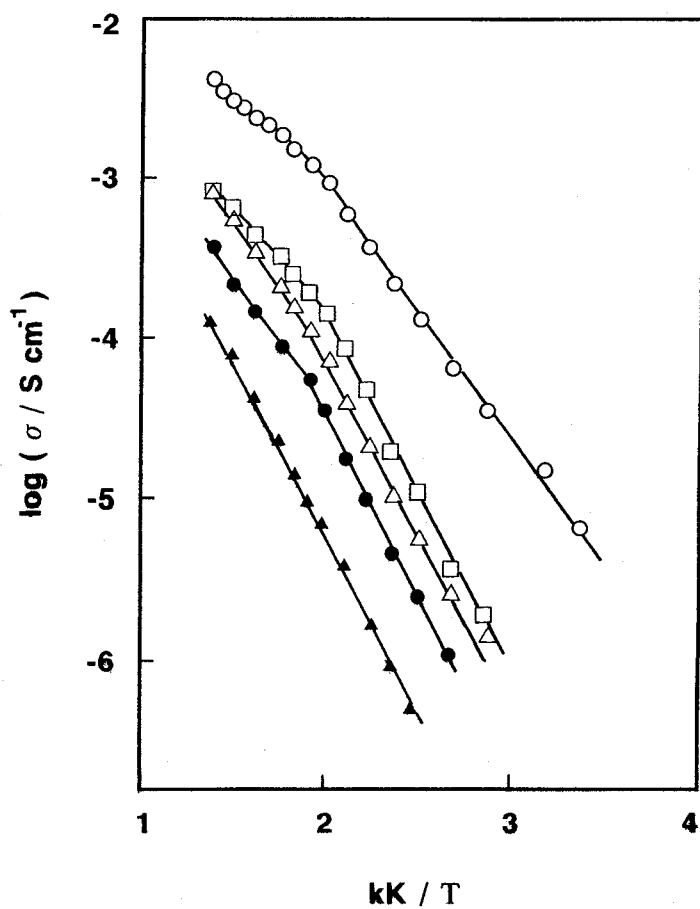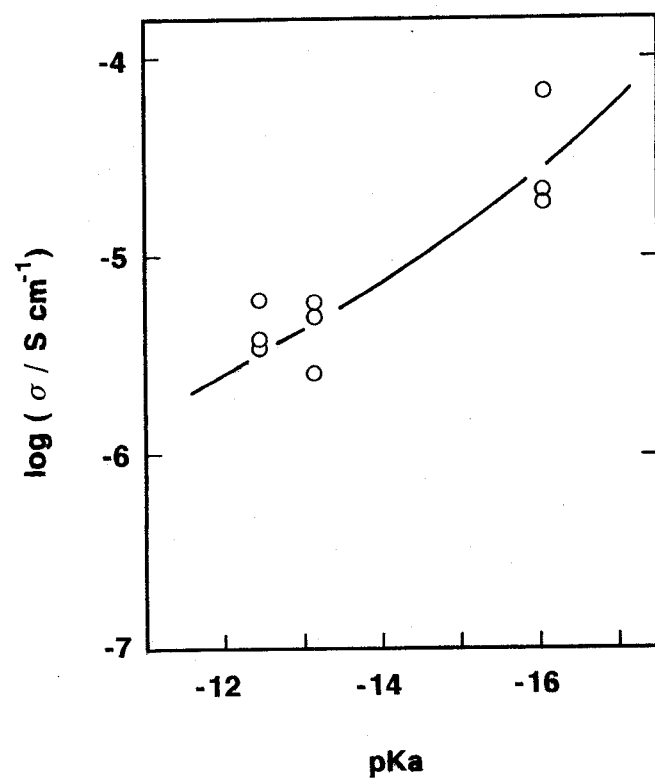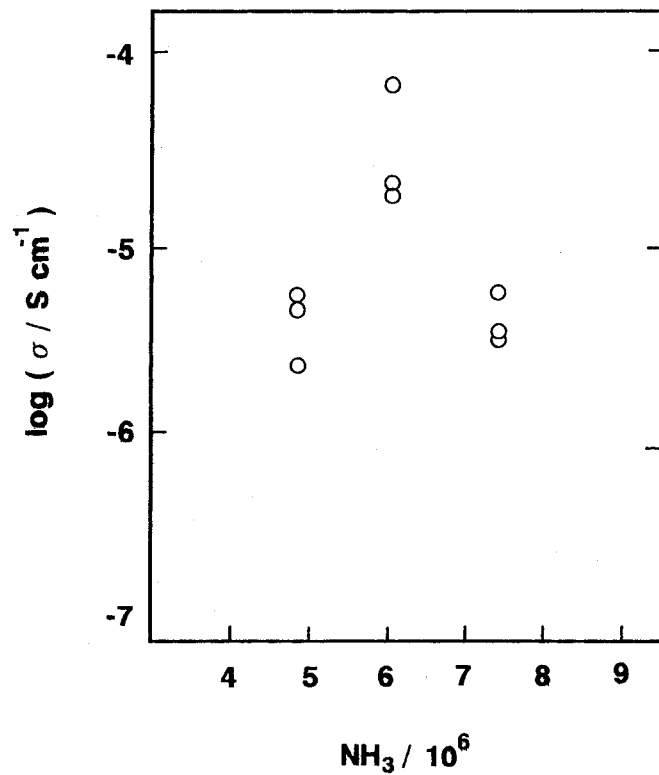Fig. 3-23 Schematic mechanism to enhancing acid strength by SbF$_5$ adsorption.

Fig. 3-24   Temperature dependence of ionic conductivity of NZS (●) and NZS composite with S/(S-A) (○), S/(S-Z) (△), S/(T-Z) (□) and S/(S-T) (▲).

(a)　　　　　　　　　　　　　　　　　　(b)

Fig. 3-25　Conductivity of NZS dispersed with solid superacid as a function of (a) acid strength and (b) amount of acidic site of dispersant.

acidic sites does not correlate with the conductivity enhancement, as shown in fig. 3-25(b).

In the case of the S/(S-T) dispersion, a conductivity decrease and the activation energy increase (fig. 3-24) were observed with increasing dispersant content. Powder XRD pattern of the $1000^{O}C$ sintered composite pellets showed peaks from some unidentified phase. It could be assumed that the creation of a insulating second phase thin layer at the interface would lower the conductivity.

Dominant factor in the interfacial conductivity

In order to discuss the ionic conduction mechanism, the author tried to estilate the mobile ion concentration (c_i) and hopping rate (ω_p) of ions from the frequency dependence of ac conductivity after Almond et al.[21].

Figure 3-26 shows c_i and ω_p as a function of dispersed molar concentration of S/(S-A). The carrier concentration, c_i, almost remained at the value of NZS without dispersant with increasing x, whereas the hopping rate, ω_p, increased about two orders of magnitude. In a space charge model, the vacancies may be concentrated at the interfacial region from the neighbouring bulk region, being induced by a dispersant/ionic conductor intergrain atomic interaction. Consequently, ω_p could be enhanced by the vacancies created at the interfacial regions. However, c_i should be essentially constant since it is represented by the relative ratio of mobile ions to available ions in the conductor particle. This is consistent with the experimental results. The
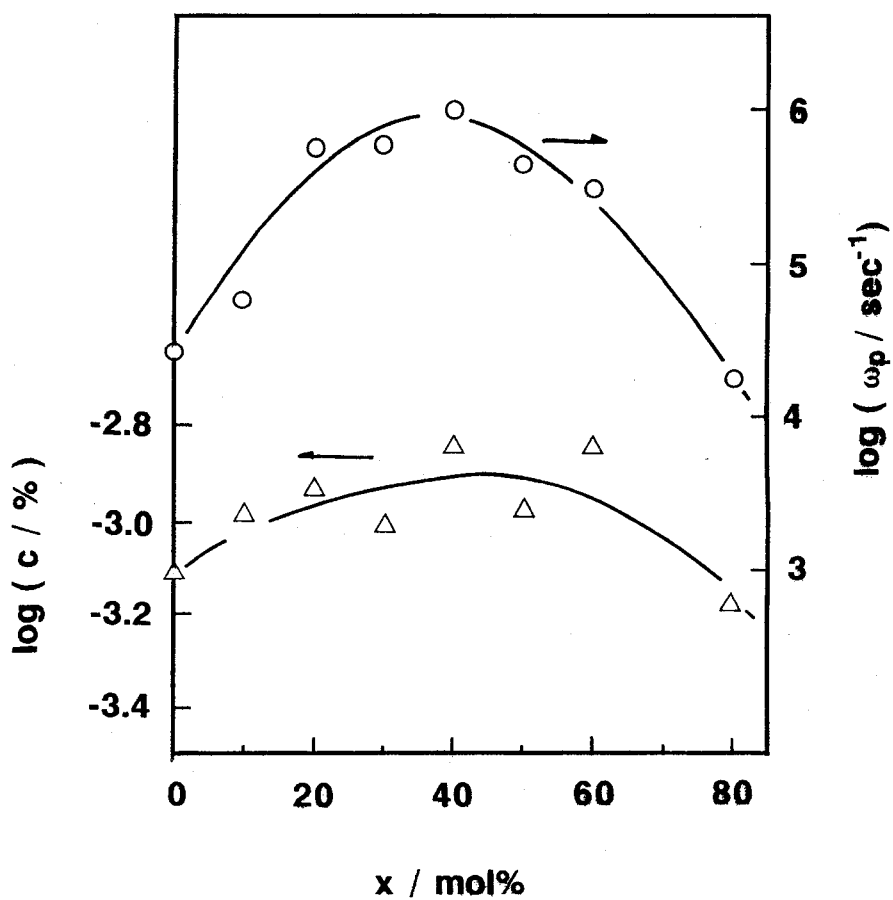
Fig. 3-26 Mobile ion concentration (c_i) and hopping rate (ω_p) of NZS dispersed with S/(S-A) as a function of molar concentration of S/(S-A).

hopping rate, ω_p, would increase because the mean distance between vacancies would be reduced as a result of the increase of vacancy concentration at the interfacial regions.

Figue 3-27 shows the x dependence of c_i and ω_p in the case of S/(S-T) dispersion. An ω_p decrease with increasing x, which was mainly responsible for the observed conductivity decrease, was demonstrated, whereas c_i remained ~0.1% for the whole x range. This is consistent with the model of insulating thin layer formation at the interface region, which was suggested previously by XRD analysis.

Considerable experimental and theoretical studies suggesting that a high conductive layer formed along the ionic conductor/insulator interface is the result of enhanced carrier concentration in the space charge layer[4,5]. However, these experimental results show that the interfacial conductivity enhancement is mainly due to the increase of ω_p, and that c_i is rather unaffected by the superacid particle dispersion.
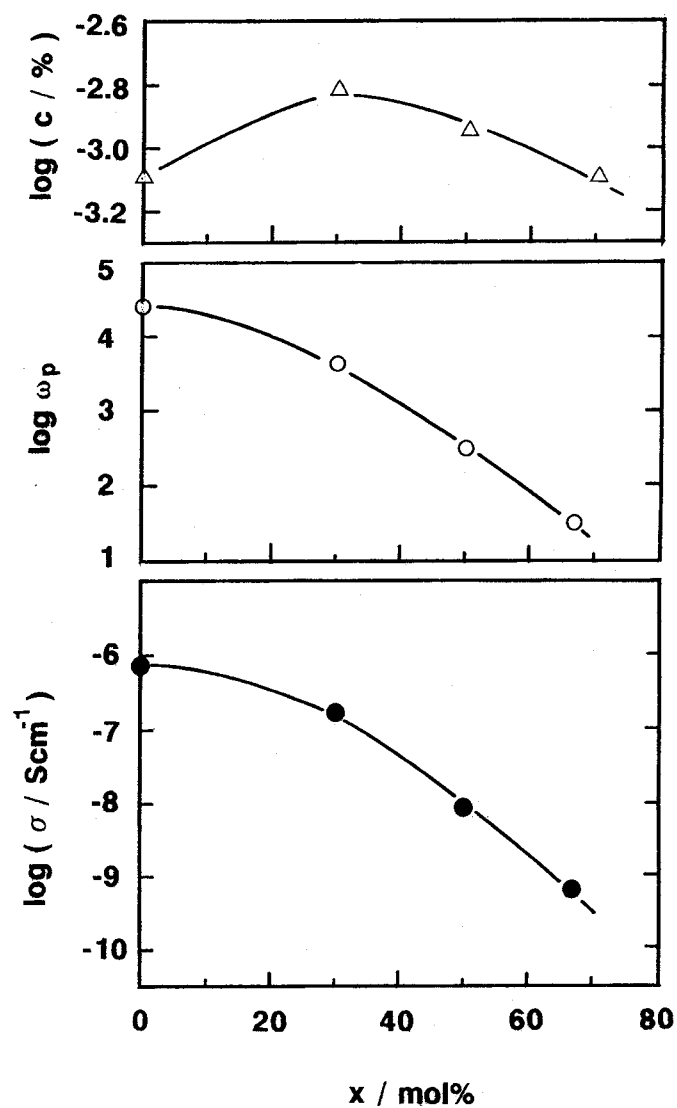
Fig. 3-27 Mobile ion concentration (c_i), hopping rate (ω_p) and electronic conductivity (σ) of NZS dispersed with S/(S-T) as a function of molar concentration of S/(S-T).

References

[1] J. B. Goodenough, Solid State Microbatteries, ed. by J. R. Akridge and M. Balkanski (Plenum Press, New York, 1990) p157.

[2] K. L. Kliewer, J. Phys. Chem. Solids, 27, 705 (1966).

[3] T. Jow and J. B. Wagner, Jr., J. Electrochem. Soc., 126, 1963 (1979).

[4] J. B. Wagner, Jr., Mat. Res. Bull., 15, 1691 (1980).

[5] J. Mayer, J. Phys. Chem. Solid, 46, 309 (1985).

[6] N. J. Dudney, J. Am. Ceram. Soc., 68, 538 (1985).

[7] J. B. Phipps, D. L. Johnson and D. H. Whitmore, Solid State Ionics, 5, 393 (1981).

[8] J. B. Phipps and D. H. Whitmore, Solid State Ionics, 9/10, 123 (1983).

[9] O Nakamura and J. B. Goodenough, Solid State Ionics, 7, 119 (1982).

[10] N. J. Dudney, Solid State Ionics, 28-30, 1065 (1988).

[11] K. Shahi and J. B. Wagner, Jr., J. Electrochem. Soc., 128, 6 (1981).

[12] A. Schiraldi, Z. Phys. Chem. N. F., 97, 285 (1975).

[13] J. Grins and A. R. West, J. Solid State Chem., 65, 265 (1986).

[14] T. Yamamoto, S. Kikkawa and M. Koizumi, Phys. Status Solidi (a) 91, K67 (1985).

[15] M. Hino, S. Kobayashi, K. Arata, J. Am. Chem. Soc., 101, 6439 (1987).

[16] S. Fujitsu, M. Miyayama, K. Koumoto, H. Yanagida and T. Kanazawa, J. Mat. Sci., 20, 2103 (1985).

[17] M. Hino, K. Arata and K. Yabe, Shokubai (Catalysis) <u>22</u>, 232 (1980).

[18] K. Shibata, T. Kiyoura, J. Kitagawa, T. Sumiyoshi and K. Tanabe, Bull. Chem. Soc. Jpn., <u>46</u>, 2985 (1973).

[19] M. W. Tamele, Disc. Faraday Soc., <u>8</u>, 270 (1960).

[20] K. Tabe and R. Noi, "Superacid and superbase" (Kodansya, Japan, 1981) p13.

[21] D. P. Almond, G. K. Duncan and A. R. West, Solid State Ionics, <u>8</u>, 159 (1983).

[22] D. L. Olgaard and B. Evans, J. Am. Ceram. Soc., <u>69</u>, C272 (1986).

4. Conductivity enhancement by the formtaiton of non-stoichiometric structure

4.1 Purpose of these approaches

Substitution of one host ion by another ion with different valence introduces some defects such as interstitial ions and vacancies. This change in the lattice structure leads to the displacement of neighbouring ions and the change in bonding nature with surrounding ions. These, more or less, contribute to the conductivity change, i.e., enhancement or reduction, in ionic conductors because these affect the mobile ion content and the mobility which are the principal factors of the conductivity. If the process of the conductivity enhancement by the substitution is realized systematically, the enhancement mechanism at the interface between heterogeneous particles could be estimated based on the concept common to any kinds of the conductivity enhancement. This discussion would be extended in chapter 5, and the author will introduce the new concept, 'defect core structure' to explain the conductivity enhancement mechanism.

This chapter will be concentrated on the experimental investigation of the relationship between the enhanced conductivity and the features of dopants or consequent structural change when the non-stoichiometric conductors are formed by doping technique.

4.2 $Li_{1+x}M_xM'_{2-x}(PO_4)_3$ (M: Sc^{3+}, Y^{3+}, M': Ti^{4+}, Zr^{4+}) type ionic conductors

Lithium ion conductors are promising materials for the development of high-energy density batteries. The properties of high ionic conductivity, high decomposition potential and less reactivity with water and carbon dioxide should be satisfied when they are applied to solid electrolytes. Not so many Li^+ ion conductors with high conductivity have been developed compared with high Na^+ ion conductors, because Li^+ ion has a high polarizing power.

$LiZr_2(PO_4)_3$ (LZP) system, which is one of the lithium analogues of NASICON end member, $NaZr_2(PO_4)_3$, is generally accepted to show a low ionic conductivity because Li^+ ion is too small in size to migrate freely in the three-dimensional network[1], and the sinterbility is fairly low in ceramics.

The $LiTi_2(PO_4)_3$ (LTP) system shows higher conductivity than that of LZP since the six membered oxygen bottleneck which composed of alternative PO_4 and TiO_6 structures for Li^+ ion migration is more suitable in size. Aono et al. have tried to prepared $Li_{1+x}M_xTi_{2-x}(PO_4)_3$ (M-LTP) systems with different M^{3+} ions[2]. The conductivities of almost all M-LTP systems have increased and the porosities of sintered pellets have decreased compared with those of the original LTP. In addition, the maximum conductivity relevant to the M^{3+}ion content has been found to be independent of the ionic radii of M^{3+} ions. This suggests the conductivity enhancement is mainly attributed to the grain boundary conductivity which depends on the density and segregated ions

in the grain boundary region of sintered pellet.

In this section, conductivity changes of $Li_{1+x}M_xTi_{2-x}(PO_4)_3$ (M: Sc^{3+}, Y^{3+}) with x are discussed on the basis of the mobile Li^+ ion concentration (c_i) and its hopping rate (ω_p) which are two factors contributing to the observed conductivity. And these results are compared with those of LZP in order to estimate the effect of tetravalent ion size for the conductivity enhancement.

*** Experimental ***

The compounds were prepared by a conventional solid state reaction using starting materials, Li_2CO_3, M_2O_3 (M; Sc^{3+} or Y^{3+}), TiO_2, $ZrO(NO_3)_2 \cdot 2H_2O$ and $NH_4H_2PO_4$. The stoichiometric mixtures were sintered at $1000^O C$ for 24 hours, and the products were identified by their XRD patterns. Lattice constants were refined with the least-squares method using observed peaks ($\sin\theta/\lambda$ < 0.562) based on the structural symmetry $R\bar{3}c$.
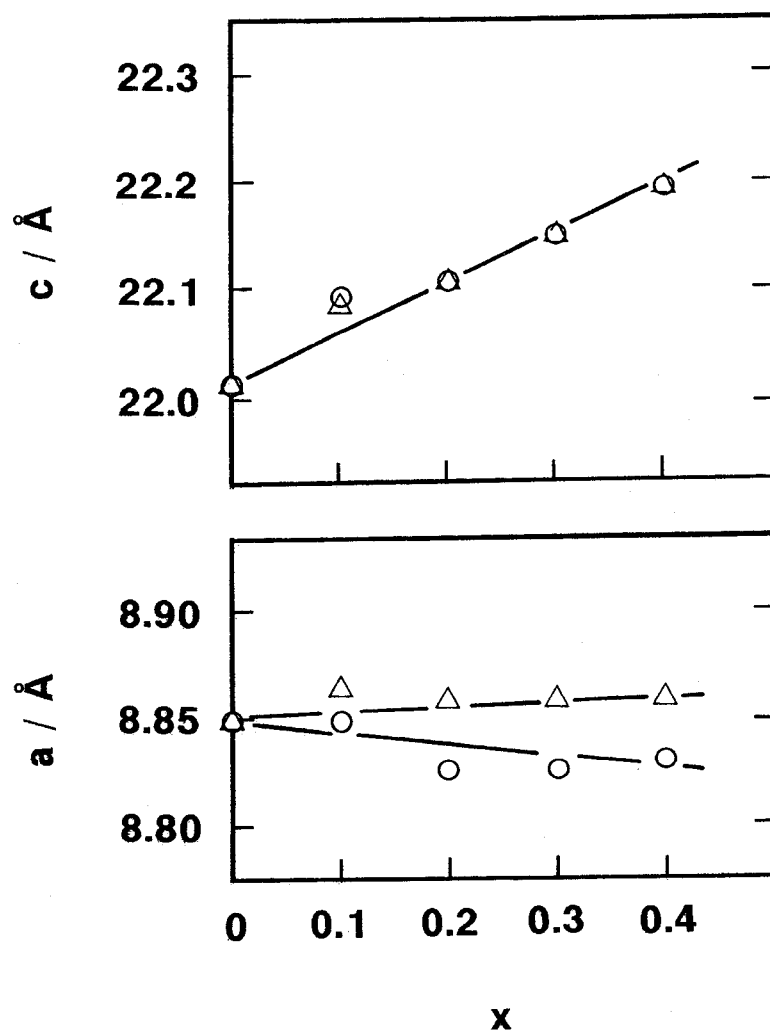

*** Results ***

Plots of lattice parameter versus doped ion content are shown in fig. 4-1 to determine the solubility limit for nominal Sc- and Y- substituted LTP and LZP systems. In the Sc-LTP system, both crystallographic a and c parameters increased with x up to x=0.4. This is consistent with that Sc^{3+} ion (ionic radius; 0.73 A) is slightly larger than Ti^{4+} ion (0.605 A). Further increase of x showed no more change both in the a and c axis lengths and the broadening of the XRD peaks as well as the increase of the second phase ($ScPO_4$) peak intensity. On the contrary, a and c parameters of Y-LTP system kept constant, inde-
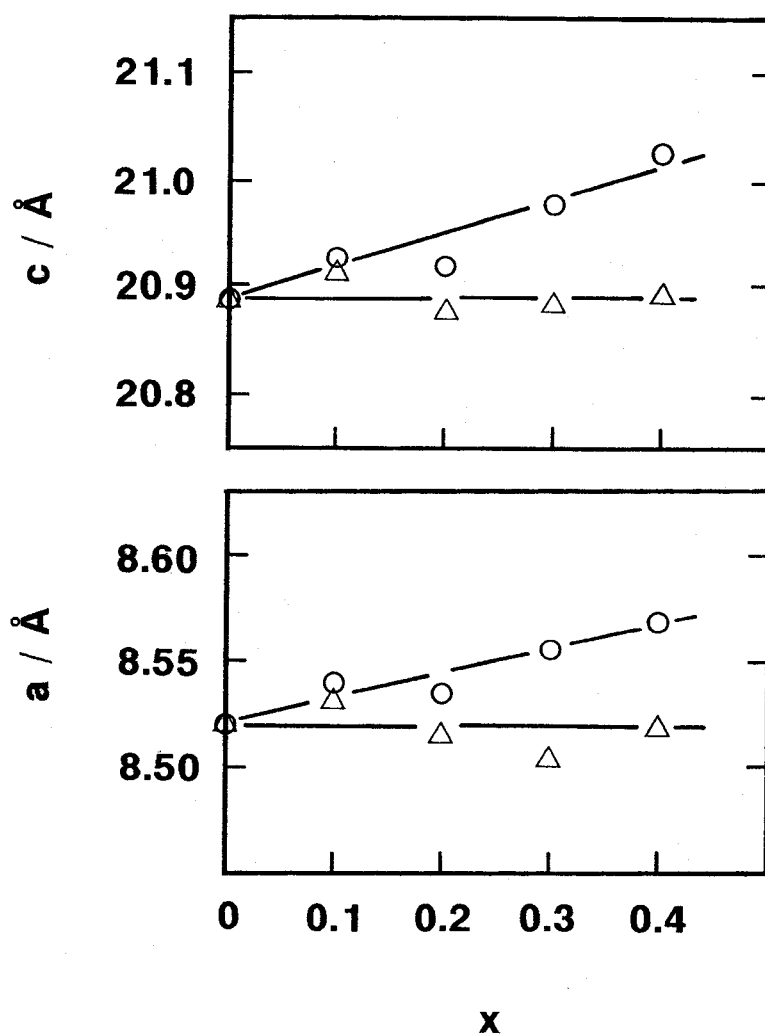
Fig. 4-1　Crystal lattice parameters of (a) $Li_{1+x}M_xTi_{2-x}(PO_4)_3$ and (b) $Li_{1+x}M_xZr_{2-x}(PO_4)_3$ (M: Sc^{3+} (O), Y^{3+} ($\triangle$)) as a function of x.

(b)

pendent of x and second phase (YPO$_4$) peak intensities increased with the increase of x, suggesting that the Ti^{4+} ion would not be replaced by Y^{3+} ion (0.89 A). These results agree with those of Aono et al.[2].

The XRD patterns of LZP systems also showed the two phase mixture, even in x=0, comprizing of R$\bar{3}$c assigned NASICON phase and the distorted R$\bar{3}$c second phase[1]. The peak intensities of the second phase increased with increasing x in addition to the peak broadening. Figure 4-1(b) shows the compositional c dependence of crystallographic a- and c-axis lengths of LZP systems for only the R$\bar{3}$c phase, ignoring second phase peaks.

The ionic conductivity variation with x are shown in fig. 4-2 and 4-3 for nominal Sc- and Y- substituted LTP and LZP systems, respectively. In the LTP system, the maximum conductivity was observed for Sc-LTP ($\sigma_{27^{o}C}$ = 4.0 x 10^{-5} Scm^{-1}) and Y-LTP ($\sigma_{27^{o}C}$ = 3.2 x 10^{-1} Scm^{-1}) systems at around x=0.3. These results fairly agree with those of Aono et al.[2]. Obtained capacitance data (~250 pFcm^{-1}) assuming parallel RC equivalent circuit for semicircles in Cole-Cole plots indicate that the observed conductivity was mainly composed of the grain boundary conductivity.

In the LZP systems, the conductivity decrease with x was observed in both Sc-LZP and Y-LZP sintered pellets.

In order to discuss the ionic conduction mechanism from the above conductivity dependence on x in the LTP and LZP systems, the mobile ion concentration (c$_i$) and hopping rate (ω_p) of ions were estimated from the frequency dependence of ac conductivity (fig. 4-2, 4-3) after Almond et al.[3,4]. In the Sc-LTP system,
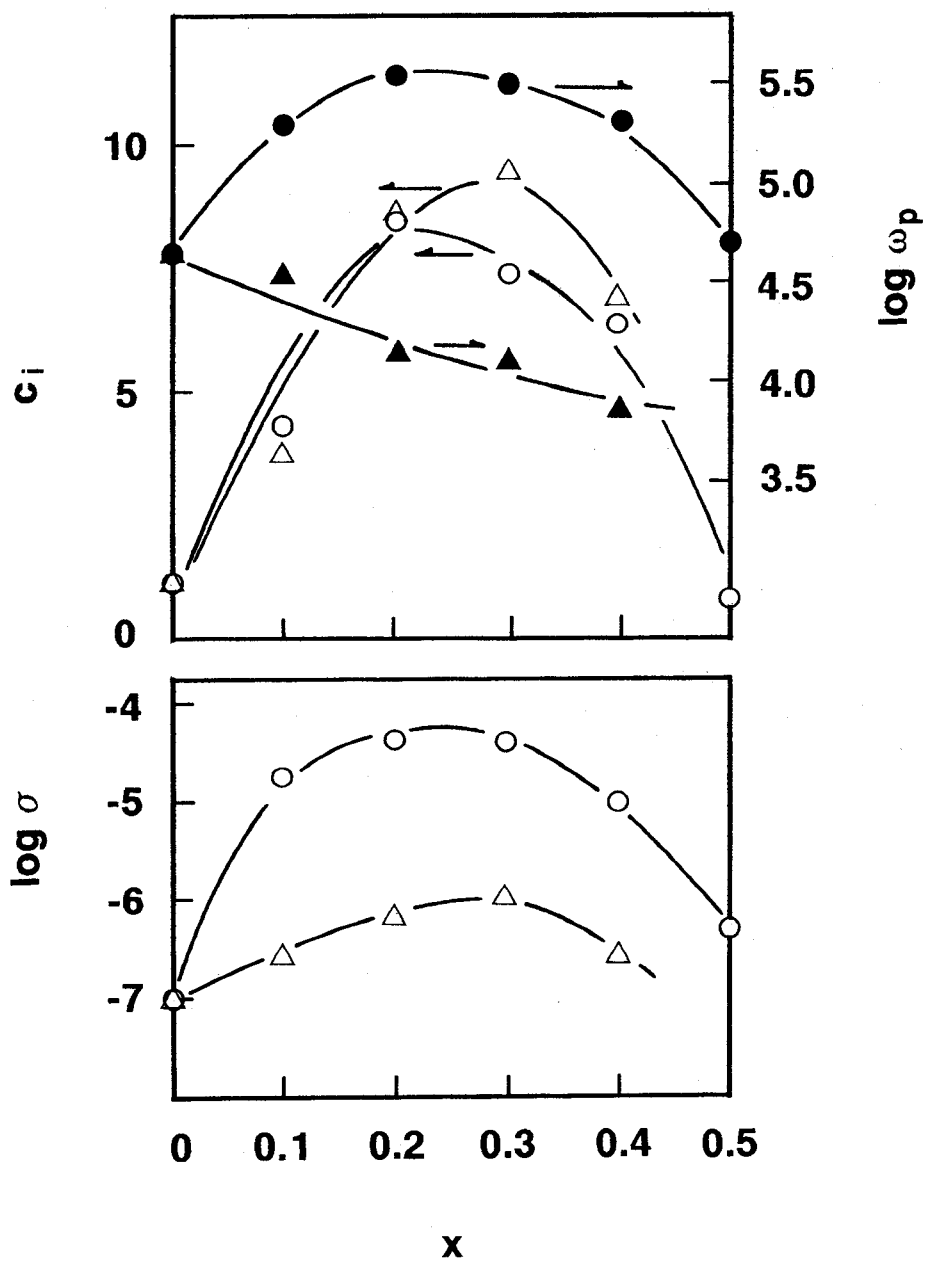
Fig. 4-2 Electrical conductivity (σ), mobile ion concentration (c_i) and hopping rate (ω_p) of $Li_{1+x}M_xTi_{2-x}(PO_4)_3$ (M: Sc^{3+} (O,●), Y^{3+} (△,▲)) at 27^OC as a function of x.

Fig. 4-3 Electrical conductivity (σ), mobile ion concentration (c_i) and hopping rate (ω_p) of $Li_{1+x}M_xZr_{2-x}(PO_4)_3$ (M: Sc^{3+} (O,●), Y^{3+} (△,▲)) at $27^{\circ}C$ as a function of x.

both c_i and ω_p increased with x in the region of 0<x<0.3, and then decreased beyond x=0.3, similar to the dependence of the total conductivity. Extra Li^+ ions resulting from Sc^{3+} ion substitution for Si^{4+} ion could occupy the interstitial sites. This can promote the increase of c_i and ω_p. In this case, the porosity was controlled in almost the same for doped or undoped pellet because the conductivity and the activation energy strongly depend on the porosity of sintered LTP pellets[5,6].

On the other hand, the x dependence of c_i in the Y-LTP system was similar to that of Sc-LTP, but ω_p decreased with x. Furthermore, the c_i showed the temperature dependence in contrast to the temeprature independent c_i of Sc-LTP system. As Y-LTP system is essentially two phase mixture composed of $LiTi_2(PO_4)_3$ and the Y containing second phase, the decrease of ω_p with x should be expected because the insulating second phase may block the Li^+ ion migration along and across the grain boundary region. But the increase of c_i compared with that of end member LTP is never expected. My experimental results, therefore, show a possibility that a special thin layer with high Li^+ ion conduction at the interfacial region between grains might be formed which has different mechanism from the intracrystal.

In the zirconium analogue Sc-LZP and Y-LZP systems, both c_i and ω_p decreased with x. This suggests that the effect of the second phase blocking for the Li^+ ion migration along and across the grain boundary region would be greater compared to the conductivity enahancing effect by doped ions.

These results are consistent with that the LZP single phase is difficult to prepare by a conventional solid state reaction

because of the structural instability[1]. This is the definite difference in Li^+-ion conduction from the LTP systems.

In conclusion, the frequency dispersion analyses of LTP and LZP systems show that c_i mainly attributed to the total conductivity. Unexpected increase in c_i in Y-LTP system suggests the possibility that a highly ion conductive layer might be formed at the interface between grains.

4.3 $Na_{1+x}M_xZr_{2-x}(PO_4)_3$ (M: trivalent ion) type ionic conductors

NASICON, $Na_{1+x}Zr_2P_{3-x}Si_xO_{12}$ ($0 \leq x \leq 3$), is well known as a high Na^+ ion conductor with three-dimensional network structure which has rhombohedral space group $R\overline{3}c$ except for the distorted structures at x~ 2.0[7]. There are two types of Na^+ ion sites (Na_1 and Na_2) located in the network which is composed of SiO_4/PO_4 tetrahedra sharing corners with ZrO_6 octahedra and the interstitial spaces. Na^+ ions partially occupying these sites could hop to the neighbouring vacant sites with some activation energy, resulting in the ionic conduction.

The conductivity depends on the value of x which is responsible both for the mobile ion content and the ionic mobility changing with the ratio of PO_4 to SiO_4. As x increases, the mobile Na^+ ion content increases, which is the main reason for the conductivity increase for smaller x value. At x=2, NASICON shows the maximum conductivity. In the range of x>2, the conductivity decreases with x. This reduction would be mainly due to two casues. One is the decrease of mobile ion content because the increase of x leads to the lack of Na^+ vacant sites which are needed for mobile Na^+ ions to migrate. Another is the decrease of ionic mobility by the structural change of SiO_4^{4-} tetrahedra in place of PO_4^{3-} tetrahedra[20]. That is, lower valent ions (Si^{4+}) substituted for P^{5+} ions polarize the surrounding oxygen ions less and the attractive interaction between the oxygen and the mobile Na^+ ion at the bottleneck or at the Na^+ ion site is enhanced. This effect would reduce the ionic mobility.

The change of the mobile ion content and the ionic mobility

could also be inctroduced by the partial substitution of ions which construct the NASICON framework structure by aliovalent ions. In this section, the substituted compounds for Zr^{4+} ions of $NaZr_2P_3O_{12}$ were prepared and the conductivity changes and lattice constants were compared with substituted ionic radii. Part of the Zr^{4+} ions was replaced by trivalent ions in order to increase the Na^+ ion content per chemical formula unit. The change of mobile ion concentration and ion mobility were estimated from the ac conductivity to investigate the ionic conduction mechansims in this system.

4.3.1 $Na_{1.5}M_{0.5}Zr_{1.5}(PO_4)_3$ (M: Al^{3+}, Ga^{3+}, Cr^{3+}, Sc^{3+}, Fe^{3+}, In^{3+}, Yb^{3+}, Y^{3+}) ionic conductors

*** Experimental ***

The starting materials, Na_2CO_3, $ZrO(NO_3)_2 \cdot 2H_2O$, $NH_4H_2PO_4$ and one of Al_2O_3, Ga_2O_3, Cr_2O_3, Sc_2O_3, Fe_2O_3, In_2O_3, Yb_2O_3, Y_2O_3 were mixed mechansically in stoichiometric proportion of $Na_{1.5}M_{0.5}Zr_{1.5}(PO_4)_3$ and sintered at $1000^{\circ}C$ for 10 hours. All sintered materials were identified by XRD patterns $((\sin\theta)/\lambda < 0.562)$ based on the structural results of Hong[7].

*** results ***

Figure 4-4 shows the dependence of lattice parameters of $Na_{1.5}M_{0.5}Zr_{1.5}(PO_4)_3$ (M: Al^{3+}, Ga^{3+}, Cr^{3+}, Sc^{3+}, Fe^{3+}, In^{3+}, Yb^{3+}, Y^{3+}) on the radius of the substituted ion. For the compounds substituted with larger ions in size than Zr^{4+} ions, a and c parameters increased with the substituted ionic radius. This
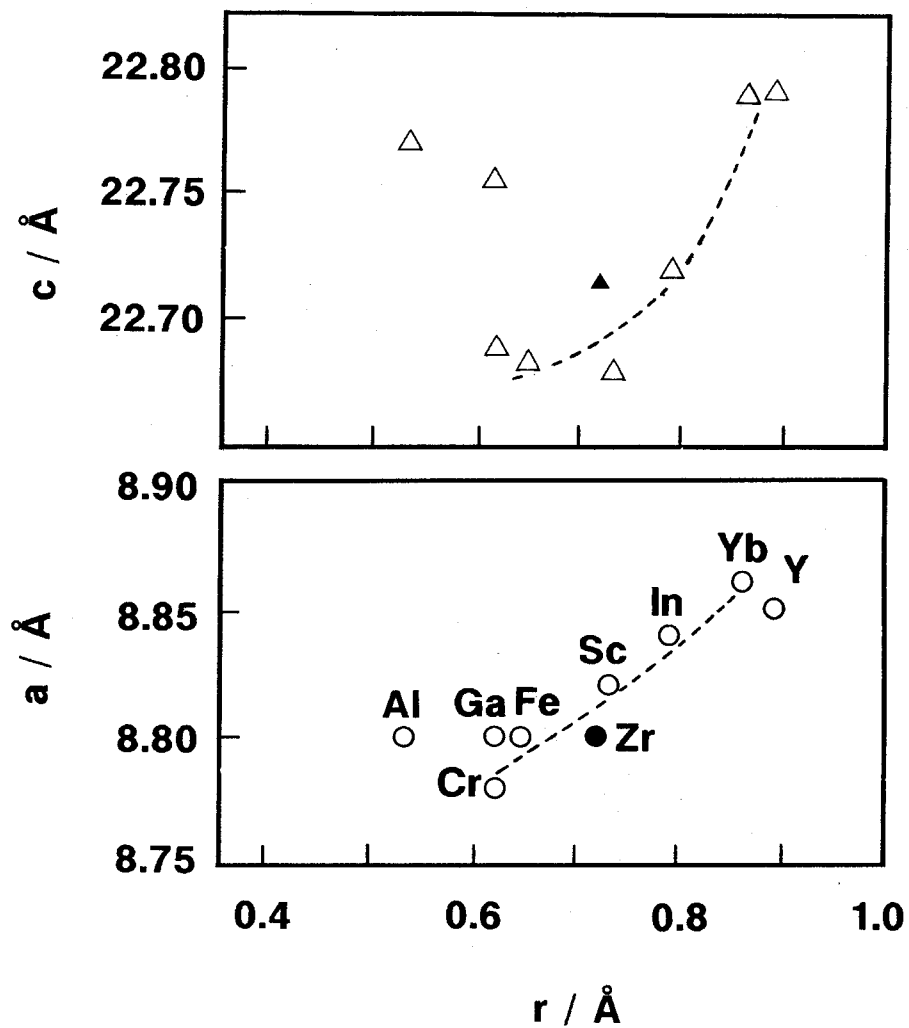
Fig. 4-4 Rhombohedral cell parameters of a and c axes as a function of ionic radius (r) of M in $Na_{1.5}M_{0.5}Zr_{1.5}(PO_4)_3$ (M: Al^{3+}, Ga^{3+}, Sc^{3+}, Cr^{3+}, Fe^{3+}, In^{3+}, Yb^{3+}, Y^{3+}).

change would depend on the size of MO_6 octahedron substituted for ZrO_6 octahedron in the structure. The extra Na^+ ion content (X=0.5) would scarcely affect the expansion of the lattice parameters because $NaZr_2(PO_4)_3$ (NZP) has the original vacant sites appropriate for extra Na^+ ion occupation. On the other hand, for the smaller ion (Al^{3+}, Ga^{3+}, Cr^{3+} and Fe^{3+}) substitution, changes of lattice parameters did not always depend on the ionic radii. In the case of Cr^{3+} and Fe^{3+} ion substitutions, a and c parameters decreased compared with NZP, which could be realized from the smaller size of CrO_6 and FeO_6 octahedra than that of ZrO_6. Ga^{3+} and Al^{3+} ion substitutions, however, showed almost the same value of a parameters and larger value of c parameters compared with those of NZP. Figure 4-5 shows the lattice parameters variation versus composition x of nominal compounds of $Na_{1+x}(Al,Ga)_xZr_{2-x}(PO_4)_3$. There are no obvious change in lattice parameters with increasing x both in Al^{3+} and Ga^{3+} ion substitution. These are different from the case of Cr^{3+} ion substitution reported by Delmas et al. where the lattice parameters decreased with the increase of the content of dopant Cr^{3+} ion[21]. It is shown from these results that the Al^{3+} and Ga^{3+} ions do not substitute for Zr^{4+} ions even in smaller x in NZP.

The substitutional feature would be attributed to the electronic structure of dopants. The dopant ions could be divided into two groups, i.e., ions of main group elements (Al^{3+} and Ga^{3+}) and transition group elements (Cr^{3+}, Sc^{3+}, Fe^{3+}, In^{3+}, Yb^{3+}, Y^{3+}). Coordination properties with oxygen ions are different between them because the orbital symmetries of valence electrons are different. Zr^{4+} ions in NASICON structure coordinate
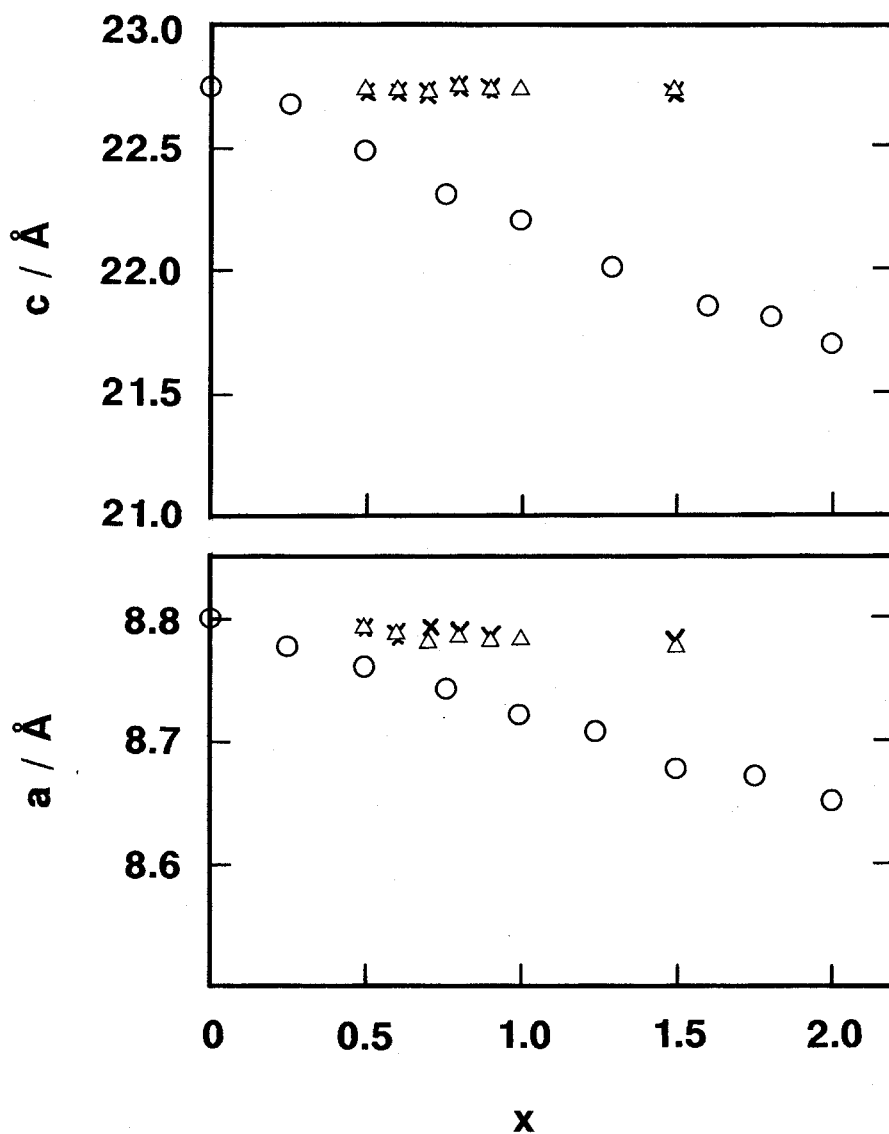
Fig. 4-5 Variation of rhombohedral cell parameters versus composition x of nominal $Na_{1+x}M_xZr_{2-x}(PO_4)_3$ (M: Al^{3+} (X), Ga^{3+} ($\triangle$)) and $Na_{1+x}Cr_xZr_{2-x}(PO_4)_3$ (O) reploted from the result of Delmas et al.[21].

octahedrally with six O^{2-} ions; therefore, it would be natural for ions of the transition group element to substitute for the Zr^{4+} ions because they have the electrons of d-orbital with the octahedral coordination property.

In the case of lithium orthosilicate type ionic conductors, $Li_{4.2}M_{0.2}Si_{0.8}O_4$ (M: B^{3+}, Al^{3+}, Ga^{3+}, Cr^{3+}, Sc^{3+}, Fe^{3+}, In^{3+}, Yb^{3+}, Y^{3+}), higher conductivities were observed in the substitutions with M ions of the main group element rather than the compounds with the M ions of the transition group element. Si^{4+} ions prefer to coordinate tetrahedrally into many kinds of crystal structures. The ion of main group element, which has the spherical orbital of valence electrons, would be appropriate for the substitution for Si^{4+} ions rather than the ion of transition group elements. Detailed discussion of lithium silicate type conductors is explained in section 4.4

Figure 4-6 shows the dependence of electrical conductivities on substituted ionic radius at $100^{O}C$ and $300^{O}C$. The larger the substituted ionic radius, the higher the conducvitity is observed at $100^{O}C$. The dependence of the conductivity is similar to that of crystal lattice parameters in fig. 4-4. This suggests that the increase of lattice parameters would contribute to the expansion of the width of the bottleneck for the ion migration resulting in the higher conductivity. However, the conductivity of Ga^{3+} doped conductor is lower than that of Cr^{3+} doped conductor about one order of magnitude although the ionic radii of Cr^{3+} and Ga^{3+} ions are the same. This is because the Ga^{3+} ions do not substitute for Zr^{4+} ions in the lattice structure and do not contribute to the increase of mobile ion content and/or the
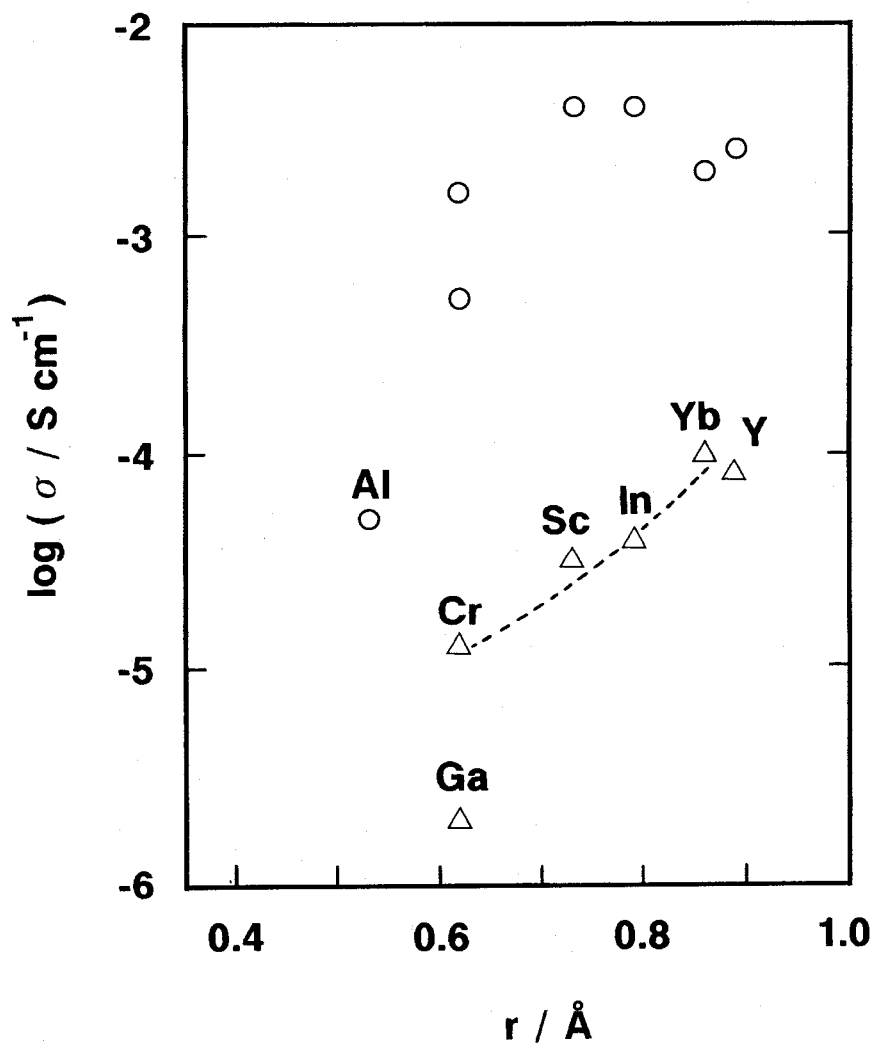
Fig. 4-6 Electrical conductivity of $Na_{1.5}M_{0.5}Zr_{1.5}(PO_4)_3$ as a function of ionic radius (r) of M at $100^{O}C$ and $300^{O}C$.

expansion of bottleneck on the NZP structure. The dependence of conductivities on substituted ionic radius at 300°C was similar to that at 100°C except in the cases of Yb^{3+} and Y^{3+} ion substitutions which show lower conductivities than In^{3+} or Sc^{3+} substituted compound. This reverse comes from the fact that the temperature dependence of conductivity of Yb^{3+} and Y^{3+} ion substituted compounds change in slope at ~180°C. This may correspond to the structural transition by the lattice distortion as a result of larger ion substitutions.

4.3.2 Different effect between the doping of Ga^{3+} and Cr^{3+} ions

Several attempts of trivalent ion substitution for Zr^{4+} ions in NZP almost showed the conductivity enhancement independent of the possibility of the substitution. This is because mobile ion content and/or the ionic mobility increase not only in the bulk (inner crystal) region but also in the grain boundary regions where the impurities tend to be segregated. In this section, a different effect between Ga^{3+} and Cr^{3+} ions doping on the ionic conductivity is demonstrated from the estimation of the mobile ion concentration and mobility of nominal $Na_{1.5}Ga_{0.5}Zr_{1.5}(PO_4)_3$ (Ga-NZP) and $Na_{1.5}Cr_{0.5}Zr_{1.5}(PO_4)_3$ (Cr-NZP) ionic conductors.

The temperature dependence of the electrical conductivity of Ga-NZP and Cr-NZP are shown in fig. 4-7. Apparent activation energies (E_a) are 47 kJ/mol and 43 kJ/mol for Ga-NZP and Cr-NZP, respectively. The capacitances obtained from the impedance data on the basis of RC equivalent circuit are ~100 $pFcm^{-1}$ for both compounds, indicating that the observed conductivities correspond
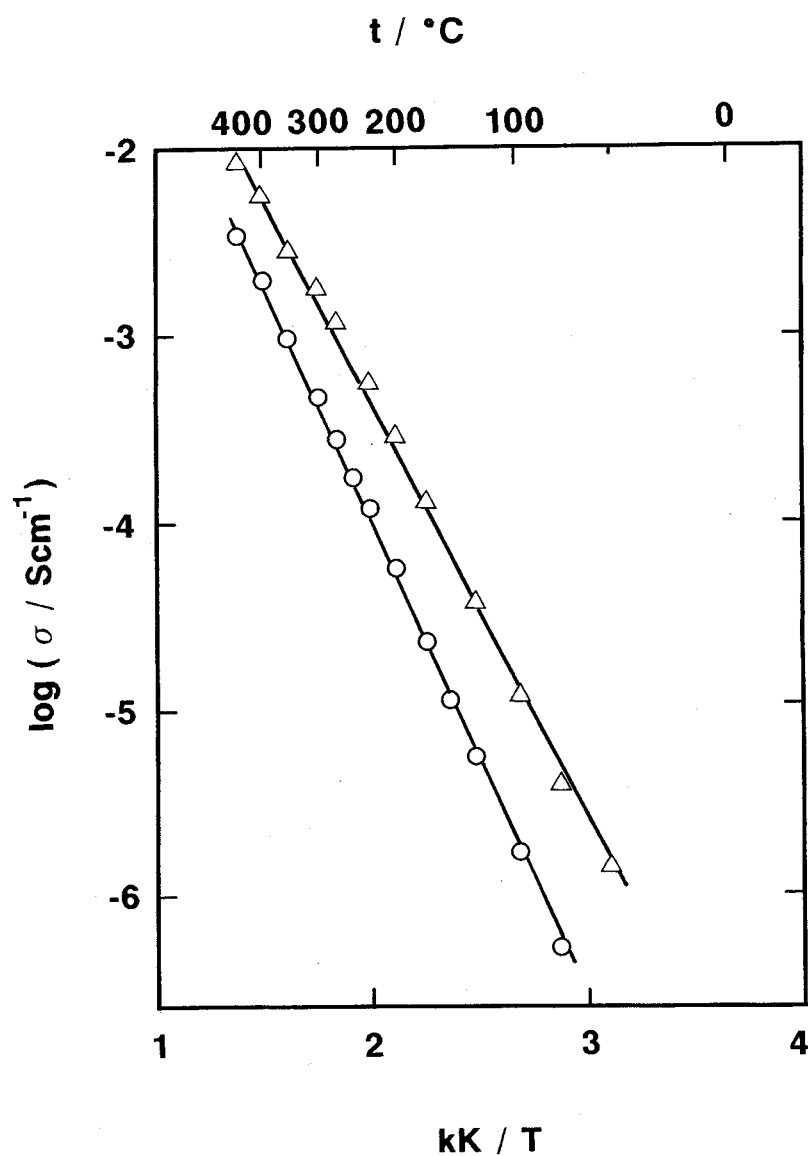
Fig. 4-7 Temperature dependence of electrical conductivity of $Na_{1.5}Ga_{0.5}Zr_{1.5}(PO_4)_3$ (O) and $Na_{1.5}Cr_{0.5}Zr_{1.5}(PO_4)_3$ (△).

to the grain boundary conductivities. When the content of Ga^{3+} ions increased to x~1.0, the conductivity did not show the obvious change. On the other hand, it is reported by Delmas et al. that the conductivities of Cr^{3+} substituted compound increased with x up to x~1.5[21]. It is probable that the extra Ga^{3+} and Na^+ ions (X=0.5) which are introduced in the preparation of Ga-NZP are segregated in the grain boundary between NZP dominant particles. Therefore, the increase of x only affects this grain boundary region which is different from the crystal structure of NZP. On the other hand, substitution of Cr^{3+} ions resulted in a change in the crystal structure which was observed by the change of lattice parameters. It could be assumed from this result that the observed grain boundary conductivity of Cr-NZP reflects the substituted crystal structure.

In order to investigate the conduction properties of Ga-NZP and Cr-NZP in detail, the mobile ion concentration (c_i) and hopping rate (ω_p), which are the two main factors of the conductivity, were estimated from the frequency dispersion analysis of ac conductivity following the procedure of Almond et al.[3,4].

Ac conductivities as a function of frequency at several temperatures for Ga-NZP and Cr-NZP are shown in fig. 4-8. The solid lines were obtained by least-squares fit. The values of $\sigma(0)$ and A used for these fits are shown in fig. 4-9 with the conventional Arrhenius format. At $100^\circ C$, $c_i = 1.5\%$ and $\omega_p = 5 \times 10^5$ /s for Ga-NZP , and $c_i = 5\%$ and $\omega_p = 1.0 \times 10^6$ /s for Cr-NZP. Both c_i and ω_p of Cr-NZP were larger than those of Ga-NZP resulting in higher conductivity. Furthermore, in the case of Cr-NZP, the ratio of the activaiton energies of $\sigma(0)$ and A was
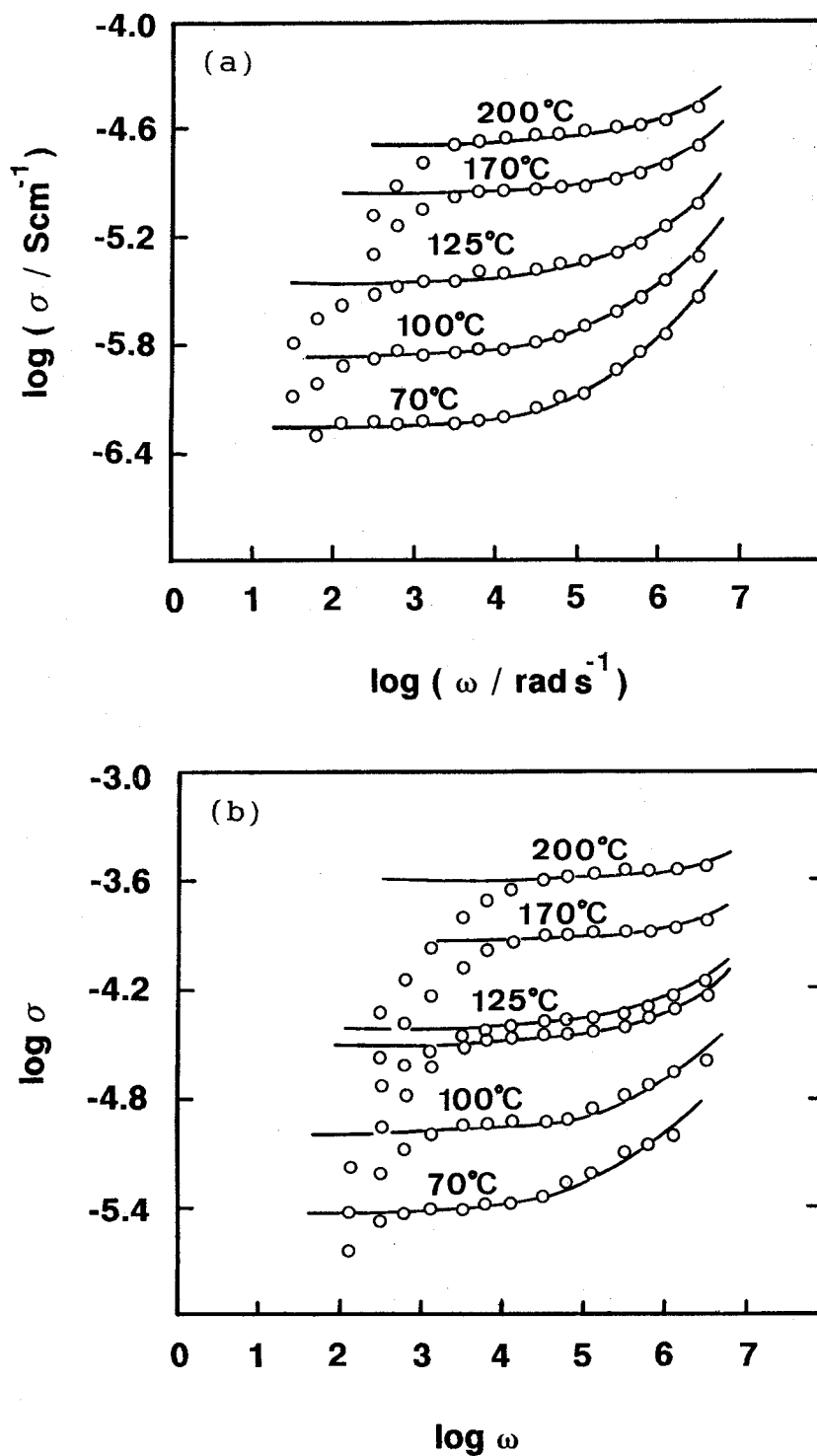
Fig. 4-8 Conductivity data of nominal (a) $Na_{1.5}Ga_{0.5}Zr_{1.5}(PO_4)_3$ and (b) $Na_{1.5}Cr_{0.5}Zr_{1.5}(PO_4)_3$ at a selection of temperatures. Solid curves are fits of $\sigma(\omega) = \sigma(0) + A\omega^n$ to the experimental data.
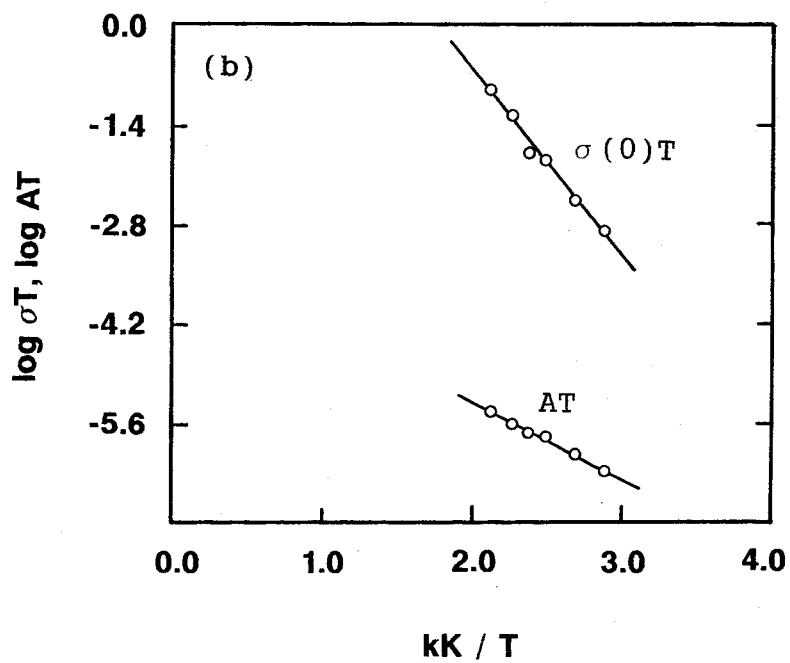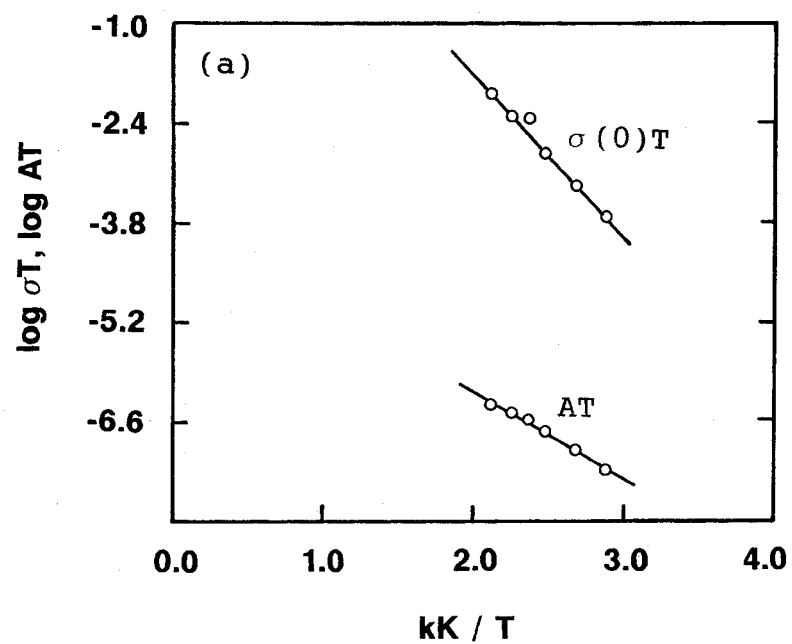
Fig. 4-9   Arrhenius plots of $\sigma(0)T$ and AT of (a) $Na_{1.5}Ga_{0.5}Zr_{1.5}(PO_4)_3$ and (b) $Na_{1.5}Cr_{0.5}Zr_{1.5}(PO_4)_3$.

1:0.65 and is consistent with 1:(1-n), where n is one of the fitting parameters in fig. 4-8. This result suggests that the activation energy of the conductivity (E_a) comes from that of the ω_p[3]. On the other hand, the ratio of the activation energies of $\sigma(0)$ and A of Ga-NZP did not agree with 1:(1-n). This is explained as the temperature dependence of mobile ion content by Almond et al. However, it is also possible that the ionic conduction originates from more than one process in the observed frequency range. Activation energies of ω_p derived from the Arrhenius plots were 30 kJ/mol and 45 kJ/mol for Ga-NZP and Cr-NZP, respectively (fig. 4-10), and the value of Cr-NZP is fairly consistent with E_a. Furthermore, ω_e, the extrapolation of ω_p to infinite temperature, was estimated to be 7.9 x 10^9 /s and 6.3 x 10^{12} /s for Ga-NZP and Cr-NZP, respectively. The ω_e of Cr-NZP corresponds to the vibrational frequency of ions typically observed in IR and Raman spectra. However, the ω_e of Ga-NZP is lower compared with other data. It can therefore be presumed that these characteristic features of c_i and ω_e of Ga-NZP are attributed to the grain boundary conduction. Segregated Na^+ ions in the grain boundary would be mainly responsible for the additional grain boundary conductivity, leading to a higher conductivity than that of NZP. It is generally recognized that the segregated insulator phase blocks the ion migration of the conductive crystal phase. However, this case showed anomalous feature of the conductivity increase enhanced by the segregated ions. This feature was similarly observed in the case of Li^+ ion conductor, $Li_{1+x}M_xTi_{2-x}(PO_4)_3$ (M: Sc^{3+}, Y^{3+}) in section 4.2.

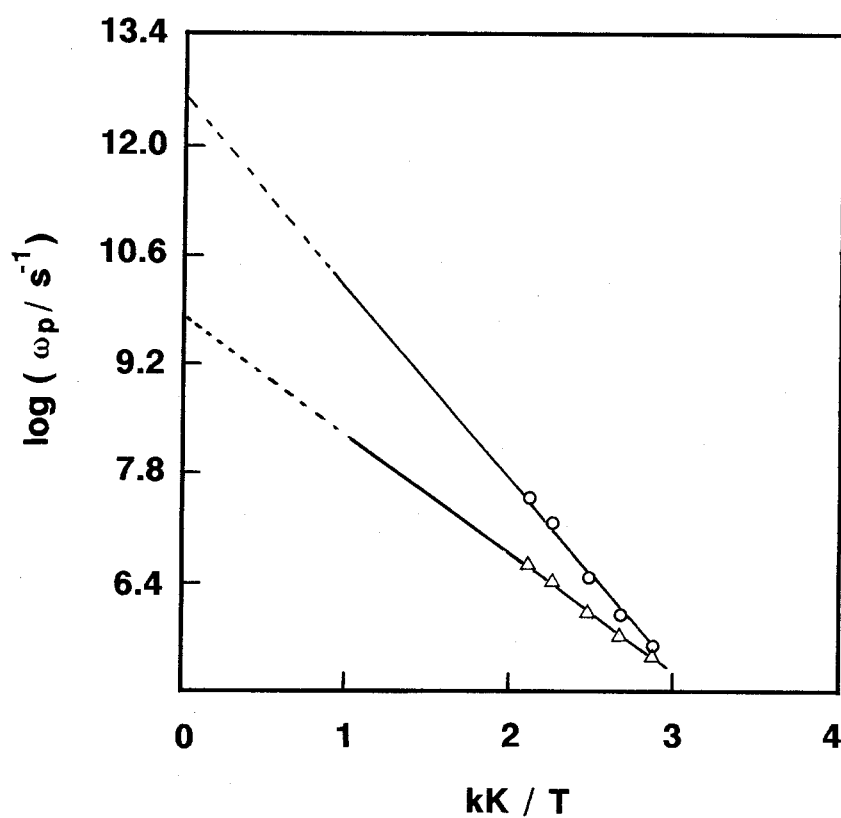This result suggests that the estimation of c_i and ω_p is

Fig. 4-10 Arrhenius plots of ion hopping rates, ω_p for $Na_{1.5}Ga_{0.5}Zr_{1.5}(PO_4)_3$ ($\triangle$) and $Na_{1.5}Cr_{0.5}Zr_{1.5}(PO_4)_3$ (O).

one of the promising techniques to investigate and distinct the
conduction properties which exist complicatedly in ceramic mate-
rials.

4.4 Lithium ortho-silicate type ionic conductors

Li_4SiO_4-based solid solutions are well known for their great increase in conductivity when aliovalent ions are substituted by silicon. Jackowska et al. prepared aluminium substituted solid solutions, $Li_{4+x}Al_xSi_{1-x}O_4$, which show an interstitial Li^+ ion conduction[8]. On the other hand, they also found $Li_{4-3y}Al_ySiO_4$ to show a vacancy conduction, when an Al^{3+} ion is substituted by three Li^+ ions. Both of them were found to have much higher conductivity than Li_4SiO_4. In the two types of conduction mechanism, the author is interested in the interstitial Li^+ conduction, because higher conductivities have been observed in the Li_4SiO_4 solid solutions system.

In this chapter, the conductivity changes with substituted ionic radii or lattice constants are investigated. Si^{4+} ions were replaced by di- or trivalent ions partially in order to increase Li^+ ion contents per a chemical formula unit. To compare the conduction properties, the chemical formula of the solid solutions was fixed into $Li_{4.2}M_xSi_{1-x}O_4$, where $x=0.2$ for M^{3+}: B^{3+}, Al^{3+}, Ga^{3+}, Cr^{3+}, Fe^{3+}, and $x=0.1$ for M^{2+}: Ni^{2+}, Co^{2+}.

4.4.1 $Li_{4.2}M_{0.2}Si_{0.8}O_4$ (M: B^{3+}, Al^{3+}, Ga^{3+}, Sc^{3+}, Cr^{3+}, Fe^{3+}, Yb^{3+}, Y^{3+}) ionic conductors

*** Experimental ***

The starting materials, Li_2CO_3, SiO_2 and one of H_3BO_4, Al_2O_3, Ga_2O_3, Cr_2O_3, Fe_2O_3, NiO, CoO were mixed mechanically in stoichiometric proportion and sintered at 800 or $900^{\circ}C$ for 10

hours. All sintered materials were identified by X-ray diffraction (XRD) patterns to be solid solutions. Signal to noise (S/N) ratios were eveluated by (200) peak in XRD patterns. Lattice constants were refined with a least-squares method using these XRD patterns $((\sin\theta)/\lambda < 0.562)$ based on structural results of Vollenkle et al.[9].

*** Results ***

Lithium orthosilicate, Li_4SiO_4, is composed of isolated tetrahedral $SiO_4{}^{4-}$ groups and positively charged Li^+ ions at the sites between $SiO_4{}^{4-}$ groups. The occupancy of Li^+ ion sites is different to each other.

Ionic conductivities at 100 and 300°C of the solid solutions as a function of the substituted ionic radius are shown in fig. 4-11. The ionic conductivity reaches a maximum at the Al^{3+} substitution.

Figure 4-12 shows the temperature dependence of the electrical conductivity σ for Al^{3+} substituted compound. The observed conductivity at 300°C was 1.6×10^{-3} Scm^{-1} and the activation energy was 56 kJ/mol. A conductivity enhancement of two orders of magnitude was observed compared with $\sigma_{300°C} = 1.8 \times 10^{-5}$ Scm^{-1} of non-doped compound. These data agree with those of Jackowska et al. The conductivity increase may be due to the increase of charge carrier concentration.

The compounds substituted with trivalent ions, Ga^{3+}, Cr^{3+}, Fe^{3+}, which is larger in size than Al^{3+}, showed a lower level of conductivity than Al^{3+} substituted compound. Since electrical conductivity is composed of the product of carrier concentration
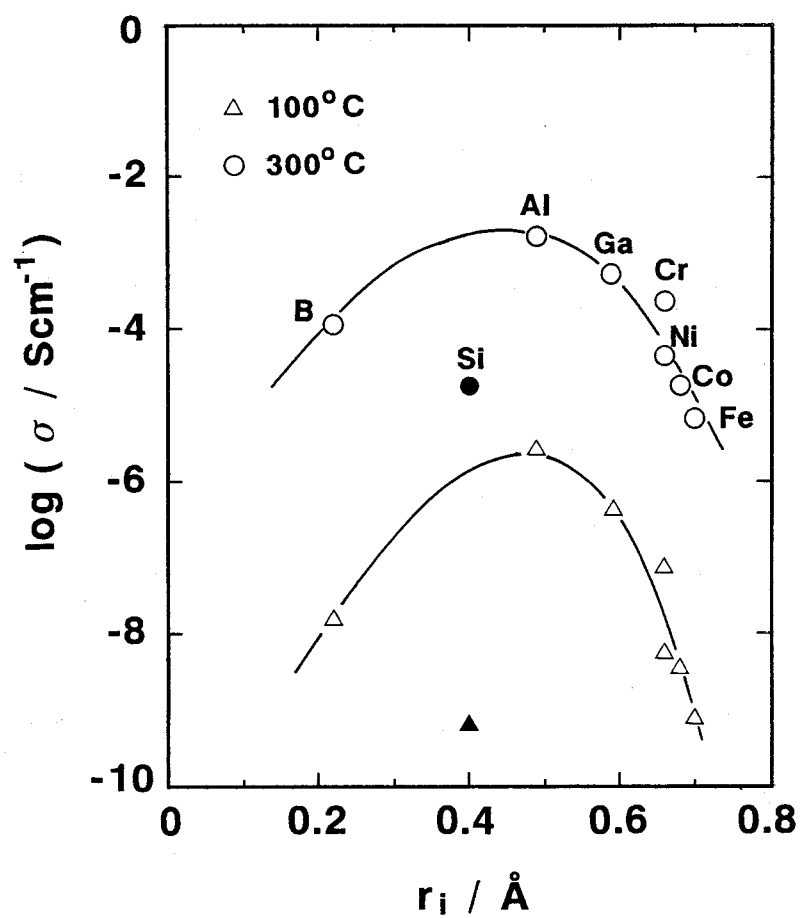
Fig. 4-11 Electrical conductivity of Li_4SiO_4-based compound as a function of tetrahedrally coordinated ionic radius (r_i).
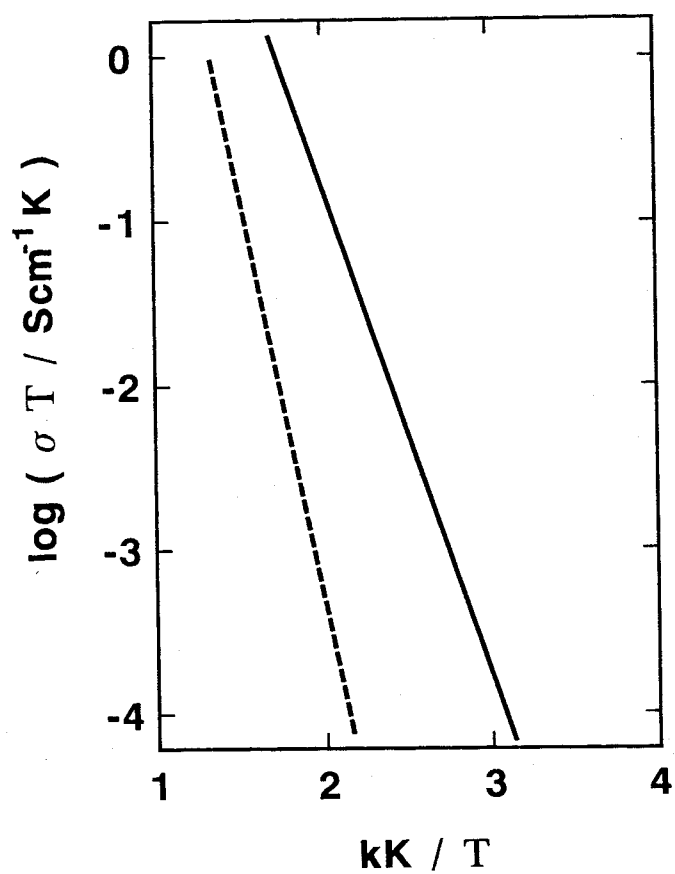
Fig. 4-12 Temperature dependence of electrical conductivities of
Li_4SiO_4 (----) and $Li_{4.2}Al_{0.2}Si_{0.8}O_4$ (——).

and ionic mobility, this conductivity decrease can be assumed to be dependent on the mobility. Because the Li^+ ion contents were fixed to4.2 per a chemicalformula unit, it is assumed that charge carrier concentration should be constant among these compounds. The ionic mobility would unequivocally depend on the potential barrier height for ionic migration.

The size of MO_4^{5-}, where M is Ga, Cr, Fe, would be larger than that of AlO_4^{5-} in the order of M^{3+} ion size. The potential barrier against Li^+ ion migration would be higher if the oxygen-oxygen distance between MO_4^{5-} was shorter due to the longer M-O distance within MO_4^{5-}.

Tranqui et al. reinvestigated the crystal structure of Li_4SiO_4 with monoclinic cell, a=11.546, b=6.090, c=16.645, and β =99.5[11]. They found that the structural principle is the same as that analyzed by Vollenkle et al.[2]. The results of Vollenkle et al. are used as starting parameters for the refinement because of simpler representation. Figure 4-13 shows the dependence of cell parameters on substituted ionic radius. The dependence of b parameter length on the ionic radius showed a similar shape to that of conductivity, but a, c and β did not show a clear trend to the ionic radius. The unit cell volume, therefore, showed a similar dependence on ionic radius to that of the conductivity (fig. 4-13(e)). It is assumed that volume expansion would be attributed to the extra lithium ion content (x=0.2) and MO_4 tetrahedron expansion. A simple calculation estimates the contribution of the MO_4 expansion to the unit cell volume expansion to be only 5% when Si^{4+} are substituted by 0.2 Al^{3+}. Therefore, increased Li^+ ions should be largely responsi-
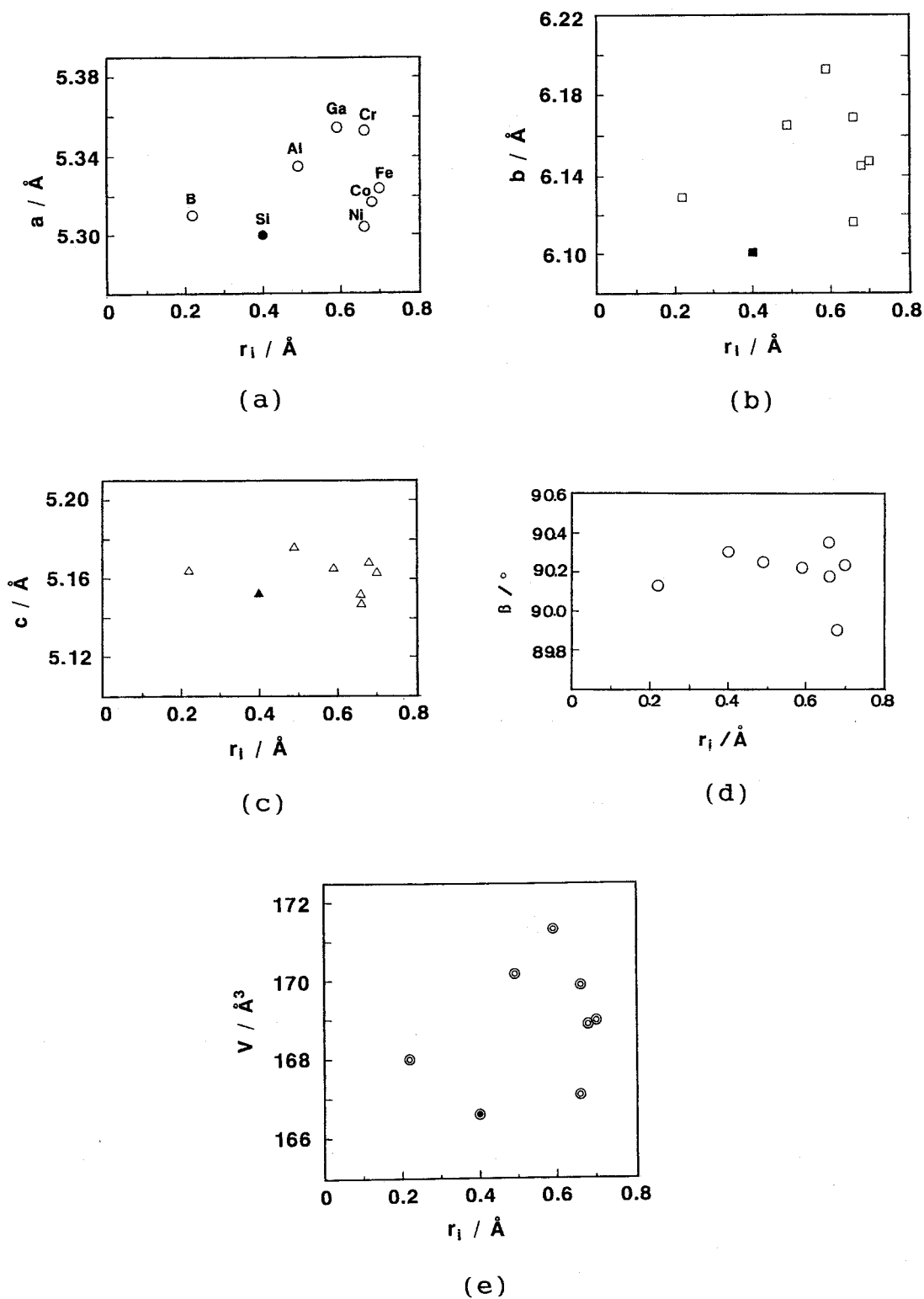
Fig. 4-13   Monoclinic cell parameters of (a) a, (b) b, (c) c, (d) β and (e) volume, V, as a function of ionic radius (r_i).

ble for the volume expansion.

The author speculates why Ga^{3+}, Cr^{3+}, Fe^{3+} substituted compounds have lower conductivity and smaller unit cell volume than Al^{3+} substituted compound in this order. Vollenkle's structure shows that one of tetrahedral M-O vector which has large b component directs against a Li^+ site. If a weak attractive bond would be created between the Li^+ ion and O atom of MO_4, the Li^+ ion could be trapped at that site. This would be one of the reasons for lowering the conductivity and smaller unit cell volume.

Moreover, tetrahedrally coordinated Cr^{3+} and Fe^{3+} ions can be assumed to have deformed T_d symmetry because of non-spherical 3d orbitals. Therefore, an irregular atomic arrangement may be suggested in these compounds. The S/N ratio decrease of the XRD powder pattern due to the line width broadening was observed with increasing substituted ionic radius as shown in fig. 4-14. This is also presumed to be one of the reducing factors of the conductivity.

The compounds substituted with divalent ions, Ni^{2+}, Co^{2+}, which are also larger in size than Al^{3+} ion, showed a lower conductivity which could be responsible for the trapped Li^+ ion content as discussed above. The content of these divalent ions on solid solutions is a half of that of trivalent ion substitution. Therefore, the contribution of the MO_4 expansion to the volume expansion of the unit cell would be much smaller. Tetrahedrally coordinated Ni^{2+} and Co^{2+} ions can be assumed to have fairly deformed T_d symmetry. The observed low S/N ratio and line width broadening of the XRD pattern suggest irregularity of atomic arrangements. These can be the origins of the conductivi-
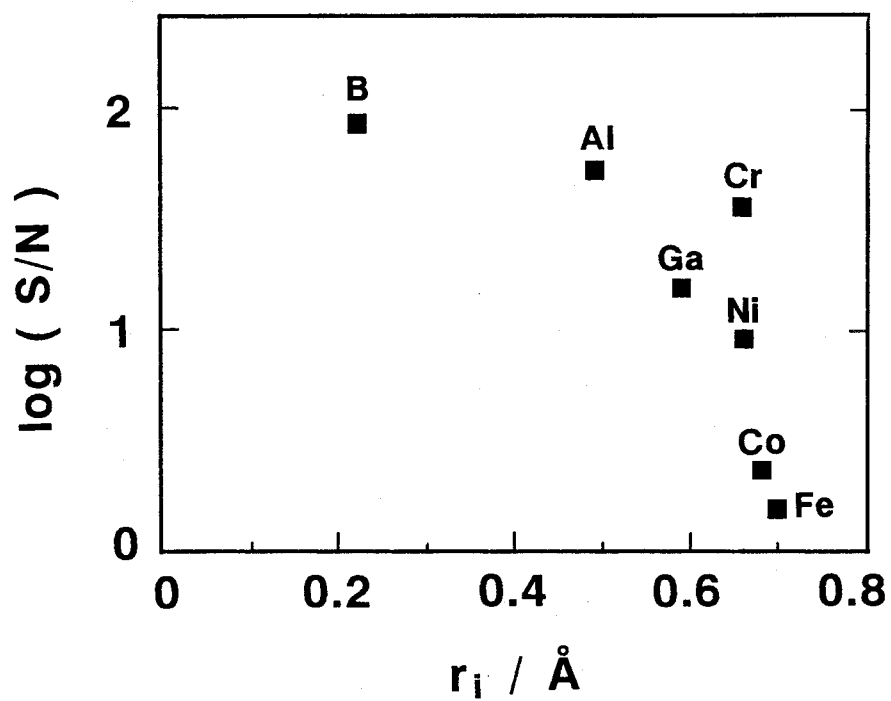
Fig. 4-14 Observed S/N ratio as a function of ionic radius (r_i).

ty decrease.

For the boron substituted compound, the electrical conductivity of 1.1×10^{-4} Scm^{-1} at 300°C was observed. This is higher than that of the non-doped compound, but considerably lower than that of the Al^{3+} substituted compound.

A larger unit cell volume in $Li_{4.2}B_{0.2}Si_{0.8}O_4$ was observed than that of the non-doped compound which is also shown in fig. 4-13(e). The B-O distance of 1.52A within BO_4^{5-} is fairly shorter than the Si-O distance of 1.66A within SiO_4^{4-}[12]. Therefore, the volume expansion of B^{3+} substituted compound should arise mainly from the extra lithium ion content (x=0.2). This can explain the higher conductivity of the B^{3+} substituted compound than that of non-doped compound.

In comparison with the Al^{3+} substituted compound, the unit cell volume of the B^{3+} substituted compound should be smaller because the ionic radius of B^{3+} is smaller than that of Al^{3+}. This may cause the low conductivity compared with the Al^{3+} substituted compound.

4.4.2 $Li_{4+x}B_xSi_{1-x}O_4$ (0<x<0.7) ionic conductors

B^{3+} substituted compound, $Li_{4.2}B_{0.2}Si_{0.8}O_4$, showed the highest signal to noise (S/N) ratio and no extra peaks in the X-ray diffraction (XRD) pattern (4.4.1). This suggests a greater B^{3+} solubility limit with the occupation of a larger amount of interstitial mobile Li$^+$ ions, indicating higher conductivity. In this section, the author discusses the changes of the conductivity and the crystal lattice parameters as a function of B^{3+} con-

tent in the $Li_{4+x}B_xSi_{1-x}O_4$ system.

*** Experimental ***

The compound $Li_{4+x}B_xSi_{1-x}O_4$ were prepared with x varying in steps Δx of 0.1 by a conventional solid state reaction with the starting materials Li_2CO_3, SiO_2 and H_3BO_3. All mixtures with each stoichiometric ratio corresoponding to a selected composition were sintered at 800°C for 10 hours and confirmed by XRD patterns to be solid solutions. S/N ratios were evaluated by the peak height of the (200) peak against the _ise level. Lattice constants were refined with the least-squares method from the observed peaks ($\sin\theta/\lambda < 0.562$) based on the structural results of Tranqui et al.[13].

*** Results ***

Solubility limit of B^{3+} in the system $Li_{4+x}B_xSi_{1-x}O_4$

The XRD S/N ratio and melting point of the $Li_{4+x}B_xSi_{1-x}O_4$ compounds decreased gradually with the increase of B^{3+} content. Significant extra peaks assigined to Li_2CO_3 appeared for larger B^{3+} contents (x>0.5). The peak intensity grows on standing for a few months at room temperature, which suggests a reaction with CO_2 in air. This deduction suggests, in turn, that the $Li_{4+x}B_xSi_{1-x}O_4$ system may be a good Li^+ ionic conductor. The solubility limit of B^{3+} in Li_4SiO_4 was found to be x=0.7; the mixture with x=0.8 gave a different phase. This value is quite a bit larger than the limiting composition of other substituents, e.g. x=0.4 for the Al^{3+}-substituted system.

Conductivity of solid solution $Li_{4+x}B_xSi_{1-x}O_4$

The ionic conductivities of several compositions are shown in fig. 4-15 in Arrhenius format. An apparent change in slope (activation energy) was not observed in any of the compounds up to 450°C in contrast to the results of Jackowska and West [8], who reported a change in slope at 470°C for $Li_{4+x}Al_xSi_{1-x}O_4$ (x=0.1, 0.2), and of Shannon et al.[14], who reported a change at 180°C for Li_4SiO_4.

All the solid solutions have higher conductivity than Li_4SiO_4. The conductivity reaches a maximum for the composition with x=0.5. The activation energy, E_a, extracted from the Arrhenius plot of conductivity also reaches a minimum at this composition.

It is helpful to understand the origin of the above conductivity enhancement with the decrease of activation energy. Therefore, the carrier concentration and hopping rate of the Li^+ ions were estimated from the frequency dependence of the ac conductivity following the procedure of Almond et al.[3,4].

Conductivity data as a function of frequency at several temperatures for $Li_{4.5}B_{0.5}Si_{0.5}O_4$ are shown in fig. 4-16. The solid lines were obtained by least-squares fit. The values of $\sigma(0)$ and A used for these fits are shown in fig. 4-17 with the conventional Arrhenius format. In each case, the activation energies of $\sigma(0)$ and A were in the ratio of 1:(1-n). This result means that both the activation energies of $\sigma(0)$ and A are consistent with that of the hopping rate, ω_p. This means that the concentration of c of mobile ions involved in K is independent of temperature. The hopping rates ω_p calculated from the
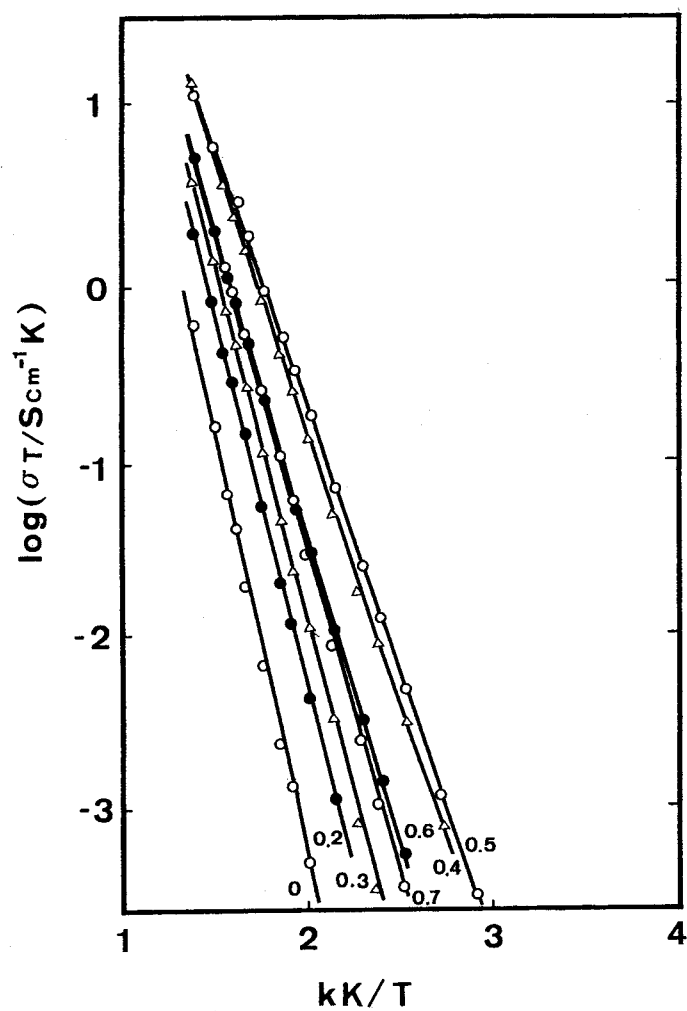
Fig. 4-15　Temperature dependence of electrical conductivity of $Li_{4+x}B_xSi_{1-x}O_4$.　x is marked on each.

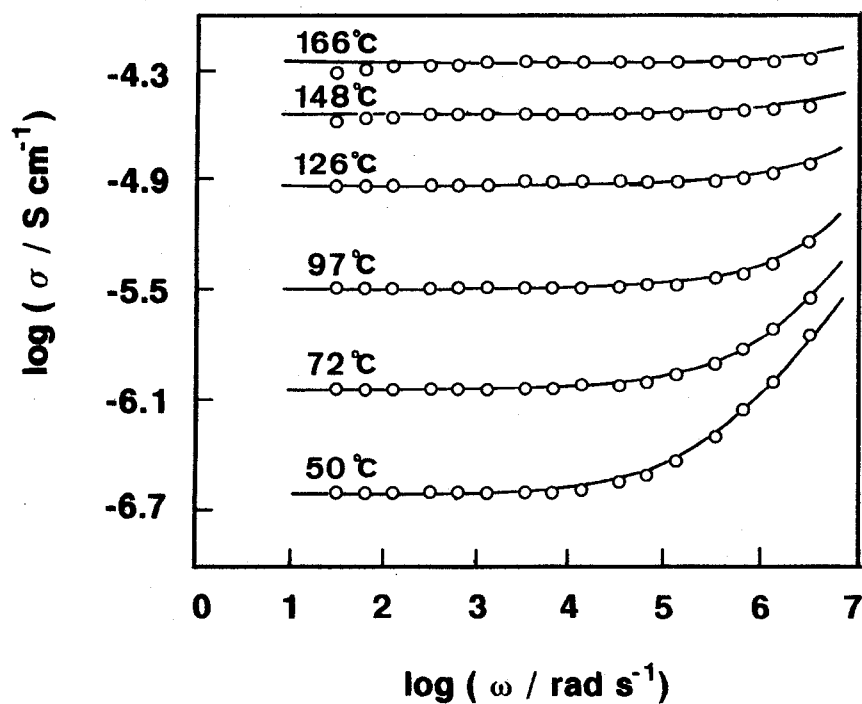Fig. 4-16 Conductivity data for $Li_{4.5}B_{0.5}Si_{0.5}O_4$ at a selection of temperatures. Solid curves are fits of equation (2-12) to the experimental data.
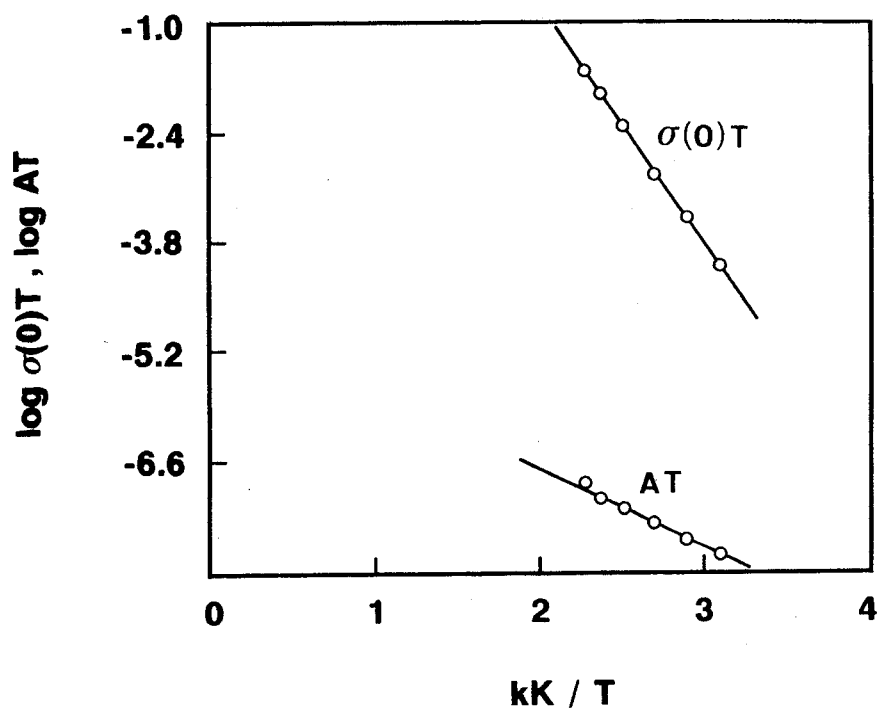
Fig. 4-17 Arrhenius plots of $\sigma(0)T$ and AT.

same data are shown in fig. 4-18. This also indicates that the thermal activations of these conductivities are caused by those of the hopping alone. The effective attempt frequencies ω_e obtained from the infinite temperature intercepts were 3×10^{14} and 2×10^{14} Hz for Li_4SiO_4 and $Li_{4.5}B_{0.5}Si_{0.5}O_4$, respectively. These frequencies reproduce the corresponding vibrational frequency, $\sim 10^{13}$ Hz, fairly well. Therefore, the treatment for ac conductivity proposed by Almond et al. is acceptable for this system. Moreover, the temperature independence of carrier concentration was proved for all of $Li_{4+x}B_xSi_{1-x}O_4$ compounds.

Figure 4-19 shows the c and ω_p at 100^OC as a function of B^{3+} content x. The maxima of c and ω_p were observed at $x \sim 0.5$, similar to the case of ionic conductivity. The increase in c is about one order of magnitude, whereas the increase in ω_p at 100^OC is more than two orders of magnitude compared with that of Li_4SiO_4. Therefore, the observed conductivity enhancement of $Li_{4+x}B_xSi_{1-x}O_4$ at 100° is mainly due to the increase of hopping rate.

Changes of lattice parameters and the Li^+-ion conduction mechanism in $Li_{4+x}B_xSi_{1-x}O_4$ solid solutions

Figure 4-20 shows the observed lattice parameters as a function of x. The crystallographic a- and c-axes and the cell volume, V, increase with x, whereas the b-axis length shows a unique x dependence, i.e., the rate of increase is twice as great as those of the a- and c-axis lengths until x=0.5 and gradually decreases with a further increase of x. This dependence, with a maximum value at x=0.5, is similar to that of the conductivity.
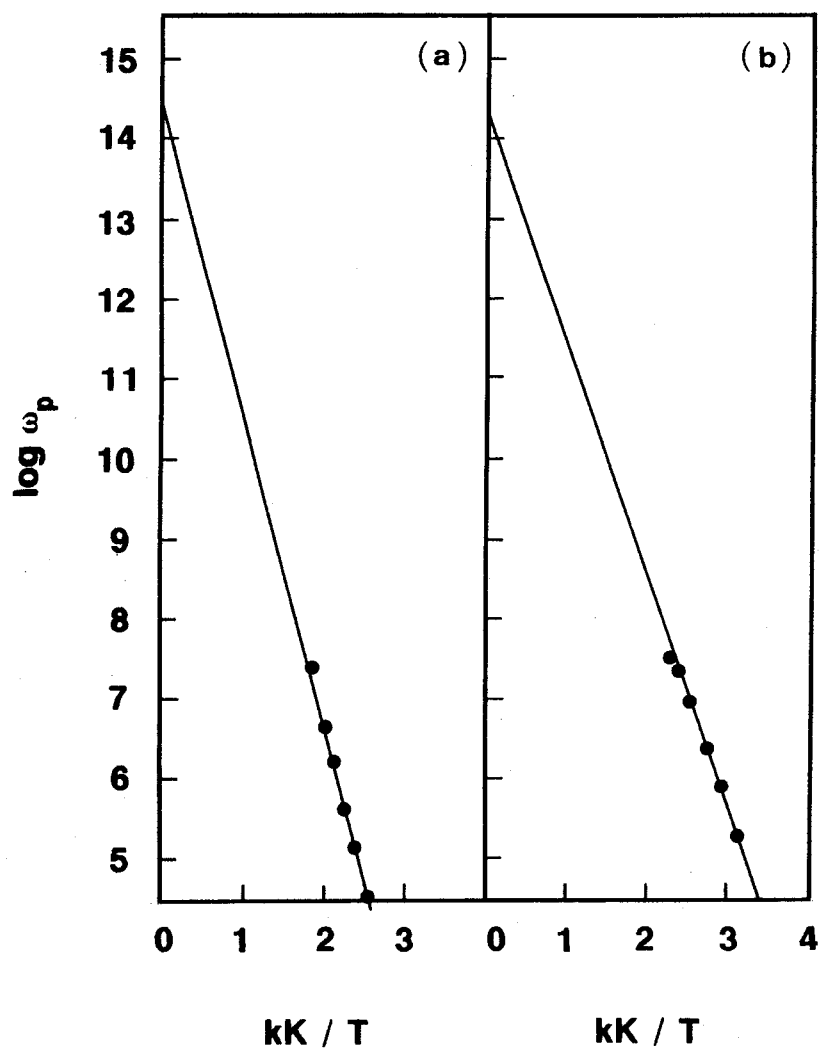
Fig. 4-18 Arrhenius plots of ion hopping rates, ω_p for (a) Li_4SiO_4 and (b) $Li_{4.5}B_{0.5}Si_{0.5}O_4$.
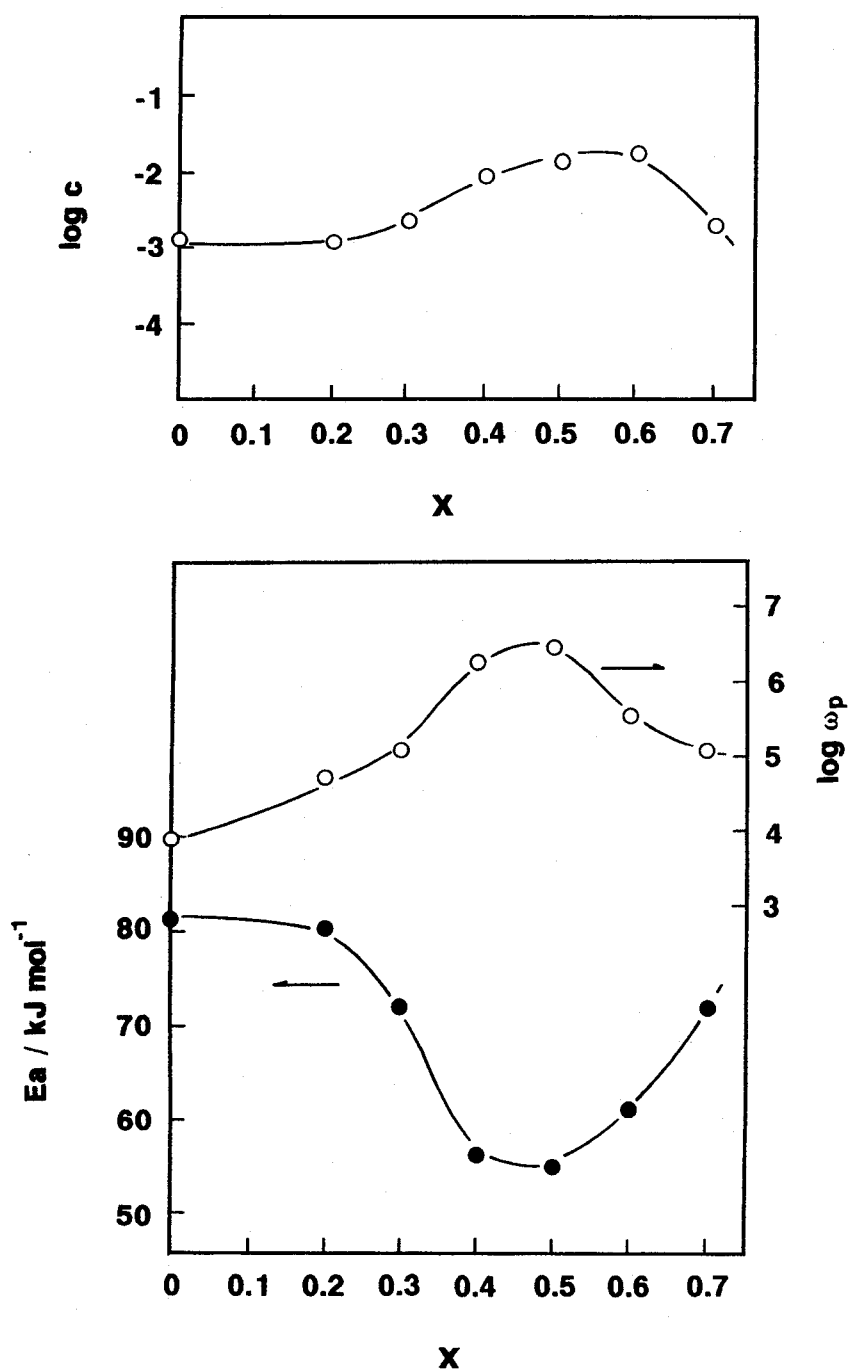
Fig. 4-19 Change of (a) carrier concentration (c_i) and (b) hopping rate (ω_p) with its activation energy (E_a) as a function of x at 100°C in $Li_{4+x}B_xSi_{1-x}O_4$.
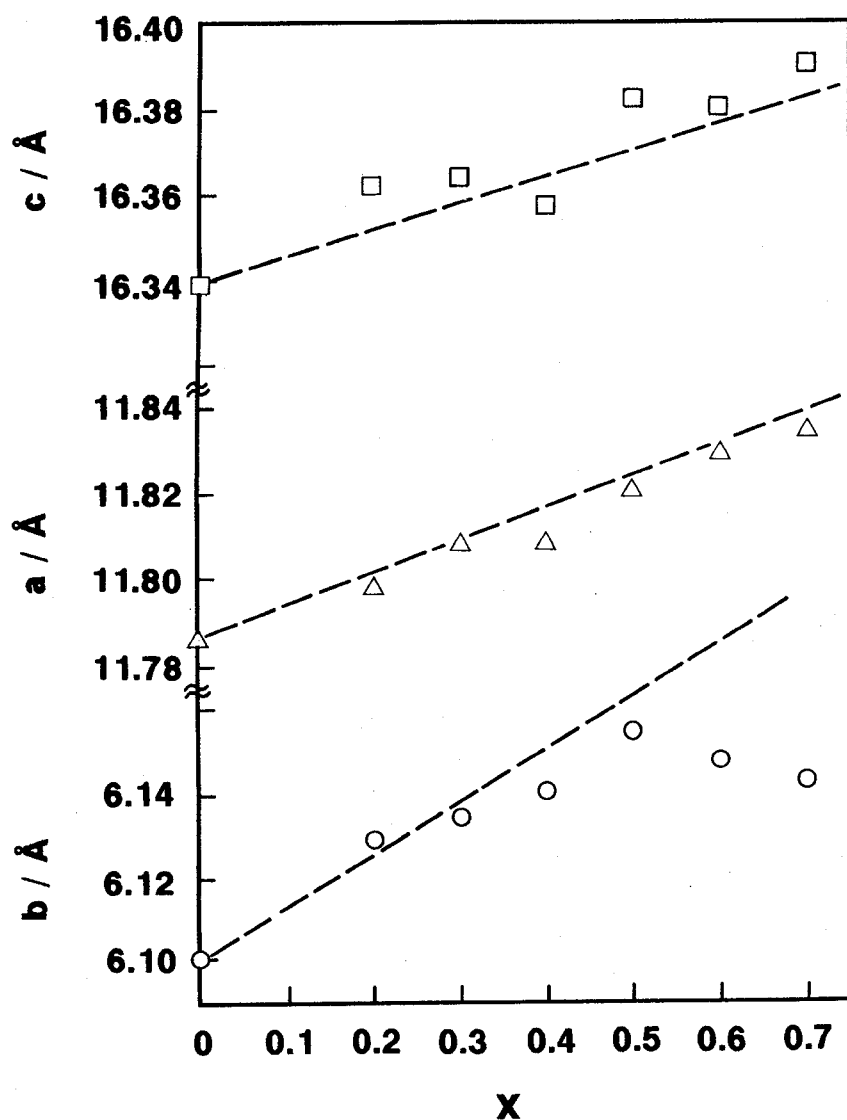
Fig. 4-20 Lattice constants (monoclinic unit) for the $Li_{4+x}B_xSi_{1-x}O_4$ systems. Broken lines are fits of the parameters in equation (4-1) to the experimental data.

The author describes the x dependence of crystal structure and conductivity to discuss the Li^+-ion conduction mechanism.

Li_4SiO_4 crystallizes in the monoclinic space group $P2_1/m$ with a=11.564, b=6.090, c=16.645 A, β =99.5° and Z=14[13]. The Li atoms are ordered and occupy 19 of 42 sites in the sevenfold supercell (fig. 4-21) as compared with the cell of Vollenkle et al.[15]. The LiO_4, LiO_5 and LiO_6 polyhedra are linked by edge- and corner-sharing. There is good three-dimensional connectivity between Li sites with distances of less than 2.9A. The ordered nature of Li_4SiO_4 is consistent with the low ionic conductivity, whereas the good conductivity of B^{3+}-substituted $Li_{4+x}B_xSi_{1-x}O_4$ is consistent with the good Li-site connectivity and the partial occupation of Li interstitials (Li^+ ion disordered state), which results in the expansion of the cell volume with an increase of x in the range x<0.5. The experimental conductivity data show that the increase of x is attributable to the increase of mobile ion content and the hopping rate, as shown in the previous section.

Once any Li interstitial sites, which were first introduced by Vollenkle et al.[15], are occupied by Li^+ ions (model A), an extremely short Li^+-Li^+ distances (~1A) are unavoidable. The summation was carried out over all the Li^+-Li^+ repulsive forces as well as Li^+-O^{2-} (~2A) attractive and Li^+-Si^{4+} (~3.5A) repulsive forces. Hence, the total Coulomb force, F, can be described by

$$F = k \frac{q_i q_j}{r^2} ,$$
(4-1)

where k is a constant, q_i and q_j are point charges of individual
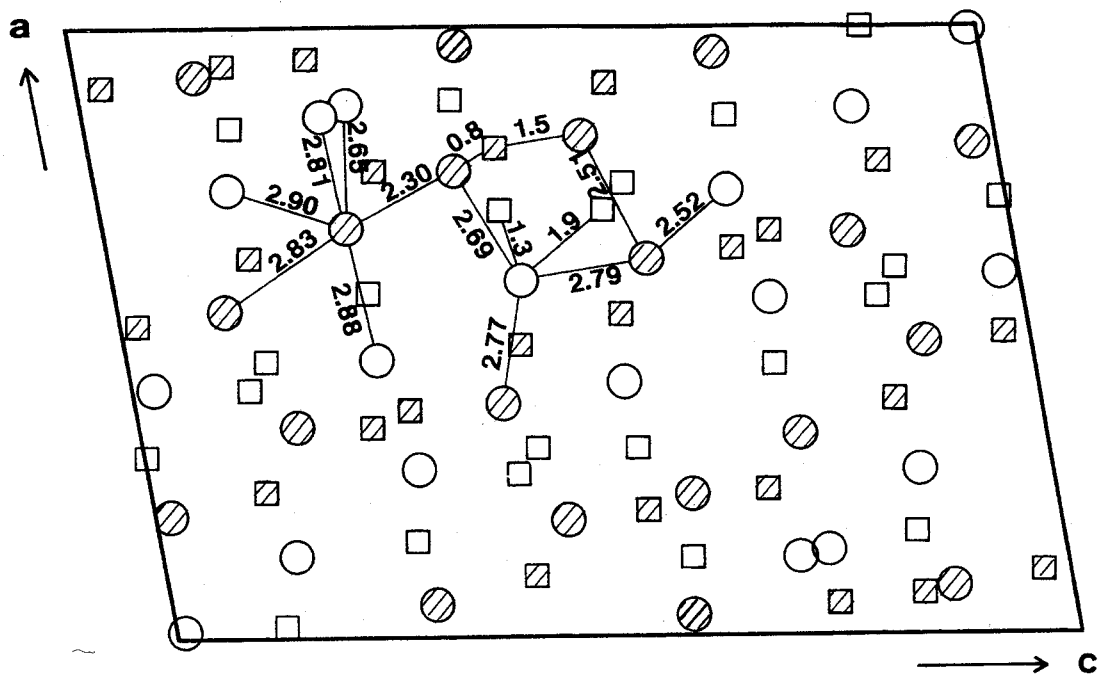
Fig. 4-21 Projection along b axis of all Li atoms (O) and all Li available sites (□) for the interstitially occupied Li atoms. Open circles and squares are at y=1/4 and 3/4; shaded circles and squares are at y=0 and 1/2, respectively. Possible Li-Li distances are indicated.

atoms, and r is the interatomic distance. As a result of the above F calculation, the local atmosphere at Li sites was repulsive. If it is assumed that the repulsive force makes an expansion of cell volume, the relative expansion rates along individual directions could be described as

$$
\begin{bmatrix} \Delta a \\ \Delta b \\ \Delta c \end{bmatrix} = \begin{bmatrix} 0.62 \\ 1 \\ 0.49 \end{bmatrix}
\qquad (4-2)
$$

This is consistent with the anisotropy of experimental results, i.e. a unique increasing rate of the b axis. Broken lines in fig. 4-20 show that the above calculated results fit the experimental ones in the region $0<x<0.5$. The strong anisotropy of the total repulsive force mainly arises from the Li^+-Li^+ repulsion rather than Li^+-O^{2-} or Li^+-Si^{4+} interactions. This structural anisotropy corresponds to an increase of the two-dimensionality in Li^+-ion conduction. This may give rise to two effects: (i) a total conductivity decrease because of the reduction of the Li^+-ion hopping probability along the b direction, and (ii) a hopping rate increase normal to the b-axis because of the elongation of the Li-O bond length along the b direction and because of the consequent reduction of the hindrance by O^{2-} ions against Li^+-ion hopping. The latter can interpret the experimental results shown in fig. 4-19.

In the region $x>0.5$, only the b-axis length decreases with increasing x. It could be assumed that the concentration of the planar BO_3^{3-} triangles would increase compared with BO_4^{5-} tetra-

hedra (model B) when Si atoms are substituted by B atoms. These changes of local structure have already shown to occur in borosilicate glass[16]. Figure 4-22 illustrates how BO_3^{3-} arise from BO_4^{5-}. Tranqui et al.[13] have also shown the unique long Si-O bond length (~1.68A) in a SiO_4^{4-} compared with the other three (~1.62A) in a SiO_4^{4-} tetrahedron. This indication suggests the following equilibrium with increasing x:

$$SiO_4^{4-} \rightarrow BO_4^{5-} + Li^+ \rightleftharpoons BO_3^{3-} + LiO^- \qquad (4-3)$$
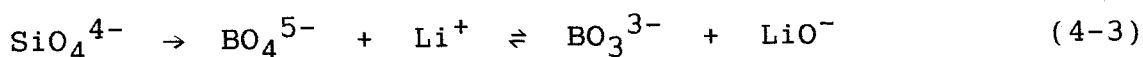
Equation (4-3) indicates the same content of chemical species of BO_3^{3-} and LiO^- depending on x. On the other hand, the B-O bond length of 1.42A in BO_3^{3-} is shorter than that (1.52A) in BO_4^{5-} [17]. This suggests the reduction in cell volume with increasing x. The anisotropic reduction to each crystallographic axis may be interpreted by the equilibrium in equation (4-3). Namely, the oxygen atom with a uniquely long B-O bond would recombine with the nearest Li^+ ion rather than remain as one of the members of BO_4^{5-}, resulting in LiO^- and BO_3^{3-} formation. Under an assumption that a B atom is displaced from the center of a BO_4^{5-} tetrahedron to the center of a BO_3^{3-} triangle, the summation was carried out over all the individual crystallographic axis components of reduced bond length; only the b-axis length was reduced whereas the a and c lengths were not affected. This is consistent with the experimental results in the range x>0.5. Moreover, the model B allows interpretation of the reduction of the conductivity. Namely, Li^+-ion trapping due to LiO^- formation might result in the reduction of the mobile Li^+-ion concentration,
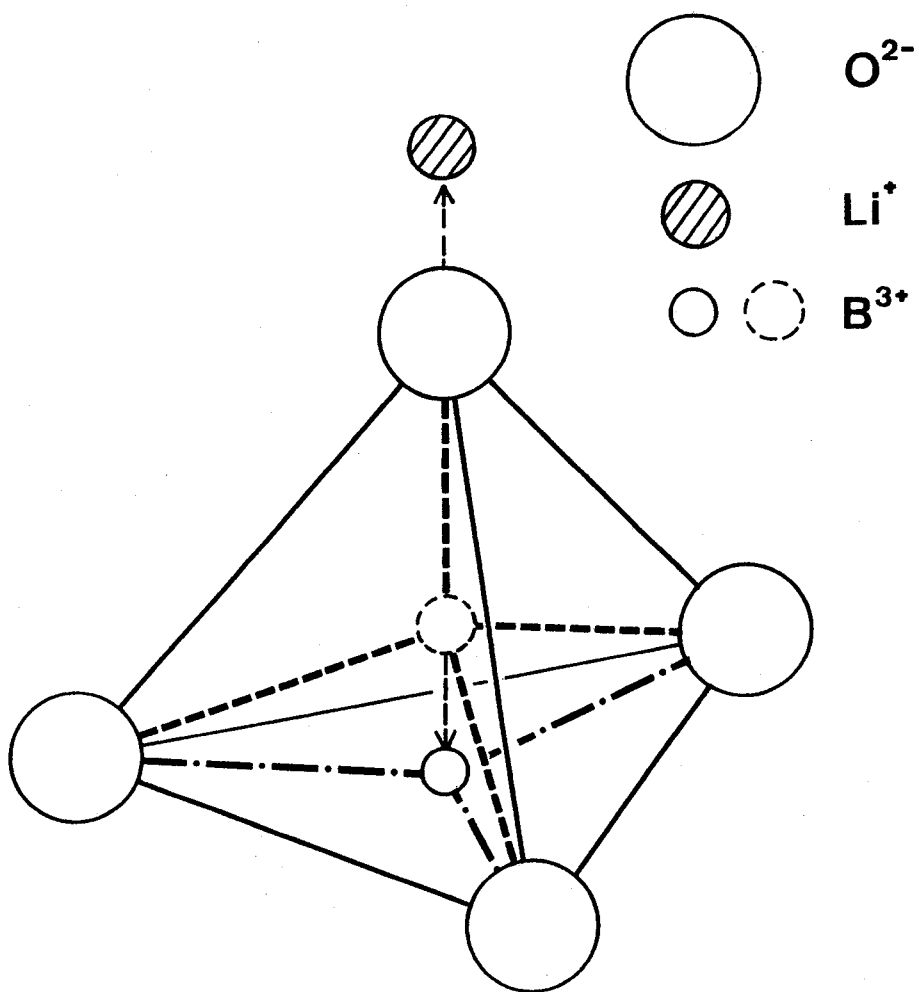
Fig. 4-22   Structural relationship between the tetrahedral BO_4 and triangular BO_3.

which would be consistent with the results shown in fig. 4-19.

An ion coupling model might explain a conductivity decrease with increasing x at higher Li^+-ion concentration as has been frequently suggested for some superionic crystals, e.g., ZrO_2[18,19]. But the author has no indication that this model applied to the Li_4SiO_4 system.

In conclusion, the author has analyzed the conductivity so as to separate the hopping rate and the mobile ion concentration. Both components have maxima at x=0.5. Also, a simple point-charge model can interpret the reason why the x dependence of the b-axis length is unique and corresponds to that of the conductivity.

References

[1] B. E. Taylor, A. D. English and T. Berzins, Mat. Res. Bull., 12, 171 (1977).

[2] H. Aono, E. Sugimoto, Y. Sadaoka, N. Imanaka and G. Adachi, J. Electrochem. Soc., 137, 1023 (1990).

[3] D. P. Almond, G. K. Duncan and A. R. West, Solid State Ionics, 8, 159 (1983).

[4] D. P. Almond and A. R. West, Solid State Ionics, 9/10, 277 (1983).

[5] H. Aono, E. Sugimoto, Y. Sadaoka, N. Imanaka and G. Adachi, Chem. Lett., 331 (1990).

[6] H. Aono, E. Sugimoto, Y. Sadaoka, N. Imanaka and G. Adachi, Chem. Lett., 1825 (1990).

[7] H. Y-P. Hong, Mat. Res. Bull., 11, 173 (1976).

[8] K. Jackowska and A. R. West, J. Mat. Sci., 18, 2380 (1983).

[9] H. Vollenkle, A. Wittmann and H. Nowotny, Monatsh. Chem. 99, 1360 (1968).

[10] H. Yanagida, Kinzoku (Metals) 41 (1988).

[11] D. Tranqui, R. D. Shannon and H.-Y. Chen, Acta Cryst., B25, 1046 (1970).

[12] R. D. Shannon and C. T. Prewitt, Acta Cryst., B25, 1046 (1970).

[13] D. Tranqui, R. D. Shannon, H.-Y. Chen, S. Iijima and W. H. Baur, Acta Cryst., B35, 2479 (1979).

[14] R. D. Shannon, B. E. Taylor, A. D. English and T. Berzins, Electrichim Acta, 22, 783 (1977).

[15]   H. Vollenkle, A. Wittmann and H. Nowotny, Monatsh. Chem., 99, 1360 (1968).

[16]   A. R. West, Solid State Chemistry and its Applications (Wiley, New York, 1984) p.609.

[17]   R. D. Shannon and C. T. Prewitt, Acta Cryst., B25, 925 (1969).

[18]   J. A. Kilner and C. D. Waters, Solid State Ionics, 8, 201 (1982).

[19]   D. Y. Wang, D. S. Park, J. Griffith and A. S. Nowick, Solid State Ionics, 2, 95 (1981).

[20]   K-D. Kreuer, H. Kohler and J. Maier, in: High Conductivity Solid Ionic Conductors, ed. T. Takahashi (World Scientific, 1989) p.242.

[21]   C. Delmas, J-C. Viala, R. Olazcuaga, G. le Flem and P. Hagenmuller, Solid State Ionics, 3/4, 209 (1981).

5. Discussion

Properties of ceramic materials depend both on the characters of composed particles and grain boundaries. In particular, it has been suggested that the grain boundary has the significant effect on many kinds of ceramic functions. The mechanical strength of most ceramics is typically influenced by the grain boundary character, i.e., it largely depends on the sintering degree. In the application of electroceramics, anomalous and useful properties arise from the grain boundary phenomena. Composite ceramics have an additional regime, i.e., interface. Interfaces where different kinds of particles meet together have a possibility to produce new properties because the polarization or transport phenomena, due to an abrupt change of their chemical potentials at the interface, can be expected.

In the composite ceramic electrolyte, interfacial conductivity is a principal component of the observed ion conductivity. Chapter 3 describes that electrical conductivities of the composite have enhanced compared with those of the original ionic conductor when the insulator particles such as PZT and solid superacid were dispersed into ionic conductor NZS. The conductivity enhancement of composite electrolytes has been widely observed in the metal halide/alumina system. And many attempts have been done to explain the mechanism of this interfacial anomalous phenomena. However, no model is available not only in the explanation of the enhancement but in designing composite solid electrolytes. An acceptable model should contain (i) what is essential for the high conductivity, and

(ii) how the special ion conductive layer at the interface can be created.

In this chapter, discussion will be concentrated on the above two subjects.

5.1 Essential concept of ionic conductivity

5.1.1 Factors which are responsible for the ionic conductivity in the solid materials

There are four main factors which affect the ionic conduction properties in the solid materials.

(a) Structural features would be an important factor which determine the conduction properties of ionic conductors. This is appears from the experimental results that mobile ions in the conductor could migrate successively in the structure when sufficient energy for activation is given to the ions. However, there are no obvious dimensional features that a material must have to show the high conductivity because the good ionic conductors include 1D structures, layer structures and three dimensional structures composed of framework and open channels. At present, there would be no consistent features which explain the relationship between the ionic conductivity and the structural features.

(b) Bonding features of the material is one of the factors of ionic conduction properties. 'Soft' covalent bonding which is constructed with polarizable atoms (ions) leads to higher ionic conductivity than 'hard' ionic bonding because the polarizable

ions would be deformed more easily in the process of migration through the channels in the structure. This is proved from the results that AgI has a higher conductivity than other halides, and the cupper halide has a higher conductivity than alkali halides such as LiCl and NaCl.

(c) A large number of the mobile ion with the sufficient empty sites which are available for them to jump into is requisite for the high conductivity. Moreover, it is necessary for ion migration that the site occupancies should not be too high and the distance between these sites should be available for one ion hop (a few angstrom), resulting in the decrease of activation energy for ion migration.

(d) Cooperative interactions between mobile ions and/or mobile ions and the framework would affect not only the mobility but the mobile ion content. Some phenomena like mixed alkali effects have been observed in which the cooperative nature leads to the reduction of the conductivity.

5.1.2 Definition of 'defect core structure'

If the above conditions are satisfied, a highly ion conductive material would be designed. And removing limitation or constructing a proper structure for ion migration will enhance the conductivity.

Substitution of one host ion by another ion with different valence introduces some defects such as interstitial ions and vacancies. This is one of the conventional way to enhance the ionic conductivity.

Suppose that additional Li^+ ions are introduced in a Li_4SiO_4 crystal by replacing B^{3+} ion for Si^{4+} ions ($Li_{4+x}B_xSi_{1-x}O_4$). Figure 5-1 schematically represents the preference position of additional Li^+ ion, i.e., the available Li^+ site in the vicinity of BO_4^{5-} ion. This site would have slightly higher occupation rate compared with other sites in the neighbour of SiO_4^{4-} ion due to the stability of charge conpensation. This complex of Li^+(interstitial)-BO_4^{5-} would make the neighbour ions displaced or perturbed in bonding nature with host atoms. Here we define 'defect core structure' as the deformed structure composed of the complex, displaced ions and polarized ions in the ordinary host lattice. This idea is similar to that of Frenkel defects, and this should be the origin of the ion migration as described below.

Ordered Li_4SiO_4 is monoclinic with space group $P2_1/m$ and an unit cell of a=11.546A, b=6.090A, c=16.645A, β=99.5°[1]. The Li atoms are statically ordered and occupy only 19 of 42 sets of equivalent positions in the sevenfold supercell which is identical to the above unit cell. These occupied 19 sets can be divided into two groups. The first is made up of ten sets (subcells) of special equivalent positions [Li(2) x 4 subcells (i.e., all Li(2) sites of only 4 subcells are occupied in the supercell), Li(3) x 3 subcells, Li(6) x 3 subcells] with a multiplicity of two as these are located on the mirror planes. The second group consists of nine sets (subcells) of general equivalent positions [Li(1) x 4 subcells, Li(4) x 3 subcells, Li(5) x 2 subcells] with a multiplicity of four. Thus, two times ten and four times nine add up to the 56 Li atoms occupying 56 sites (V_s) out of a possi-
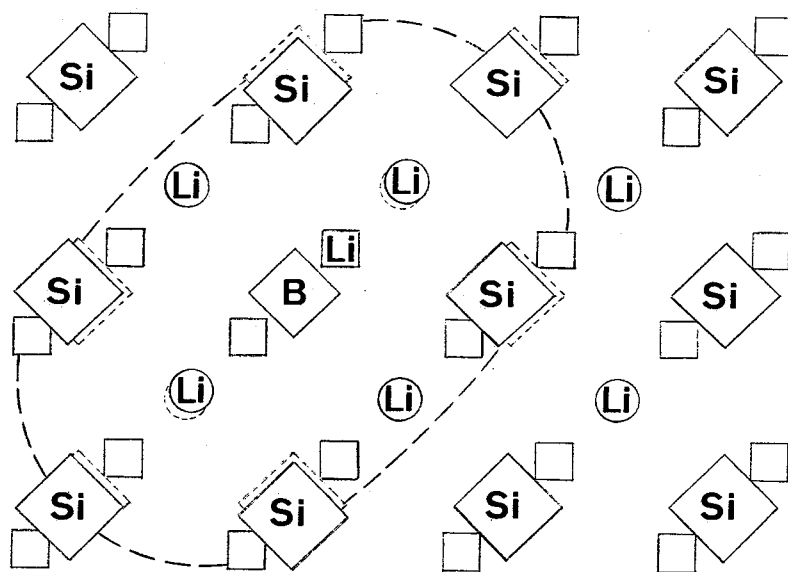
Fig. 5-1 Model of defect core structure which is constructed by B^{3+} ion substitution for Si^{4+} ion. ⬭ represents the region of defect core structure. ⬭ and ⬦ represent the original position in which ◯ and ◇ ions are placed before the formation of defect core structure. (Li) : Li^+ ion occupied sites, ☐ : available empty sites for Li^+ ions. Both contain the six kinds of position. Additional Li^+ ions introduced by the formation of the defect core structure occupy any of the ☐ site with roughly equal possibility.

ble 126 individual atomic sites (available sites) per supercell. That is, each subcell contains 8 Li atoms, i.e., 2 chemical formula units. Accordingly, 70 empty sites (V_a) in the 126 available sites are applicable for the additional x Li atoms in the B-substituted $Li_{4+x}B_xSi_{1-x}O_4$.

In the case of $Li_{4+x}B_xSi_{1-x}O_4$, an additionally introduced Li^+ ion (Li_{ai}) by the formation of the Li^+-BO_4^{5-} complex in the defect core structure could occupy in any kinds of V_a sites with roughly equal possibility, because the observed occupation factors in pure silicate are the same order of magnitude among all Li sites[1], suggesting a dynamically disordered sublattice of Li^+ ions. In this Li^+ ion sublattice, we have already discussed abnormally short V_a-V_a distances of 0.8, 1.3, 1.5 and 1.9A, while V_s-V_s distances are between 2.3 and 2.9A[2]. These short distances and equal occupying possibility suggest that Li_{ai} would be easy to hop and that the activation energy for the ion hopping would also be reduced from that for the V_a-V_s hopping.

Thus, it is understandable that Li_{ai} can migrate throughout the crystal. In addition, the experimental results of mobile ion content variation versus x demand that both $Li^+(V_s)$ and $Li^+(V_a)$ should migrate[2], where $Li^+(V_s)$ and $Li^+(V_a)$ ions are the Li^+ ions at V_s and V_a sites, respectively. We must hereupon encounter a paradox why both $Li^+(V_s)$ and $Li^+(V_a)$ ions are available for conduction in B-substituted silicate while the $Li^+(V_s)$ ions in pure silicate are hardly mobile to show low conductivity. Cooperative effects of $Li^+(V_a)$ ions with the neighbouring ions could answer the question. We can assume that $Li^+(V_a)$ ion would deform the host anion sublattice at the moment of ion hop, resulting in

the possible cooperation of $Li^+(V_s)$ ion hop. This procedure is shown schematically in fig. 5-2. The marked increase of mobile Li^+ ion content and the decrease of observed activation energy for Li^+ ion conductivity with the increase of x are consistent with this model[2]. This cooperative effect would make $Li^+(V_s)$ ions possible to hop to V_a sites, resulting in no distinction among any Li^+ ions. This actually arises from the short distances of V_s-V_a compared to the distances between V_s sites.

Furthermore, polarized and displaced ions in the defect core structure would contribute to the ionic mobility. When Li_{ai} is located at a V_a site next to SiO_4^{4-}, the nearest oxygen of tetrahedral SiO_4^{4-} would be attracted, resulting in elongation of Si-O distance and in contraction of other three Si-O bond length. The latter mode can reduce the attractive force between tetrahedral oxygen and its nearest Li^+ ion. This can make the Li^+ ion easy to hop. The activation energy for Li^+ ion hop would thus be reduced and its mobility would thus be increased. This is explained in fig. 5-3.

When the content of defect core structure increases throughout the crystal, they would interact each other. There would be repulsive Coulomb interaction between Li^+ ions at the V_a or V_s sites. This interaction would displace the Li^+ ions from the initial sites leading to the initiation of the ion hopping.

In summary, it is demonstrated how the defect core structure works for the conductivity enhancement as a source of moible ions. Introduced Li^+ ions by a substitution with aliovalent ion have tendency to construct a defect core structure and to occupy any other available sites, dynamically. This Li^+ ion motion may
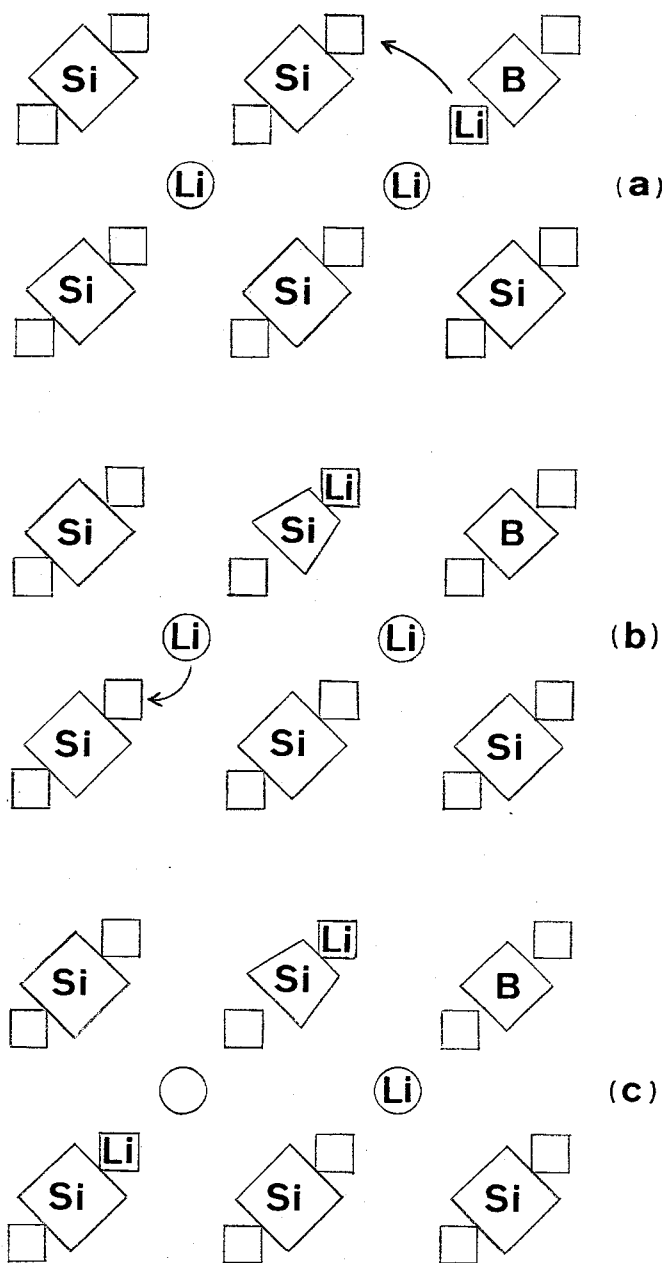
Fig. 5-2   Schematic feature of cooperative interaction to induce the hopping of $Li^+(V_s)$ ion.   (a) Additionally introduced Li^+ ion (Li_{ai} : ⌐Li⌐) by the formation of the defect core structure hops to the neighbouring V_a site (⌐ ⌐).   (b) $Li^+(V_a)$ ion deforms the nearest SiO_4^{4-} ion, resulting in the weakening of the attractive interaction with $Li^+(V_s)$ ion (Li).   (c) As a result, $Li^+(V_s)$ ions would be mobile to hop to the nearest V_a site.
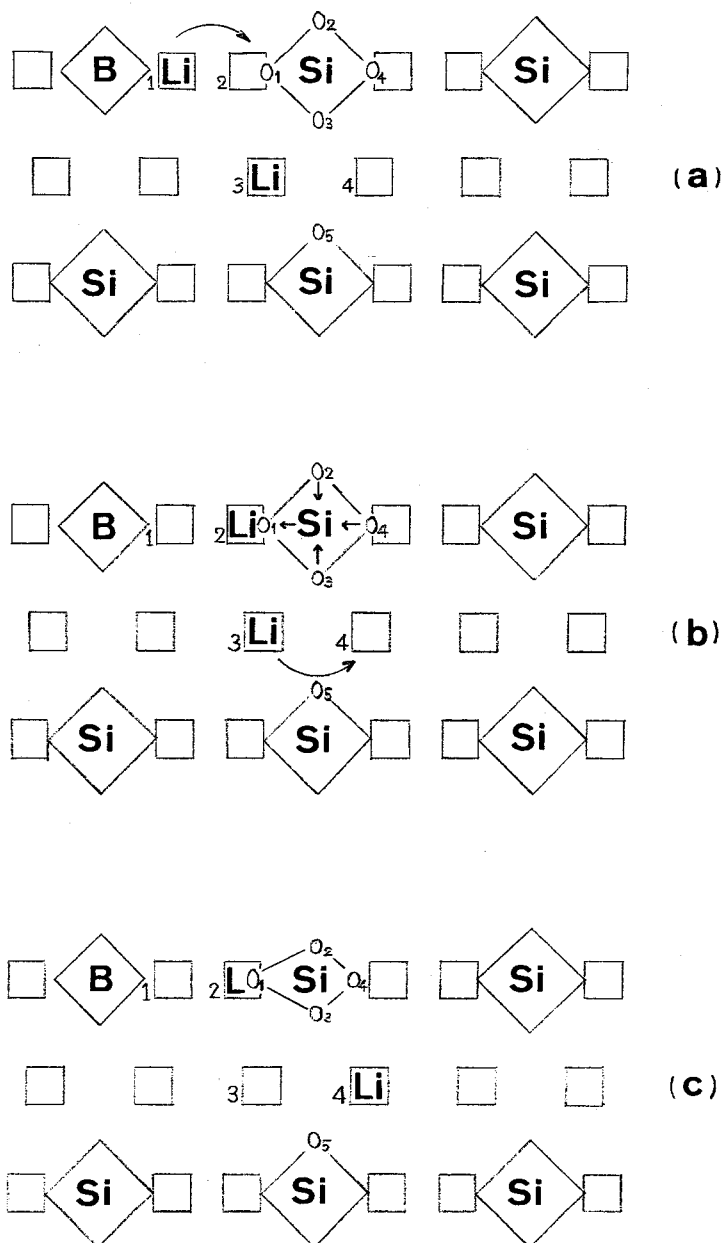
Fig. 5-3 Example of hopping motion by the increase of ionic mobility due to the polarization of SiO_4^{4-} ion. (a) Formation of the defect core structure introduces the Li_{ai} ion in the $V_a(1)$ site in the vicinity of BO_4^{5-} ion. (b) When $Li^+(V_a(1))$ ion hops into the $V_a(2)$ site, the nearest SiO_4^{4-} ion is polarized. It could be assumed that the $Li^+(V_a(2))$ ion induces the deformed mode of SiO_4^{4-} structure in which O_1 is attracted to $Li^+(V_a(2))$ ion and other three oxygens are displaced toward the Si^{4+} ion. (c) This elongates the O_3-O_5 distance, and reduces the hindrance effect of O_3 and O_5 ions for the $Li^+(V(3))$ ions hopping to $Li^+(V(4))$ site, resulting in the increase of the ionic mobility.

induce the neighbouring immobile Li$^+$ ions to be mobile, coopera-tively. Furthermore, the polarized and displaced ions which construct the bottleneck for ion migration can be responsible for the reduction of the activation energy of ion hop. Therefore, the formation of the defect core structure results in not only the increase of mobile ion content but also the increase of its mobility.

5.2 Creation of defect core structure at the interface

In the previous discussion, the defect core structure is one of the models to explain the conductivity increase by the substi-tution with aliovalent ions. The conductivity enhancement of ionic conductors by the insulator particle dispersion is also recognized using this model.

We suppose that the surface of a Na$^+$ ion conductor particle is in contact with an insulator particle as shown in fig. 5-4. If an insulator particle whose surface shows an attractive force for Na$^+$ ions (factors of the attractive force will be discussed in the next section) is applied, mobile Na$^+$ ions could have a tend-ency to be pulled out to the surface or near surface of the ionic conductor. The quasi-complex thus created is composed of the attractive site of the insulator particle and the surface Na$^+$ ions. This quasi-complex would make the neighbouring ions dis-placed and polarized. All of these atomic group should corre-spond to the defect core structure (DCS). The quasi-DCS at the interface consequently creates a Na$^+$ ion vacancy (V_a) at the second neighbour. This vacancy should be the origin of the
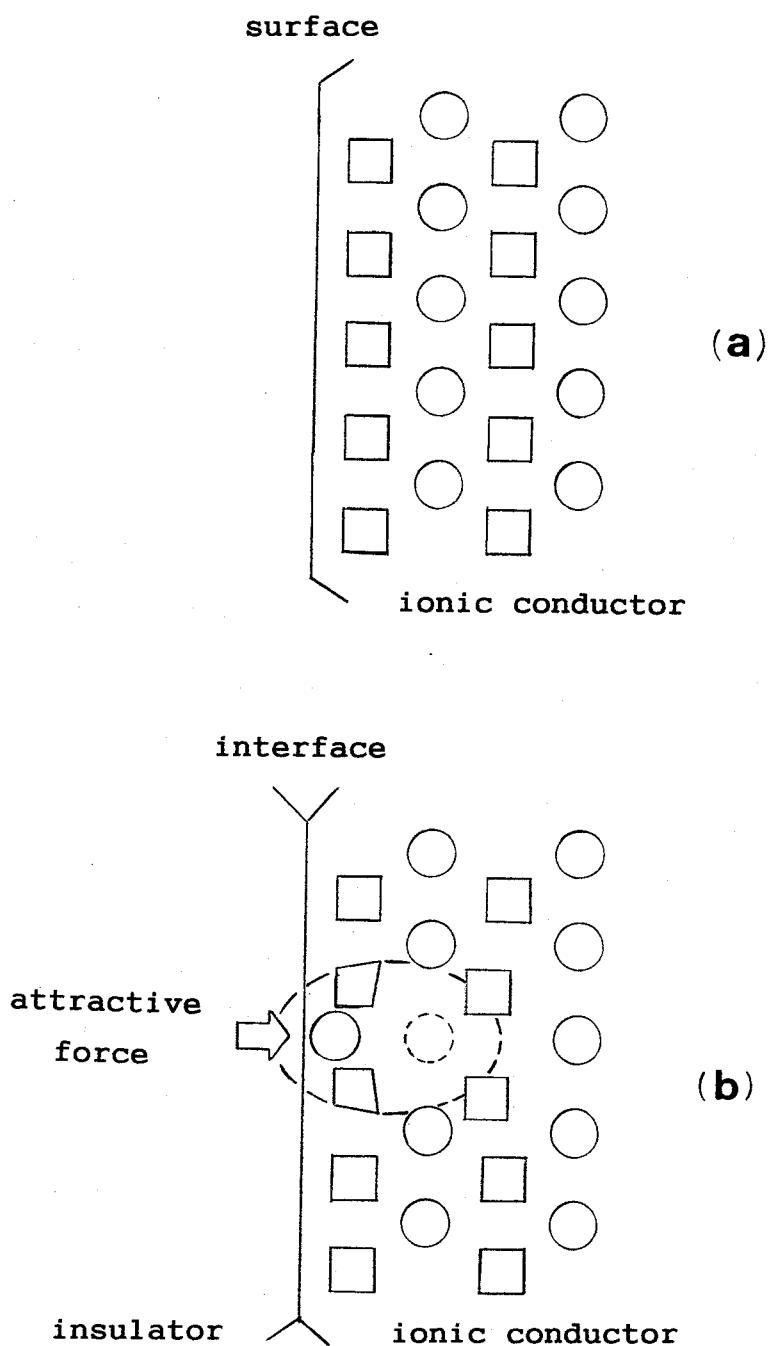
Fig. 5-4 Schematic feature of (a) the surface of ionic conductor and (b) the interface of ionic conductor contacting with insulator particle with attractive site. ○ : occupied sites of Na^+ ion; ⊙ : vacant site of Na^+ ion; □ , ▱ : ordinary and polarized host anions, respectively; ⇨ : attractive site on the insulator particle; ⬭ : quasi-defect core structure.

increase of mobile ion concentration. Many Na^+ ion attractive sites scattered at the insulator surface make a Na^+ ion depletion layer at the near surface in the conductor particle. This depletion layer (space charge layer) therefore has an excess of Na^+ ion vacancies, which allows the high conductivity along the interface. Furthermore, the pulled out Na^+ ion at the surface would deform the neighbouring host anions to reduce the activation energy for Na^+ ion hop through the V_a, similar to that in the case of substituted Li_4SiO_4 represented in fig. 5-3. This results in the increase of Na^+ ion mobility. Both increases of mobile ion concentration and mobility lead to the conductivity enhancement.

5.3 Factor for the quasi-DCS creation

'What is the Na^+ ion attractive force ?' is important for the material designing to develop a high ion conducting composite.

Acidic surface has an effective factor to attract Na^+ ions. As an acid has a tendency to release protons, Na^+ ions tend to replace these protons. This tendency of acidic surface can promote the shift of Na^+ ion at the interface when it contacts with Na^+ ion conductor particle. In order to demonstrate this idea, solid superacid particles (SO_4^{2-}/ZrO_2 and SbF_5/binary metal oxides) which have the stronger acidity than 100% sulfuric acid have been used as dispersants for NZS conductor (chapter 3). When the SbF_5/binary oxides were dispersed, the conductivity has enhanced depending on the acidic strength of the dispersant.

A pair of conductivity plates parallel to one another and separated by a distance, d is known as a simple parallel plate capacitor. On applying a potential difference, V, between the plate, a quantity of charge, Q_0, is stored on them, given by

$$Q_0 = \frac{\varepsilon_0 A}{d} V \qquad (5-1)$$

where ε_0 is the permittivity of free space and A is the area of the plates. Now, we can use the ionic conducting particles instead of the conducting plates. In this case, the surface charge quantity of the two particles is, in general, different to one another, since the different crystalline face will be appear when these particles are placed randomly. That is, every spaces between two ionic conducting particles give a small potential difference, storing a small quantity of charge determined by equation (5-1). If a dielectric substance is now placed between the particles, and the potential difference remains constant, the amount of charge stored increases, depending on the dielectric constant ε'. These increased charge (Na^+ ions) at the surface of the positively charged ionic conductor may arise from the inner part of the crystal, leaving Na^+ ion vacancy. This is the second factor to create the quasi-DCS. The conductivity enhancement by the application of ferroelectric PZT or $BaTiO_3$ with large ε' may indicate the above model.

The application of the particle whose surface is negatively charged or the negative end of polar crystal to the Na^+ ion

conduction particle can be anticipated. But this should be difficult to realize, because we have not yet develop such materials or the arranging techniques to show enough strength of the Na^+ ion attractive force.

In conclusion, it is accepted at present that acidic property and dielectric constant are effective to create quasi-DCS at the interface between ionic conductor and insulator particles. These are therefore the critical factors to demonstrate the enhancement of interfacial conductivity.

References

[1] D. Tranqui, R. D. Shannon and H.-Y. Chen, Acta Cryst., B35, 2479 (1979).

[2] Y. Saito, K. Ado, T. Asai, H. Kageyama and O. Nakamura, Solid State Ionics, 47, 149 (1991).

6. Conclusion

Interfaces in materials exhibit a wide variety of defects such as interstitial ions, vacancies, dislocations and its consequent electronic structures. These defects would have the possibility to create new function because those features are not deduced from the conventional single crystal oriented studies. Ceramic solid electrolyte is one of the typical examples which show the interfacial anomalous feature.

In chapter 1, the purpose of this research and the strategy to achieve that were emphasized.

Chapter 2 represented two analytical methods of a.c. conductivity and their characteristic features. Complex impedance analysis, which was the most popular technique to investigate the electrochemical properties of a.c. conductivity, was effective for the separation of two component, bulk and grain boundary regions in the ceramic conductors. Another technique of frequency dispersion analysis of a.c. conductivity was available to obtain the details of the electrical condutivity which reflects the two main factors, mobile ion content and the mobility. Contribution of each factor to the total conductivity could be estimated utilizing the two components of frequency response, frequency independent (d.c.) conductivity and frequency dependent (a.c.) conductivity in the frequency dispersion analysis.

In chapter 3, it was found that the conductivity of sodium ion conductor $Na_4Zr_2Si_3O_{12}$ (NZS) was enhanced about one to two orders of magnitude by the dispersion of some insulator particles. First, it was expected that the dielectric interactions at

the interface between ionic conductor and insulator particles would be effective for the conductivity enhancement from the theoretical model of space charge layer proposed previously. Therefore, ferroelectric PZT and BaTiO$_3$ particles were dispersed into NZS and observed the enhanced conductivity about one to two orders of magnitude higher than that of pure NZS. When the ferroelectric BaTiO$_3$ particles were dispersed into NZS, conductivity enhancement depended on the dielectric constant of BaTiO$_3$ particles. This reult indicated that the dielectric interaction at the interface would be an important factor for the enhancement of the interfacial conductivity.

Acid-base interaction would be a factor of enhancing the interfacial conductivity. This was expected from the results that the wet Al$_2$O$_3$ particle dispersion into some metal halides showed the higher conductivity than that of dried Al$_2$O$_3$ dispersed composites. Based on this analogy, solid superacid particles, SO$_4$$^{2-}$/ZrO$_2$ were dispersed into NZS, resulting in the conductivity enhancement. In the case of another solid superacid, SbF$_5$/binary oxide dispersion, the conductivity increase depended on the acidic strength of the dispersant. This result suggested that the acid-base interaction would be also effective for the conductivity enhancement of NZS.

Chapter 4 showed the conductivity enhancement by the replacement of one host ion by another ion of different valence for some ionic conductors. The conductivity of LiTi$_2$(PO$_4$)$_3$ (LTP) was enhanced by the substituition of Sc^{3+} for Ti^{4+}. Although the Y^{3+} ions did not substitute for Ti^{4+} ions in the lattice structure, the conductivity of nominal Li$_{1+x}$Y$_x$Ti$_{2-x}$(PO$_4$)$_3$ was enhanced

compared with that of LTP. It was possible to propose that the grain boundary conductivity, which has essentially the different conduction mechanism from that of the bulk conductivity, was enhanced as the result of the increase of the mobile ions segregated in the grain boundary. This situaiton was also observed in the substituted ionic conductor of $NaZr_2(PO_4)_3$ (NZP). When the Ga^{3+} and Cr^{3+} ions, which have the same ionic radii, were tried to substitute for Zr^{4+} ions in NZP, only Ga^{3+} ions did not substitute for Zr^{4+} ions. The ionic conductivity of nominal $Na_{1+x}Ga_xZr_{2-x}(PO_4)_3$ was higher than that of NZP, and the mobile ion content estimated from the frequency dispersion analysis showed the temperature dependence, which was different from the feature of Cr^{3+} substituted NZP. This should reflect the difference of conduction mechanism between bulk and grain boundary. For the Li_4SiO_4 type ionic conductors, the conductivity increased with the expansion of the lattice parameters. The expansion of lattice parameters depended both on the size of substituted trivalent ion for Si^{4+} ion and on the force of the Coulomb interaction between interstitially introduced Li^+ ions and host and doped ions surrounding the Li^+ ions. In the case of $Li_{4+x}B_xSi_{1-x}O_4$, x dependence of the b-axis length showed the maximum at x=0.5 and corresponded to that of the conductivity. This could be interpreted by a simple point charge model in the crystal structure.

In chapter 5, the author discussed the ionic conduction mechanism based on the model of 'defect core structure'. It could be defined that the defect core structure is a deformed structure composed of the doped ions, consequently created de-

fects such as interstitial ions or vacancies, and the displaced and polarized ions in the neighbour of the doped ions. The formation of the defect core structures was the origin of the conductivity enhancement in the doped ionic conductor. The defect core structure was effective to explain the cooperative interaction between mobile ions or mobile ions and host ions, which was demonstrated in the marked increase of mobile ion content. This concept was applied to the composite ionic conductor in order to describe the conductivity enhancement at the interface between ionic conductor and insulator particles. The conductivity enhancement mechanism at the interface could be explained systematically by the definition of the defect core structure at the interface as the deformed structure composed of created defects with the attractive force of insulator particle, and the neighbouring displaced and polarized ions.

Acknowledgment